

Neutrino Spectroscopy with Atoms and Molecules

Atsushi Fukumi¹, Susumu Kuma², Yuki Miyamoto³, Kyo Nakajima², Itsuo Nakano^{3,4}, Hajime Nanjo⁵, Chiaki Ohae³, Noboru Sasao^{2,3†}, Minoru Tanaka⁶, Takashi Taniguchi^{2‡}, Satoshi Uetake^{3,4}, Tomonari Wakabayashi⁷, Takuya Yamaguchi³, Akihiro Yoshimi^{2,3} and Motohiko Yoshimura⁴

¹*Kawasaki College of Allied Health Professions, Kurashiki, Okayama 701-0194, Japan*

²*Research Core for Extreme Quantum World, Okayama University, Okayama 700-8530, Japan*

³*Graduate School of Natural Science and Technology, Okayama University, Okayama 700-8530, Japan*

⁴*Center of Quantum Universe, Okayama University, Okayama 700-8530, Japan*

⁵*Department of Physics, Kyoto University, Kyoto 606-8502, Japan*

⁶*Department of Physics, Osaka University, Toyonaka, Osaka 560-0043, Japan*

⁷*Department of Chemistry, Kinki University, Higashi-Osaka, Osaka 577-8502, Japan*

*E-mail: sasao@fphy.hep.okayama-u.ac.jp

.....
We systematically investigate the new experimental method of using atoms or molecules to measure important parameters of neutrinos still undetermined; the absolute mass scale, the mass hierarchy pattern (normal or inverted), the neutrino mass type (Majorana or Dirac), and the CP violating phases including Majorana phases. Most of these observables are difficult to measure in neutrino oscillation experiments.

There are advantages of atomic targets, due to the closeness of available atomic energies to anticipated neutrino masses, over nuclear target experiments such as the end point spectrum of β decay and two-electron line spectrum in the neutrinoless double β decay, both of which address some of the overlapping objectives with atomic/molecular experiments. Disadvantage of using atomic targets, the smallness of rates, is overcome by the macro-coherent amplification mechanism.

The atomic or molecular process we use is a cooperative deexcitation of a collective body of atoms in a metastable level $|e\rangle$ emitting a neutrino pair and a photon; $|e\rangle \rightarrow |g\rangle + \gamma + \nu_i \nu_j$ where ν_i 's are neutrino mass eigenstates. The macro-coherence is developed by trigger laser irradiation of two colors, which frequently causes two-photon process $|e\rangle \leftrightarrow |g\rangle + \gamma + \gamma$, $|e\rangle + \gamma \leftrightarrow |g\rangle + \gamma$ inside the target. We discuss important aspects of the macro-coherence development in detail, by setting up the master equation for the target Bloch vector (whose components are population difference and medium polarization) and propagating electric field. Our master equation includes effects of phase decoherence of medium polarization and decay of population difference.

The spectral rate (the number of events per unit time) of macro-coherent radiative emission of neutrino pair has three parts, and is given by a factorized formula of the form, (overall ω independent rate denoted by Γ_0) \times (spectral shape function denoted by $I(\omega)$) \times (time evolving dynamical factor), where ω is the photon energy. The constant factor Γ_0 determines the overall rate in the unit of 1/time, and for Xe it is of order, 1 Hz ($n/10^{22}\text{cm}^{-3}$)³ ($V/10^2\text{cm}^3$). The dynamical factor is time dependent and is given by the space integrated quantity over the entire target, of the product of magnitude squared of coherent polarization and field strength (in the unit of the maximally extractable energy density) stored inside the target. The asymptotic value of time evolving dynamical factor is given by contribution of field condensate accompanied by macroscopic coherence, which is calculated using the static limit of the master equation. With an appropriate choice of heavy target atoms or molecules such as Xe and I₂ that has a large M1×E1 matrix element between $|e\rangle$ and $|g\rangle$, we show that one can determine

three neutrino masses along with distinction of the mass hierarchy pattern (normal or inverted) by measuring the spectral shape $I(\omega)$. If one uses a target of available energy of a fraction of 1 eV, the most experimentally challenging observable, the Majorana CP phases, may be determined, comparing detected rate with differences of theoretical expectations which exist at the level of several %. The Majorana CP violating phase is expected crucial to the understanding of the matter-antimatter imbalance of our universe. Our master equation, when applied to E1×E1 transition such as pH₂ vibrational $Xv = 1 \rightarrow 0$, can describe explosive PSR events in which most of the energy stored in $|e\rangle$ is released in duration of order a few nano seconds.

The present paper is intended to be self-contained explaining some details of related theoretical works in the past, and further reports new simulations and our ongoing experimental efforts of the project to realize the neutrino mass spectroscopy using atoms/molecules.

Subject Index neutrino, Majorana particle, lepto-genesis, macro-coherence, paired super-radiance

Contents

1. Introduction and overview	p.3
1.1 Remaining important problems in neutrino physics and our objective	
1.2 Radiative emission of neutrino pair (RENP)	
1.3 Paired super-radiance (PSR) to be controlled	
1.4 More on RENP and PSR	
1.5 Relation to cosmology and outlook	
2. Theoretical aspects of paired super-radiance	p.12
2.1 Super-radiance and extension to two-photon emission process	
2.2 Master equation for paired super-radiance	
2.3 Dynamics of PSR	
3. Theory of macro-coherent radiative emission of neutrino pair (RENP)	p.23
3.1 Coherent neutrino pair emission from atoms/molecules	
3.2 Neutrino properties extractable from the photon spectrum	
3.3 Estimation of the dynamical RENP factor based on asymptotic solution	
4. Experimental aspects of PSR and RENP	p.34
4.1 Overview and strategy towards PSR/RENP experiments	p.34
4.2 PSR experiment with para-hydrogen molecule	p.39
4.3 Towards RENP experiment with Xe	p.52
5. Summary and prospects	p.60
Appendix A: Electroweak interaction under nuclear Coulomb potential	p.63
Appendix B: Mathematical structure of Maxwell-Bloch equation	p.66
Appendix C: Molecules for RENP	p.68
Appendix D: Coherence time measurements of para-hydrogen vibrational levels	p.70
Appendix E: Experimental studies on PSR/RENP targets in condensed phases	p.74
Appendix E.1: Bismuth in neon matrix	p.74
Appendix E.2: HF molecule trapped in solid pH ₂	p.78
Appendix E.3: Nitrogen atom in fullerene C ₆₀	p.80

[†]Corresponding author.

[‡]Deceased.

1. Introduction and overview

1.1. Remaining important problems in neutrino physics and our objective

The present status of neutrino mass matrix is summarized by the following central values measured by oscillation experiments [1], [2]:

$$s_{12}^2 = 0.31, \quad s_{23}^2 = 0.42, \quad s_{13}^2 = 0.024, \quad (1)$$

$$\Delta m_{21}^2 = 7.5 \times 10^{-5} \text{ eV}^2, \quad |\Delta m_{31}^2| = 2.47 \times 10^{-3} \text{ eV}^2. \quad (2)$$

The usual notation of angle factors is used; $s_{ij} = \sin \theta_{ij}$ and $c_{ij} = \cos \theta_{ij}$. The definition of the neutrino mixing (given by U) and mass (\mathcal{M}_ν) matrix is given by [1]

$$U = \begin{pmatrix} 1 & 0 & 0 \\ 0 & c_{23} & s_{23} \\ 0 & -s_{23} & c_{23} \end{pmatrix} \begin{pmatrix} c_{13} & 0 & s_{13}e^{-i\delta} \\ 0 & 1 & 0 \\ -s_{13}e^{-i\delta} & 0 & c_{13} \end{pmatrix} \begin{pmatrix} c_{12} & s_{12} & 0 \\ -s_{12} & c_{12} & 0 \\ 0 & 0 & 1 \end{pmatrix} P, \quad (3)$$

$$P = \begin{pmatrix} 1 & 0 & 0 \\ 0 & e^{i\alpha} & 0 \\ 0 & 0 & e^{i\beta} \end{pmatrix} \quad \text{for Majorana neutrinos,} \quad = 1 \quad \text{for Dirac neutrinos,} \quad (4)$$

$$\mathcal{M}_\nu = U \mathcal{M}_D U^\dagger, \quad (5)$$

(where \mathcal{M}_D is the diagonalized mass matrix). Neutrino masses are ordered by $m_3 > m_2 > m_1$ for the normal hierarchical mass pattern (NH) and $m_2 > m_1 > m_3$ for the inverted hierarchy (IH). For convenience we define the smallest mass by m_0 , which is $= m_1$ for NH and $= m_3$ for IH.

The ongoing and planned experiments to measure the neutrino masses using nuclei as targets are in two directions; (1) measurement of the beta spectrum near the end point sensitive to both Dirac and Majorana masses, (2) neutrinoless double beta decay near the end point of two electron energy sum, sensitive to Majorana masses alone. In the neutrinoless double beta decay one attempts to measure the following parameter combination called the effective neutrino mass [3];

$$\left| \sum_i m_i U_{ei}^2 \right|^2 = m_3^2 s_{13}^4 + m_2^2 s_{12}^4 c_{13}^4 + m_1^2 c_{12}^4 c_{13}^4 + 2m_1 m_2 s_{12}^2 c_{12}^2 c_{13}^4 \cos(2\alpha) + 2m_1 m_3 s_{13}^2 c_{12}^2 c_{13}^2 \cos(2(\beta - \delta)) + 2m_2 m_3 s_{13}^2 s_{12}^2 c_{13}^2 \cos(2(\alpha - \beta + \delta)), \quad (6)$$

using our convention of Majorana phases. The best upper limit of neutrino mass scale is derived from cosmological arguments, and is $\sim 0.58 \text{ eV}$ (95% CL) [4].

Despite of this remarkable success in neutrino physics, there are still many important questions to be answered. (1) Whether the nature favors either of the neutrino mass type, Dirac (described by 4 component spinor equation) or Majorana mass (described by 2 component spinor), is unknown despite of its vital importance to lepto-genesis theory [5], [6]. (2) Two important parameters of the neutrino mass matrix \mathcal{M}_ν , the smallest mass m_0 and the CP violating phase δ , are inaccessible experimentally in the near future. (3) A definite principle of measuring the additional CP phases α, β [7],[3] intrinsic to the Majorana neutrino has not been proposed as yet.

These are challenged by our method of neutrino mass spectroscopy [8],[9],[10] using atoms or molecules instead of nuclei as targets, as closely explained in the present article.

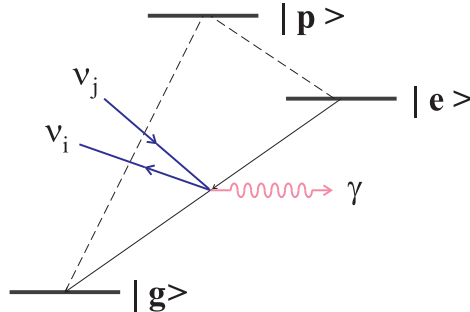


Fig. 1 Λ -type atomic level for RENP $|e\rangle \rightarrow |g\rangle + \gamma + \nu_i \nu_j$ with ν_i a neutrino mass eigenstate. Dipole forbidden transition $|e\rangle \rightarrow |g\rangle + \gamma + \gamma$ may also occur via weak M1 \times E1 couplings to virtual intermediate state $|p\rangle$.

In the rest of this Section we overview theoretical aspects by summarizing essence of theoretical sections, Sec.2 and Sec.3. Experimental status of our project is summarized in Sec.4.

1.2. Radiative emission of neutrino pair (RENP)

The atomic process we use for experiments is $|e\rangle \rightarrow |g\rangle + \gamma + \nu_i \nu_j$, as illustrated in Fig.1. The process exists in the standard electroweak theory [11] without any doubt: it occurs as a combined effect of weak interaction and QED, a kind of second order perturbation process when one regards four Fermi weak process as the first order process. We denote this process by RENP (radiative emission of neutrino pair). The radiation-less pair emission $|e\rangle \rightarrow |g\rangle + \nu_i \nu_j$ is faster as an elementary process than RENP, but with the aid of macro-coherent amplification by trigger laser irradiation RENP dominates over the radiation-less process. Moreover, the single emitted photon is a key to obtain needed information on neutrinos, since emitted neutrinos are difficult to detect. The atomic state $|e\rangle$ is assumed metastable, which means to us that its lifetime roughly $> 1\text{msec}$ (its optimal value to be determined by repetition cycle of excitation and trigger irradiation in actual experiments). Besides a single photon γ the final state has two neutrino mass eigenstates of $\nu_i, i = 1, 2, 3$. The crucial key element of our experimental methods is the ability of resolving neutrino mass eigenstates rather than flavor eigenstates, as realized by the excellent frequency resolution of used trigger laser. This becomes possible by using the technique of trigger laser irradiation in atomic processes. There are step function like threshold rises in the photon energy spectrum and six threshold locations are at

$$\omega_{ij} = \frac{\epsilon_{eg}}{2} - \frac{(m_i + m_j)^2}{2\epsilon_{eg}}. \quad (7)$$

Here $\epsilon_{ab} = \epsilon_a - \epsilon_b$ is the atomic energy difference between two states $|a\rangle, |b\rangle$. Threshold locations sensitive to neutrino masses m_i are separated by small photon energies. For example, $(m_i + m_j)^2/(2\epsilon_{eg}) \sim 5 \text{ meV}$ for $m_i + m_j = 0.1\text{eV}$ and $\epsilon_{eg} = 1\text{eV}$, taking a typical atomic energy difference. One can separate different mass eigenstates by fully exploiting the accuracy of frequency in the range of $\omega \leq \omega_{11}$ (the largest threshold), used as trigger laser in our proposed experiments. In our approach one does not need this order of precision of

detected photon energy. From the continuous spectral shape of the single photon rate one can determine both neutrino masses and mixing angles, along with Majorana phases α, β .

Atomic/molecular targets have an advantage over conventionally used nuclei in their closeness of released energy to neutrino masses (expected much smaller than 1 eV). A demerit of these targets is the weakness of RENP rate $\propto G_F^2 \alpha \epsilon_{eg}^n$ with ϵ_{eg} the available energy of order eV and $n \sim 5$. The smallness of rate is due to the small Fermi constant $G_F \sim 10^{-23} \text{eV}^{-2}$. We use macro-coherence (giving the rate $n^2 V$ with n the target number density, V the target volume) to overcome this problem. When the number density n is close to the Avogadro number per cm^3 , RENP rate may become measurable.

If the macro-coherent amplification works as expected, the neutrino pair emission accompanied by the photon of energy ω occurs according to a time dependent rate formula of the factorized form,

$$\Gamma_{\gamma 2\nu}(\omega, t) = \Gamma_0 I(\omega) \eta_\omega(t). \quad (8)$$

The constant RENP rate Γ_0 may become of order 1 Hz at the target number density 10^{22}cm^{-3} (the Γ_0 value scaling with the number density $\propto n^3$) and the volume 10^2cm^3 in the Xe example whose RENP spectrum $I(\omega)$ in the threshold region is shown in Fig.2.

¹ Relevant levels of Xe are $|e\rangle = 5p^5(^2P_{3/2})6s^2[3/2]_2$, metastable with lifetime of $0[40]\text{sec}$, $|g\rangle = 5p^6\,^1S_0$, and intermediate state $|p\rangle = 5p^5(^2P_{3/2})6s^2[3/2]_1$. The initial and the final states, $|e\rangle, |g\rangle$, have different parities and the angular momentum difference $\Delta J = 2$. Excited states here may be described by a pair state of $6s$ electron and $5p$ hole: both of the initial metastable and intermediate states are given by the spin triplet pair with a large breaking of LS coupling scheme. The dynamical factor $\eta_\omega(t)$ shall be discussed later in Sec. 3 based on the solution of the master equation of Sec. 2.

From the spectrum feature of Fig.2 it should not be difficult to measure the absolute neutrino mass scale and the distinction of normal (NH) and inverted (IH) mass hierarchy of neutrino mass pattern. The Majorana vs Dirac distinction is harder for Xe due to a large energy level difference $\epsilon_{eg} \sim 8.3$ eV. It is found in [12] that the appropriate energy scale for measurements of Majorana CP phases is a fraction of eV.

Attractive candidates of targets may be found in molecules. Molecules are interesting due to a rich vibrational and rotational band structure with much smaller level spacing than the electronic ones. We illustrate RENP spectrum calculation for I_2 electronic transition in Fig.3. Difference of spectrum rates for different CP Majorana phases is a several to 10 % for IH.

1.3. Paired super-radiance (PSR) to be controlled

It is crucial for the success of our method to control a twin process, PSR (paired super-radiance), $|e\rangle \rightarrow |g\rangle + \gamma + \gamma$. PSR event is interesting in itself. With the macro-coherence (in which the coherent volume is not wavelength limited unlike the single photon super-radiance (SR) [13]), typically exhibiting the back to back two photon emission with equal energies at the half of atomic level difference $\epsilon_{eg}/2$ (under the trigger laser of the same frequency). Emitted two photons are highly entangled especially for $J = 0 \rightarrow 0$ transition.

¹ Neutrino parameters taken for this calculation are somewhat different from the most recent values given above, Eq. 2 and are given in Sec.3.

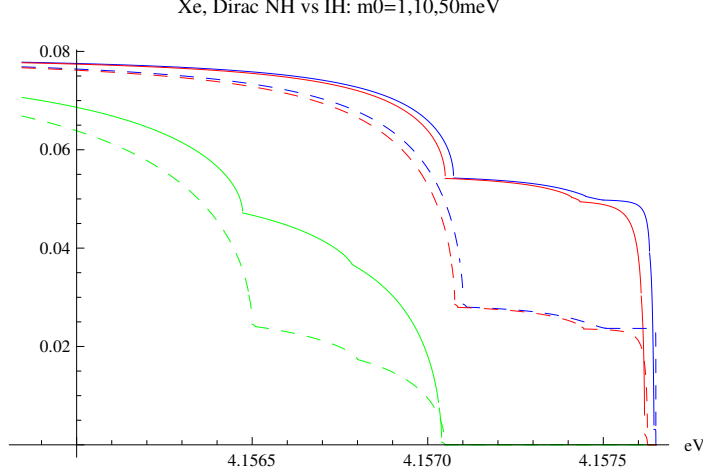


Fig. 2 RENP dimensionless spectrum function $I(\omega)$ near the neutrino pair emission thresholds from Xe level $5p^5(2P_{3/2})6s^2[3/2]_2$. Neutrinos of the smallest mass of 1, 10 and 50 meV are taken for the normal (solid curve) and the inverted (dashed curve) hierarchical mass pattern.

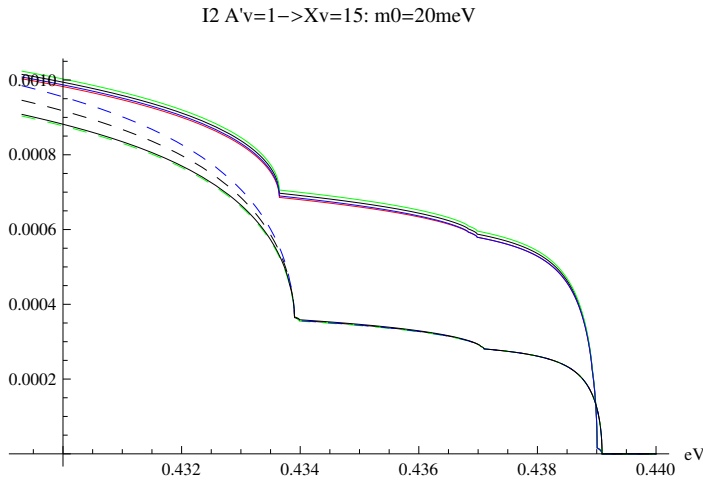


Fig. 3 I_2 RENP spectrum between $A' v=1$ and $Xv=15$. The Majorana (in colored solid for NH and in colored dashed for IH) vs Dirac (in black solid for NH and in black dashed for IH) cases are compared. Three Majorana CP phase combinations $(\alpha, \beta - \delta) = (0, 0)$ (in red), $(\pi/2, 0)$ (in green), and $(0, \pi/2)$ (in blue) are taken, with the smallest neutrino mass 20 meV. The vertical scale is in arbitrary units.

For long targets of the number density of metastable state over $\sim 10^{20} \text{ cm}^{-3}$, explosive PSR occurs if the initial coherence between $|e\rangle$ and $|g\rangle$ is present [14]. Explosive PSR event is characterized by instantaneous release of energy stored in the upper level $|e\rangle$ into short pulses of some time structure, taking place with a time delay after weak trigger irradiation, as illustrated in Fig.4 for vibrational pH_2 transition. The largest instantaneous output/input power ratio in this figure is $O[10^{21}]$. The macro-coherent PSR is fundamentally different from

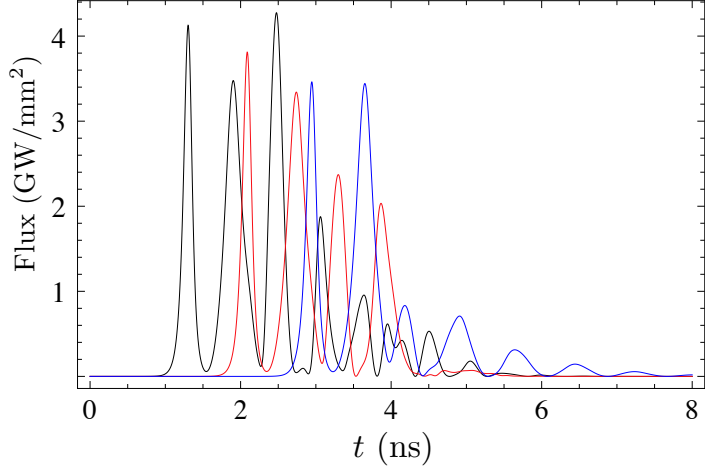


Fig. 4 Time-evolving PSR output flux resulting from the symmetric trigger irradiation at two target ends, of the power range, $10^{-12} \sim 1 \text{ Wmm}^{-2}$, under the conditions of the target number density $n = 1 \times 10^{21} \text{ cm}^{-3}$, target length = 30cm, relaxation times $T_2 = T_3 = 10$, $T_1 = 10^3$ ns's, and the initial polarization, $r_1^{(0)} = 1$ and all other Bloch vector components = 0. Depicted outputs from 1 Wmm^{-2} trigger power in black, from 10^{-6} Wmm^{-2} in red, and from $10^{-12} \text{ Wmm}^{-2}$ in blue are displaced almost equi-distantly in the first peak positions. Vibrational transition $Xv = 1 \rightarrow Xv = 0$ of pH₂ is considered.

SR of a single photon emission process in that the coherent region is extended beyond the wavelength.

The macro-coherent amplification works for both PSR and RENP. Its principle may be stated in simple terms as follows [15]. Coherent emission of particles (photons and neutrinos) from a collective body of target atoms is characterized by quantum mechanical rate (probability per unit time, not necessarily time independent) which is a squared quantity of the sum of amplitudes from many atoms. When plane wave functions of emitted particles are extracted, the rate from the collective body is proportional to

$$|\sum_L e^{i\sum_i \vec{k}_i \cdot (\vec{r} - \vec{r}_L)} \mathcal{A}_L(\vec{r}, t)|^2, \quad (9)$$

where \vec{k}_i are momenta of emitted particles including those of neutrinos and \vec{r}_L is the atomic position. The atomic amplitude part $\mathcal{A}_L(\vec{r}, t)$ is expected to be slowly varying with \vec{r}_L in the wavelength scale of \vec{k}_i . Unlike the incoherent decay in which the phases of $\mathcal{A}_L(\vec{r}, t)$ from different atoms are random (resulting in the summed quantity Eq. 9 of order N), the coherent process requires a high level of phase coherence of this quantity to give order N^2 to Eq. 9. When a single photon is involved as the only emitted particle of the process, $\sum_i \vec{k}_i = \vec{k}$, the maximal coherence region is limited by the wavelength $\sim 1/k$, the inverse of the wave number. Nonetheless the coherent amplification $\propto N^2$ (N is the number of atoms within the wavelength limited coherent volume) leads to an explosive collective decay as first discussed in the celebrated paper of Dicke and later confirmed experimentally (see the next chapter on more of this). A typical effect of Dicke super-radiance is the sudden de-excitation of all atoms in the wavelength limited coherent volume, emitted photons confined in a narrow axial direction. On the other hand, the wavelength limitation is removed when

more than two particles are involved as in PSR and RENP and the momentum conservation $\sum_i \vec{k}_i = 0$ holds: the coherent volume may become truly macroscopic without the wavelength limitation [15]. In the case of PSR the momentum and the energy conservation limits emitted two photons to back-to-back direction and of equal energy $\epsilon_{eg}/2$, if no other phase memory is present. The termination of macro-coherent process may be much more rapidly expedited than in the Dicke case. Both super-radiance and macro-coherent amplification is a highly dynamical process, and one cannot describe its principal feature by a time constant rate. One needs a time evolving dynamical equation, which we call the master equation.

The master equation that describes PSR events including the spatial grating effects (macroscopic polarization varying with the wavelength) has been derived in [14]. The equation is given in terms of the Bloch vector components $R_i(x, t)$, $i = 1, 2, 3$ for medium polarization ($R_1 \pm iR_2$) and the population difference (R_3), and field mode envelopes $\vec{E}_i(x, t)$ ($i = R, L$ denoting right- and left-moving modes). The single spatial direction, x -axis, is selected as the direction of trigger irradiation. Our master equation contains relaxation effects described by three time constants, T_3, T_2, T_1 where the phase decoherence times, T_2 for spatially homogeneous modes and T_3 for spatial grating modes (both $\ll T_1$) are more important. The population decay time T_1 may effectively be taken infinitely large in our problem. It is convenient to rescale these and length/time variables x, t using dimensionless variables. The dimensionless Bloch vector is rescaled by dividing the excited target number density n , the field envelope strength by $\epsilon_{eg}n$, while the length/time by $t_* \equiv 2/(\epsilon_{eg}\alpha_{ge}n)$. Here $\alpha_{ge} \propto$ the product of two transition dipole moments. In the double limits of large relaxation times and large target length, explosive PSR events may occur with an effective rate proportional to the stored energy in $|e\rangle$ / time duration. Dependence of an effective PSR rate on the number density is then automatically $\propto n^2$ and the macroscopic target volume is the relevant coherent volume. Thus, if the target length $\gg ct_*$ and relaxation time $\gg t_*$, one may expect explosive PSR, a new phenomenon which may find interesting applications, for instance in quantum information.

Explosive events are not the only important outcome of PSR phenomenon. It turns out that static condensate remains after PSR emission and we expect that these condensates are described as steady state solutions of our master equation by taking vanishing time derivatives, namely static solutions. If one neglects the spatial grating effect, these states are expected to become aggregate of many absolutely stable solitons as given in [14]. The most important aspect of these condensate states is their stability against two photon emission, and their instability for RENP. By its stability the condensate formation makes the signal to the background ratio RENP/PSR large. The condensate formation of large active region for RENP is then the ideal target state for RENP experiments. PSR (or rather two photon emission) has dual roles of importance to realization of RENP; first as a trigger to expedite RENP and second as a background of RENP to be rejected. We shall explain how these conflicting aspects are reconciled by condensate formation having a very small leakage flux at target ends.

1.4. More on RENP and PSR

Let us clarify further the mechanism of macro-coherent RENP amplification. The electroweak amplitude of RENP for a single atom is [8]

$$\mathcal{H}_{\gamma\nu} = \frac{G_F(\vec{d})_{gp} \cdot \vec{E}(\vec{S})_{pe} \cdot \sum_{ij} a_{ij} \nu_j^\dagger \vec{\sigma} \nu_i}{\epsilon_{pg} - \omega}, \quad a_{ij} = U_{ei}^* U_{ej} - \delta_{ij}/2, \quad (10)$$

where \vec{S} and \vec{d} are spin and dipole operators for atomic electron, and U is the unitary matrix relating the neutrino flavor, for instance ν_e , to the mass eigenstate ν_i , containing mixing angles and Majorana CP phases α, β like $U_{e2} \propto e^{i\alpha}, U_{e3} \propto e^{i(\beta-\delta)}$. This effective hamiltonian is derived in the second order of perturbation of the electroweak theory where both Z and W exchange diagrams of weak interaction are involved [8]. Three atomic levels are involved; $|e\rangle$ for the initial, $|p\rangle$ for the virtual intermediate, and $|g\rangle$ for the final states. Using the terminology of atomic physics, one would say that RENP involves $M1 \times E1$ transition. Assume momentarily (proved by macro-coherence) both the energy and the momentum conservation of 3-body RENP process. This determines six threshold energies of neutrino pair emission at the photon energy $\omega = \omega_{ij} = \epsilon_{eg}/2 - (m_i + m_j)^2/(2\epsilon_{eg})$. The threshold rises of rates are determined by the elements of the neutrino mass matrix, including θ_{13} and Majorana phases (α, β) , as illustrated in Fig.2.

Let us explain how the Majorana/Dirac distinction comes out.²

The Majorana field [11], [9] can be decomposed in terms of plane wave modes as

$$\psi^M(\vec{x}, t) = \sum_{i, \vec{p}} \left(u(\vec{p}) e^{-iE_i t + i\vec{p} \cdot \vec{x}} b_i(\vec{p}) + u^c(\vec{p}) e^{iE_i t - i\vec{p} \cdot \vec{x}} b_i^\dagger(\vec{p}) \right), \quad (11)$$

where the annihilation $b_i(\vec{p})$ and creation $b_i^\dagger(\vec{p})$ operators of the same type appears in the expansion (the index i gives the i -th neutrino of mass m_i , and the helicity summation is suppressed for simplicity). The concrete form of the 2-component conjugate wave function $u^c \propto i\sigma_2 u^*$ is given in [9]. The Dirac case is different involving different type of operators $b_i(\vec{p})$ and $d_i^\dagger(\vec{p})$:

$$\psi^D(\vec{x}, t) = \sum_{i, \vec{p}} \left(u(\vec{p}) e^{-iE_i t + i\vec{p} \cdot \vec{x}} b_i(\vec{p}) + v(\vec{p}) e^{iE_i t - i\vec{p} \cdot \vec{x}} d_i^\dagger(\vec{p}) \right). \quad (12)$$

Neutrino pair emission amplitude of modes $i\vec{p}_1, j\vec{p}_2$ contains two terms in the case of Majorana particle:

$$b_i^\dagger b_j^\dagger (a_{ij} u^*(\vec{p}_1) u^c(\vec{p}_2) - a_{ji} u^*(\vec{p}_2) u^c(\vec{p}_1)), \quad (13)$$

and its rate involves

$$\begin{aligned} & \frac{1}{2} |(a_{ij} u^*(\vec{p}_1) u^c(\vec{p}_2) - a_{ji} u^*(\vec{p}_2) u^c(\vec{p}_1))|^2 \\ &= \frac{1}{2} |a_{ij}|^2 (|\psi(1, 2)|^2 + |\psi(2, 1)|^2) - \Re(a_{ij})^2 (\psi(1, 2)\psi(2, 1)^*), \end{aligned} \quad (14)$$

where the relation $a_{ji} = (a_{ij})^*$ is used and $\psi(1, 2) = u^*(\vec{p}_1) u^c(\vec{p}_2)$. Result of the helicity sum $\sum (\psi(1, 2)\psi(2, 1)^*)$ is given in [9], which then gives the interference term $\propto \Re(a_{ij})^2$. The first term $\propto |a_{ij}|^2$ is common to the Dirac and the Majorana neutrino.

² In what follows we explain how the interference term arises for the pair emission of Majorana fermions using the two-component formalism of [9]. In Sec. 3 a similar derivation of the interference term is given using the four-component formalism of the constrained, self-conjugate field $\psi^c = \psi$. Two methods give identical results.

The macro-coherence is developed by irradiation of two trigger lasers of frequencies ω_i with the relation $\omega_1 + \omega_2 = \epsilon_{eg}$. The development of macro-coherence works for any combination (ω_1, ω_2) and not restricted to $\omega_1 = \omega_2$. The frequency at the red side $\omega_1 (< \epsilon_{eg}/2)$ is set for detected RENP photon energy. The effective interaction of two fields \vec{E}_i of frequency ω_i with atoms is given by

$$\mathcal{H}_{2\gamma} = \frac{(\vec{d})_{gp} \cdot \vec{E}_1 (\vec{m})_{pe} \cdot \vec{E}_2}{\epsilon_{pg} - \omega_2} \equiv (\vec{E}_1)_i (\alpha_{ge})_{ij} (\vec{E}_2)_j, \quad (15)$$

where $\vec{m} = ge\vec{S}/2m_e$ is the magnetic dipole operator, \vec{S} being the electron spin operator. $(\alpha_{ge})_{ij}$ is a tensor giving the interaction strength of PSR [14] [16]. The added hamiltonian $\mathcal{H}_{2\gamma} + \mathcal{H}_{\gamma\nu}$ ($\vec{E} = \vec{E}_1$ and $\omega = \omega_1$ in Eq. 10) describes the atom-field-neutrino interaction. We shall treat effects of $\mathcal{H}_{2\gamma}$ non-perturbatively, solving this part exactly by numerical means, and $\mathcal{H}_{\gamma\nu}$ is treated in the first non-trivial order of perturbation.

Two trigger laser irradiation is designed for efficient coherence development. Depending on the magnitude of the product of dipoles that appears in Eq. 15, there may or may not be significant PSR emission. What is important for RENP is the later stage after PSR related activities. The asymptotic state of fields and target atoms in the latest stage of trigger irradiation is described by static solutions of the master equation for time evolution. In many cases there is a remnant state consisting of field condensates accompanied with a large coherent medium polarization. In the limit of small T_3 decoherence time (relaxation time for grating modes) this condensate is expected to be identical to a soliton discovered in [14] or their aggregate. In any event the asymptotic target state is stable against two-photon emission, but RENP occurs from any point in the target.

Laser irradiation is continued until \sim several times the relaxation time T_2 (non-grating spatially homogeneous modes) of phase coherence and terminated there. This cycle is repeated to accumulate detectable level of RENP photons. During a cycle RENP photon is emitted within the whole space region within the target length because of the instability of condensates against RENP. On the other hand, PSR photons are emitted at two target ends due to a leakage flux, and not from the inside of medium, because condensates inside the target do not emit PSR photons. This way the signal to the background ratio RENP/PSR is largely enhanced by the small leakage energy flux at two ends due to QED two-photon process.

The important dynamical factor $\eta_\omega(t)$ in Eq. 8 is given by the bulk integral over all target atoms/molecules of the quantity, the absolute magnitude squared of macroscopic polarization \times the total field strength, both in the dimensionless units, as fully explained in Sec. 3. The time dependence of $\eta_\omega(t)$ disappears in the asymptotic time limit, and this limit is described by the static solution of our master equation. Non-trivial static limit exists and the asymptotic state consists of the field condensate supported by a macroscopic medium polarization. The state is identified as the soliton of [14] in some parameter limit.

Besides the large bulk/edge rate enhancement there exists a method to selectively detect RENP against two photon emission (namely weak perturbative PSR). The magnetic field may be used to verify parity violating (PV) effects such as correlated emission of photons to the field axis, effect intrinsic to the weak process. Evidently PV effects such as emergence of circular polarization and angular correlation of emitted photons to atomic spin are critical to prove that the process involves weak interaction.

We mention an important point for the target choice of RENP. There is a technical, but important reason why one has to look for heavy atoms or heavy molecules as candidate targets. This is explained for $J = 2 \rightarrow 0$ (whose example is the Xe case) and $J = 0 \rightarrow 0$ (Yb case) transitions in the following. The $M1 \times E1$ atomic transitions for RENP go through the angular momentum change of $J = 2 \rightarrow 1$ and $J = 1 \rightarrow 0$, or $J = 0 \rightarrow 1$ and $J = 1 \rightarrow 0$. The $M1$ transition is governed by atomic matrix elements of $\langle J \pm 1 | \vec{S} | J \rangle$. It can be shown that these matrix elements vanish in the limit of exact LS coupling scheme. The LS coupling scheme, however, breaks down for heavy atoms/molecules [17], and the overtaking jj coupling scheme evades this constraint, which explains a possible large $M1$ matrix elements.

1.5. Relation to cosmology and outlook

Our RENP measurements are sensitive to Majorana CP phases in the following combinations in the photon energy thresholds [10];

$$\begin{array}{c|c|c} (12) & (13) & (23) \\ \hline c_{12}^2 s_{12}^2 c_{13}^4 \cos 2\alpha & c_{12}^2 c_{13}^2 s_{13}^2 \cos 2(\beta - \delta) & s_{12}^2 c_{13}^2 s_{13}^2 \cos 2(\alpha - \beta + \delta) \end{array}$$

It would be of considerable interest to compare this with the following combination of the lepton asymmetry that often appears in lepto-genesis theory [6]:

$$\frac{3y_1^2}{4\pi} \left(-2\left(\frac{m_3}{m_2}\right)^3 s_{13}^2 \sin 2(\alpha - \beta + \delta) + \frac{m_1}{m_2} \sin(2\alpha) \right). \quad (16)$$

While the overall factor y_1 , the Yukawa coupling related to the heavy Majorana fermion, is unknown, the other combination of neutrino mass parameters has strong correlation to experimentally measurable quantities in RENP.

If one succeeds in measurements of RENP, one may hope and proceed to detect relic neutrinos of 1.9 K by using the spectrum distortion due to the Pauli blocking effect caused by the relic sea of cosmic neutrinos [18].

Our experimental strategy towards precision neutrino mass spectroscopy is first to prove the macro-coherence principle by QED process of stronger $E1 \times E1$, namely the discovery of explosive PSR, and then to control PSR and create ideal form of condensates for preparation of RENP. A good target of $E1 \times E1$ type is pH_2 vibrational transition $Xv = 1 \rightarrow 0$ [14], whose molecular properties shall be given in the following sections.

In the rest of this article we shall give detailed account of theories behind the neutrino mass spectroscopy and our current experimental status towards this project. We shall present material in a self-contained way even at the risk of overlap with our several past publications on this subject. Moreover, the material is presented in order to clarify how we develop experimental steps towards the goal of precision neutrino mass spectroscopy. This way we give detailed account of PSR and condensate formation so crucial to our neutrino mass spectroscopy.

The rest of the article is organized as follows. In the first two sections we develop theories of PSR and RENP based on macro-coherent amplification mechanism. Throughout these theoretical sections the natural unit of $\hbar = c = 1$ is used. In Sec. 4 experimental aspects of PSR and RENP and the status of our experimental project are described. Several Appendices give detailed accounts that supplement the main text.

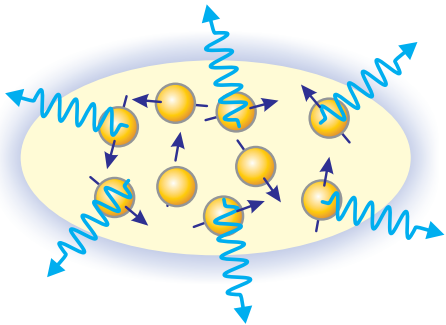


Fig. 5 Cartoon of spontaneous emission from a body of target atoms.

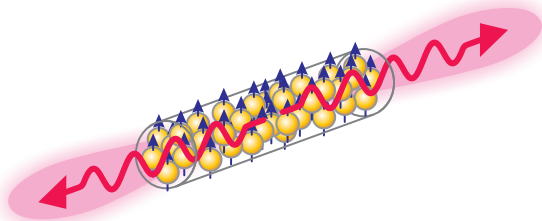


Fig. 6 Cartoon of explosive PSR.

2. Theoretical aspects of paired superradiance

The twin process of two-photon emission $|e\rangle \rightarrow |g\rangle + \gamma + \gamma$ is important to experimental realization of RENP $|e\rangle \rightarrow |g\rangle + \gamma + \nu_i \nu_j$ from two reasons; (1) QED proof of the macro-coherent amplification mechanism replacing the much weaker neutrino process, and (2) control of this QED process to reduce the major background against RENP. In this Section we shall focus on theoretical aspects of macro-coherent two-photon emission, termed paired super-radiance, or PSR in short. PSR is very interesting and has its own merits in quantum optics. The first observation of PSR is our primary goal prior to commencement of RENP experiments. Aspects more directly related to real experiments shall be discussed in Sec. 4.

We deal with atomic processes, either in PSR or in RENP. The fundamental interaction of atomic electrons with the transverse electromagnetic field and the neutrino field is briefly summarized in Appendix A. The upshot of this approach is to use bound or nearly free electron wave functions under the influence of nuclear Coulomb potential for computation of atomic transition matrix elements, which prevails in the following discussions.

It is useful first to compare PSR to the related process of single photon super-radiance [13], or SR in short. We shall thus begin with some rudimentary discussions on SR. These two phenomena have similarities and differences. Cartoons showing spontaneous emission and paired super-radiance are illustrated in Fig. 5 and Fig. 6. At a superficial level this cartoon may give an impression that PSR is similar to SR, but the photon energy, the region of macro-coherence, and how they are realized is entirely different, as explained below.

2.1. Super-radiance and extension to two-photon emission process

2.1.1. Super-radiance. The most common de-excitation process of excited atoms as occurs in a dilute gas is the spontaneous decay $|e\rangle \rightarrow |g\rangle + \gamma$, which arises in the presence of a non-vanishing electric dipole (E1) transition moment between two relevant levels, $|e\rangle$ and $|g\rangle$. The decay follows, as time t increases, the exponential law $e^{-\Gamma t}$ with a decay rate Γ whose inverse is a major portion of lifetime (the inverse lifetime is given by a sum of rates over other de-excitation processes). The interaction hamiltonian that appears in the Fermi golden rule for the transition rate contains a product of dipole matrix element and electric field \vec{E} of

emitted photon; $H = \langle g | \vec{d} | e \rangle \cdot \vec{E}$. The selection rule for this dipole-allowed transition is the parity change and the angular momentum rule $\Delta J = \pm 1, 0$ (except the strictly forbidden $J = 0 \rightarrow 0$ transition) between two states. A typical lifetime would be around 10 ns taking atomic energy difference of 1 eV and atomic size of 10^{-8} cm. Between the same parity states the E1 transition is forbidden and the dominant process of radiative decay may be a weaker magnetic dipole (M1) transition which is caused for instance by an atomic operator $g e \vec{S} \cdot \vec{B} / (2m_e)$ where \vec{S} is the electron spin operator and \vec{B} is the magnetic field of emitted photon. M1 decay rate is typically $\alpha \sim 1/100$ smaller than E1-allowed decay rate. Besides the exponential law the spontaneous decay has an isotropic angular distribution of emitted photon unless the initial state is spin polarized (even with spin polarization the anisotropy of distribution is a minor effect).

These features of spontaneous decay are dramatically changed when atoms decay cooperatively. Dicke [13] pointed out in 1954 the possibility of what he termed super-radiance (SR). The point here is that for N excited atoms in a volume within the wavelength λ of emitted photons there is no quantum mechanical way to distinguish a host atom of emitted photon. Assuming no decoherence of phases due to interaction etc, all N atoms may decay with a definite phase relation preserved from the beginning of the decay process. Suppose that several photons emitted in an initial stage have nearly the same direction by a chance, for instance along the prolongation axis in a cylindrical configuration of target atoms, then all these atoms may undergo cooperative decay. Dicke mentioned a nice analogy of this coherent initial state of $N (\gg 1)$ atoms to an eigenstate of total angular momentum. In this picture two relevant states are regarded as spin up and spin down state. Thus, $|e\rangle = |\uparrow\rangle, |g\rangle = |\downarrow\rangle$, and the initial inverted state of N atoms is given by an eigenstate of the total angular momentum, $|J, J\rangle = |\uparrow\rangle \times |\uparrow\rangle \times |\uparrow\rangle \times \dots \times |\uparrow\rangle$ with $J = N/2$. The radiative decay of the transition $|e\rangle \rightarrow |g\rangle$ is governed by the lowering operator \tilde{J}_- of angular momenta. If any phase decoherence does not occur during subsequent radiative decays, then one would arrive at a state again given by eigenstate of the total angular momentum,

$$|J, M\rangle = \tilde{J}_-^{J-M} |J, J\rangle. \quad (17)$$

All these states satisfy the maximal symmetry under interchange of atoms. When M becomes $O[1] \ll N$, the factor $|\langle J, M-1 | \tilde{J}_- | J, M \rangle|^2$, hence the rate of the total de-excitation of the collective body, becomes proportional to $O[N^2]$, as verified by the well known relation, $\tilde{J}_- |J, M\rangle = \sqrt{(J+M)(J-M+1)} |J, M-1\rangle$. The enhancement of decay rate is hence due to $\sqrt{(J+M)(J-M+1)} = O[N]$ for $|M| \ll N$. The underlying situation is that there are $O[N]$ ways to connect initial and final eigenstates reflecting the indistinguishable nature of host atoms. This simple picture breaks down in the presence of de-phasing such as van-der Waals interaction, because the maximal symmetry is broken by interaction.

Two essential features of SR lie in time profile and directionality of emitted photons. The temporal feature of the SR de-excitation as illustrated in Fig.7 (our own experimental result) is the early termination in the form of short pulse at time $\sim 1/(\Gamma N)$ and duration of a short time of the same order. The initial time of cooperative decay, usually called the delay time in the literature, may be defined as of this order $1/(\Gamma N)$. Distribution of emitted direction is uni-directional along the prolongation axis of the cylinder, taken as x direction. For simplicity we can ignore transverse field effect parallel to y, z directions in the cylindrical configuration.

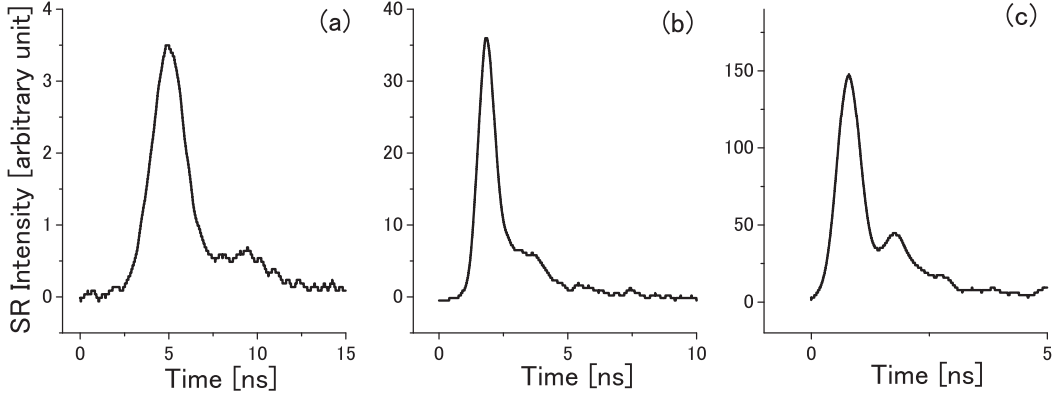


Fig. 7 Super-radiance signals [23] observed in the de-excitation process from Ba $6s6p\ ^1P_1$ to $6s6d\ ^1D_2$ state. Note the changes in delay times and peak heights as the density of the excited state increases from (a) to (c).

It would be appropriate now to explain fundamental dynamical variables and their equations to further analyze the process. We take the continuum limit of atom distribution within the target. The fundamental dynamical variable of medium is then the two-component complex wave function at each space point $\psi_a(x, t)$, $a = e, g$, and the field variable is electric field $E(x, t)$ (ignoring the vectorial nature). Instead of the wave function it is more convenient to use their bilinear forms, called the Bloch vector, $\vec{R}(x, t) \equiv \psi^*(x, t)\vec{\sigma}\psi(x, t)$ (due to the slow atomic motion the norm $\psi^*(x, t)\psi(x, t)$ expressing the atomic number density may be taken constant). The Bloch vector is a linear combination of the density matrix element, and it obeys in the pure quantum state the von Neumann equation equivalent to the Schroedinger equation. What is left to work out is then to write extended von Neumann equation and the generalized Maxwell equation incorporating atom-field interaction and effects of relaxation in an open system, generally described by two relaxation time constants T_i , $i = 1, 2$ for the two-level system [19].

Extensive works have been devoted to elucidate the origin of initiation for SR. The commonly accepted view originating from works of [20] is that the inverted state of N atoms generates quantum fluctuation of medium polarization of $O[\sqrt{N}]$, inducing field emission due to E1 coupling in the basic hamiltonian, and it finally develops into a classical coherence evolution. This gives rise to a natural time scale $1/\Gamma$ for initiation. More concretely, the origin of quantum fluctuation lies in the quantum algebraic relation between the medium polarization R_{\pm} and the population difference R_3 that prevails in the entire volume of target:

$$[R_+, R_-] = 2R_3, \quad (18)$$

as readily derived from the identity $|e\rangle\langle g|g\rangle\langle e| = |e\rangle\langle e|$ etc at each atom. In the completely inverted case R_3 is of order N , and one may take the right hand side of this equation to be a c-number of this order. This Heisenberg type of algebraic relation then gives polarization a quantum fluctuation of RMS value of $\langle R_+R_- \rangle = O[N]$, even if its linear average value vanishes: $\langle R_{\pm} \rangle = 0$. This $O[\sqrt{N}]$ fluctuation of polarization necessarily couples to field, and either zero point fluctuation of field or spontaneously emitted single photon field may stimulate the growth of medium polarization.

The classical development at later stages after quantum initiation is well described by a non-linear coupled set of partial differential equations [13] for medium polarization $R = R_-$, population difference Z , and field envelope E (all functions of time t and x),

$$\partial_t R = -idEZ, \quad (19)$$

$$\partial_t Z = i\frac{d}{2}(ER^* - E^*R), \quad (20)$$

$$(\partial_t + \partial_x)E = i2\pi\omega dnR, \quad (21)$$

where n is the number density of atoms, and ω is the frequency of emitted photon, while d is the dipole moment. This set of equations is often called the Maxwell-Bloch equation. The approximations made are (1) rotating wave approximation (RWA) which omits rapidly oscillating terms in time, (2) slowly varying envelope approximation (SVEA). The initial condition for this set of differential equations is given by random values of initial parameter R well described by a Gaussian distribution of width $2\sqrt{N}$ with N the total number of participating atoms. The mathematical structure of sine-Gordon equation exists for this set of equations, which shall be discussed in Appendix B along with auto-modeling solutions.

Leaving aside the quantum origin, one can thus clarify the spacetime evolution of SR signals, using the classical Maxwell-Bloch equation and taking a Gaussian ensemble of initial data set. Solutions give a large fluctuation of the SR delay time, pulse width, pulse height, and it is only meaningful to compare SR experiments with theory statistically, and not making a shot by shot analysis. Due to the quantum nature of initial stage of SR, the phenomenon is sometimes called superfluorescence(SF) instead of SR.

The super-radiance was first observed in the infrared region of molecular transition [21], and subsequently in the optical region, including excited atoms in solids [13]. It was found later [22] that the delay time may be shortened by irradiation of trigger along the cylinder axis. It is also expected that SR may be controlled to a certain extent. We refer to two references in [13] for more comprehensive discussion on SR.

We show in Fig.7 our Ba experiment. The global features of numerical solutions along with ringing of pulses may be understood by auto-modeling solutions of much simpler ordinary differential equation, as explained in Appendix B.

An interesting and useful point to our RENP project is to view SR as an cooperative enhancement of spontaneous decay in the presence of developed coherence. The simple concept of constant decay rate, namely time independent decay rate per unit time, disappears in the phenomenon of super-radiance, because all atoms in the excited state $|e\rangle$ nearly disappears after the pulse emission and it is meaningless to discuss the latest stage of evolution. Another important point to subsequent discussion is that the mechanism of our (triggered) PSR is more akin to the triggered SR rather than SF. This makes much easier to handle PSR without discussing the stage of quantum initiation as needed for SF. The trigger is essential to assist PSR, since the elementary rate of two photon emission involves an effective coupling in higher order of QED, and the rate becomes $\sim 10^{16}$ sec for para- $H_2Xv = 1$ two-photon decay. The quantum fluctuation of medium polarization coupled to field by a much weaker effective constant than E1 is not sufficient for its macroscopic development caused by fluctuating fields. This is a fortunate aspect to theoretical analysis of PSR dynamics: the semi-classical approach becomes possible in all stages of time evolution for polarization development and amplification by trigger.

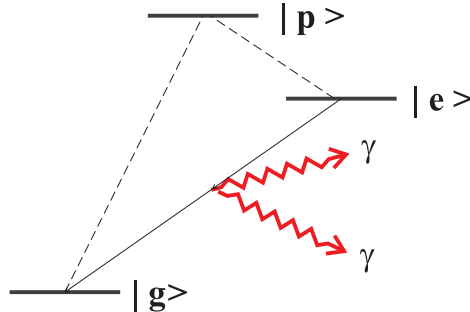


Fig. 8 Level structure for two-photon de-excitation.

2.2. Master equation for paired super-radiance

We now turn to PSR. Consider three level atom (or molecule) of level energies, $\epsilon_p > \epsilon_e > \epsilon_g$, as shown in Fig.8.

When transition between two lower levels, $|e\rangle$ and $|g\rangle$, is dipole forbidden, the dominant de-excitation process of $|e\rangle$ may be two-photon decay $|e\rangle \rightarrow |g\rangle + \gamma\gamma$, It is described in terms of second order, 2×2 matrix hamiltonian [14],

$$\mathcal{H}_I = - \begin{pmatrix} \alpha_{ee} E^+ E^- & e^{i\epsilon_{eg}t} \alpha_{ge} (E^+)^2 \\ e^{-i\epsilon_{eg}t} \alpha_{ge} (E^-)^2 & \alpha_{gg} E^+ E^- \end{pmatrix}, \quad (22)$$

$$\alpha_{ge} = \frac{2d_{pe}d_{pg}}{\epsilon_{pg} + \epsilon_{pe}}, \quad \alpha_{aa} = \frac{2d_{pa}^2 \epsilon_{pa}}{\epsilon_{pa}^2 - \omega^2}, \quad (a = g, e). \quad (23)$$

(A slightly different notation is used from [14].) Here $\epsilon_{ab} = \epsilon_a - \epsilon_b$, $\omega = \epsilon_{eg}/2$. The upper level $|p\rangle$ that has the largest coupling to lower levels, $|e\rangle$ and $|g\rangle$, should be dominant, but other competing intermediate states $|p\rangle$ may also contribute to the hamiltonian \mathcal{H}_I . In the case of trigger for RENP M1 dipole coupling is relevant to one of the two couplings, and d_{pa} is replaced by the magnetic dipole moment μ_{pa} , typically $O(1/100)$ smaller. If we ignore ω dependence, the quantities α_{ab} , $a, b = e, g$ coincide with polarizability. For simplicity we took isotropic medium and linearly polarized fields, taking \vec{E}^\pm as scalar functions E^\pm . The diagonal part $\propto \alpha_{aa}$ of this hamiltonian describes AC Stark energy shifts, while off-diagonal parts $\propto \alpha_{ge}$ are effective coupling for two photon emission and absorption. This hamiltonian (22) has been derived adopting the Markov approximation by eliminating the amplitude of level $|p\rangle$ in the three level ($|e\rangle, |g\rangle, |p\rangle$) system.

The field E is decomposed into positive and negative frequency parts in Eq. 22, and it may contain multi-modes, in particular two counter-propagating modes denoted by E_R, E_L of the same incident frequency, thus $E = E_R + E_L$. It is useful at this point to recall the physical meaning of coupling constants α_{ab} in the interaction hamiltonian. We first note that annihilation (a_i) and creation (a_i^\dagger) operators of photon modes are related to complex fields by $E_i^+ = a_i \sqrt{\omega/2V}$, $E_i^- = a_i^\dagger \sqrt{\omega/2V}$ where V is the quantization volume. The important

equations obtained after SVEA are written in terms of envelope functions:

$$(\partial_t + \partial_x)E_R = \frac{i\omega}{2} \left(\left(\frac{\alpha_{ee} + \alpha_{gg}}{2}n + \frac{\alpha_{ee} - \alpha_{gg}}{2}R_3^{(0)} \right) E_R + \frac{\alpha_{ee} - \alpha_{gg}}{2}R_3^{(+)}E_L \right. \\ \left. + \alpha_{ge} \left((R_1 - iR_2)^{(0)}E_L^* + (R_1 - iR_2)^{(+)}E_R^* \right) \right), \quad (24)$$

$$(\partial_t - \partial_x)E_L = \frac{i\omega}{2} \left(\left(\frac{\alpha_{ee} + \alpha_{gg}}{2}n + \frac{\alpha_{ee} - \alpha_{gg}}{2}R_3^{(0)} \right) E_L + \frac{\alpha_{ee} - \alpha_{gg}}{2}R_3^{(-)}E_R \right. \\ \left. + \alpha_{ge} \left((R_1 - iR_2)^{(0)}E_R^* + (R_1 - iR_2)^{(-)}E_L^* \right) \right). \quad (25)$$

Quantities R_{\pm} in the right hand side are medium polarization and R_3 is the population difference. The right hand sides of these equations give effects, all in bulk medium, of forward scattering $\propto \frac{\alpha_{ee} + \alpha_{gg}}{2}n + \frac{\alpha_{ee} - \alpha_{gg}}{2}R_3^{(0)}$, backward scattering $\propto \frac{\alpha_{ee} - \alpha_{gg}}{2}R_3^{(\pm)}$, RL(right left)- pair annihilation $\propto \alpha_{ge}(R_1 - iR_2)^{(0)}$, and RR(right right)-, LL(left left)-pair annihilation $\propto \alpha_{ge}(R_1 - iR_2)^{(\pm)}$. (The pair creation amplitudes appear in conjugate equations to those above.) We have used quantities $R_i^{(\pm)}e^{\pm 2ikx}$ as defined by decomposition of three major spatially varying components,

$$R_i = R_i^{(0)} + R_i^{(+)}e^{2ikx} + R_i^{(-)}e^{-2ikx}, \quad k = \omega > 0. \quad (26)$$

Quantities $R_i^{(\pm)}e^{\pm 2ikx}$ are what are called spatial grating in the literature of non-linear optics. The backward scattering terms, and RR,- LL-pair annihilation and creation terms are important only in the presence of spatial grating of polarization. Neglect of spatial grating is thus equivalent to retaining forward scattering and RL-pair processes, and ignoring all other terms whose effects represent propagation effects, as noted in [14].

When excitation to the metastable state $|e\rangle$ is done by high quality lasers, there may exist a spatial grating in the initial Bloch vector components, which can be incorporated as the initial condition in our computation. For instance, excitation by R-moving pump laser and R-moving coupling laser may imprint phase factors $e^{i\omega_p(t-x)}$ and $e^{-i\omega_c(t-x)}$ onto target atoms, and give the initial spatial grating $e^{-i(\omega_p - \omega_c)x} = e^{-i\epsilon_{eg}x}$ for target atom at the position x . This case corresponds to the initial grating of $e^{-2i\omega x}$. But even without initial spatial grating two-photon absorption of trigger laser by non-grating components $R_i^{(0)}$ may generate spatial grating terms, which thus requires the enlarged set of dynamical variables including $R_i^{(\pm)}$.

The field equation is to be supplemented by the Bloch equation. In two-photon process this reads as

$$\partial_t R_1 = (\alpha_{ee} - \alpha_{gg})E^+E^-R_2 - i\alpha_{ge}(e^{i\epsilon_{eg}t}E^+E^+ - e^{-i\epsilon_{eg}t}E^-E^-)R_3 - \frac{R_1}{T_2}, \quad (27)$$

$$\partial_t R_2 = -(\alpha_{ee} - \alpha_{gg})E^+E^-R_1 + \alpha_{ge}(e^{i\epsilon_{eg}t}E^+E^+ + e^{-i\epsilon_{eg}t}E^-E^-)R_3 - \frac{R_2}{T_2}, \quad (28)$$

$$\partial_t R_3 = \alpha_{ge} (i(e^{i\epsilon_{eg}t}E^+E^+ - e^{-i\epsilon_{eg}t}E^-E^-)R_1 - (e^{i\epsilon_{eg}t}E^+E^+ + e^{-i\epsilon_{eg}t}E^-E^-)R_2) - \frac{R_3 + n}{T_1}, \quad (29)$$

$$E^{\pm} = E_R^{\pm} + E_L^{\pm}. \quad (30)$$

Explicit decomposition of these equations into different grating according to Eq. 26 is given in [14], using SVEA. We have introduced two relaxation terms inversely proportional to

their time constants $T_i, i = 1, 2$. The origin of these relaxation terms is left untouched, but they may be measured by experimental means. They arise from interaction of subsystem, in this case two states in $|e\rangle, |g\rangle$, with environment reservoir such as a thermal bath. This form is the most general relaxation terms consistent with fundamental principles of quantum mechanics in the two-level problem [19].³ The phase decoherence time T_2 is much smaller and more important than the decay time T_1 , which may be taken infinitely large for our practical purpose.

It is both useful and convenient to introduce dimensionless quantities and write the Maxwell-Bloch equation of our system in terms of these dimensionless quantities. The natural time and length scale determined by the field equation is the inverse of $\alpha_{ab}\omega n$. We shall define this as

$$t_* = \frac{2}{\alpha_{ge}\epsilon_{eg}n}. \quad (31)$$

A somewhat different notation was used in [14]. The natural field scale is then obtained from the Bloch equation as

$$E_*^2 = \frac{1}{\alpha_{ge}t_*} = \epsilon_{eg}n. \quad (32)$$

This E_*^2 is nothing but the energy density stored in the atomic system, when the number density in $|e\rangle$ is equal to n .

It is useful to give numerical values for these quantities. Take the example of para-H₂ molecule and its vibrational two-photon transition $v = 1 \rightarrow 0$ of the electronically ground state. This example gives

$$t_* \sim 1\text{cm} \frac{10^{21}\text{cm}^{-3}}{n} \sim 40\text{ps} \frac{10^{21}\text{cm}^{-3}}{n}, \quad E_*^2 \sim 60\text{GWmm}^{-2} \frac{n}{10^{21}\text{cm}^{-3}}. \quad (33)$$

Our dimensionless time/length and field units are then $(\xi, \tau) = (x/t_*, t/t_*)$, $e_i = E_i/E_*$. The Bloch vector components are rescaled by the target number density, to give the dimensionless quantity $r_i = R_i/n$. The r_3 value 1 means the complete inversion in the level $|e\rangle$, and -1 the target in the ground state $|g\rangle$ completely. The medium polarization $|r_1 \pm ir_2| = 1$ implies the maximal coherence.

We now give the master equation when the spatial grating is present. (the more general equation for two color trigger is given in Appendix). In the dimensionless unit they are

$$\begin{aligned} \partial_\tau r_1^{(0)} &= 4\gamma_- (|e_R|^2 + |e_L|^2) r_2^{(0)} + 8\Im(e_R e_L) r_3^{(0)} + 4\gamma_- e_R e_L^* r_2^{(-)} + 4\gamma_- e_L e_R^* r_2^{(+)} \\ &\quad - 2i(e_L^2 - (e_R^*)^2) r_3^{(+)} - 2i(e_R^2 - (e_L^*)^2) r_3^{(-)} - \frac{r_1^{(0)}}{\tau_2}, \end{aligned} \quad (34)$$

$$\begin{aligned} \partial_\tau r_1^{(+)} &= 4\gamma_- e_R e_L^* r_2^{(0)} - 2i(e_R^2 - (e_L^*)^2) r_3^{(0)} + 4\gamma_- (|e_R|^2 + |e_L|^2) r_2^{(+)} + 8\Im(e_R e_L) r_3^{(+)} - \frac{r_1^{(+)}}{\tau_3}, \\ \partial_\tau r_2^{(0)} &= -4\gamma_- (|e_R|^2 + |e_L|^2) r_1^{(0)} + 8\Re(e_R e_L) r_3^{(0)} - 4\gamma_- e_R e_L^* r_1^{(-)} - 4\gamma_- e_L e_R^* r_1^{(+)} \\ &\quad + 2(e_L^2 + (e_R^*)^2) r_3^{(+)} + 2(e_R^2 + (e_L^*)^2) r_3^{(-)} - \frac{r_2^{(0)}}{\tau_2}, \end{aligned} \quad (35)$$

³ See further below on the relaxation term $\propto 1/T_3$ when spatial grating terms are present.

$$\partial_\tau r_2^{(+)} = -4\gamma_- e_R e_L^* r_1^{(0)} + 2(e_R^2 + (e_L^*)^2) r_3^{(0)} - 4\gamma_- (|e_R|^2 + |e_L|^2) r_1^{(+)} + 8\Re(e_R e_L) r_3^{(+)} - \frac{r_2^{(+)}}{\tau_3}, \quad (36)$$

$$\begin{aligned} \partial_\tau r_3^{(0)} = & -8 \left(\Re(e_R e_L) r_2^{(0)} + \Im(e_R e_L) r_1^{(0)} \right) + 2i(e_R^2 - (e_L^*)^2) r_1^{(-)} + 2i(e_L^2 - (e_R^*)^2) r_1^{(+)} \\ & - 2(e_L^2 + (e_R^*)^2) r_2^{(+)} - 2(e_R^2 + (e_L^*)^2) r_2^{(-)} - \frac{r_3^{(0)} + 1}{\tau_1}, \end{aligned} \quad (37)$$

$$\partial_\tau r_3^{(+)} = 2ir_1^{(0)}(e_R^2 - (e_L^*)^2) - 2r_2^{(0)}(e_R^2 + (e_L^*)^2) - 8 \left(\Re(e_R e_L) r_2^{(+)} + \Im(e_R e_L) r_1^{(+)} \right) - \frac{r_3^{(+)}}{\tau_3}, \quad (38)$$

$$(\partial_\tau + \partial_\xi) e_R = \frac{i}{2}(\gamma_+ + \gamma_- r_3^{(0)}) e_R + \frac{i}{2}\gamma_- r_3^{(+)} e_L + \frac{i}{2}(r_1^{(0)} - ir_2^{(0)}) e_L^* + \frac{i}{2}(r_1^{(+)} - ir_2^{(+)}) e_R^*, \quad (39)$$

$$(\partial_\tau - \partial_\xi) e_L = \frac{i}{2}(\gamma_+ + \gamma_- r_3^{(0)}) e_L + \frac{i}{2}\gamma_- r_3^{(-)} e_R + \frac{i}{2}(r_1^{(0)} - ir_2^{(0)}) e_R^* + \frac{i}{2}(r_1^{(-)} - ir_2^{(-)}) e_L^*, \quad (40)$$

$$\gamma_\pm = \frac{\alpha_{ee} \pm \alpha_{gg}}{2\alpha_{ge}}. \quad (41)$$

Here $\tau_i = T_i/t_*$ are relaxation times in the dimensionless unit. In our previous work two relaxation terms are taken equal; $T_3 = T_2$, but relaxation time T_3 for spatial grating terms may in general differ from the phase de-coherence time T_2 for non-grating terms, as in the equations above.

In the limit of infinite relaxation times the conservation law,

$$\partial_\tau \left((r_1^{(0)})^2 + (r_2^{(0)})^2 + (r_3^{(0)})^2 + 2r_1^{(-)} r_1^{(+)} + 2r_2^{(-)} r_2^{(+)} + 2r_3^{(-)} r_3^{(+)} \right) = 0, \quad (42)$$

holds at any point in the target. Without spatial grating terms, another important conservation law of energy exists in the $T_1 \rightarrow \infty$ (but with finite T_2, T_3) limit. In terms of quantities of physical dimensions, it is

$$\frac{d}{dt} \int_0^L dx \left(\frac{\epsilon_{eg}}{2} R_3^{(0)} + 2(|E_R|^2 + |E_L|^2) \right) = -2[|E_R|^2 - |E_L|^2]_{x=0}^L. \quad (43)$$

This expresses that exchange of energy between field and medium is balanced by a net energy flux at two ends of target. This conservation no longer holds in the presence of spatial grating terms. But correction due to this violation is expected small because the spatially varying factor $e^{\pm 2i\omega x}$ averages out in the spatial integral above.

Finally, we note that the master equation for PSR has the semi-classical nature: PSR phenomena can occur without the quantum initiation unlike SR if the trigger field is irradiated. The master equation may be solved numerically under a variety of initial and boundary conditions. The standard initial-boundary condition (IBC) we use in the present work is the symmetric trigger irradiation in which continuous wave (CW) trigger lasers of counter-propagating directions and the equal frequency are irradiated. One can think of a few interesting cases of IBC for the Bloch vector components such as a complete inversion in $|e\rangle$, and a large phase coherence between the two levels, $|e\rangle$ and $|g\rangle$. It turns out that these two cases give quite different results.

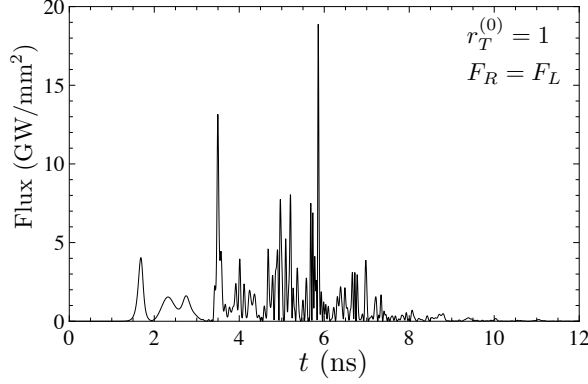


Fig. 9 Time-evolving PSR output fluxes at two target ends, resulting from the symmetric trigger irradiation of the power 1 mWmm^{-2} under the conditions of the target number density $n = 1 \times 10^{21} \text{ cm}^{-3}$, target length = 100cm, relaxation times $T_2 = T_3 = 10, T_1 = 10^3$ ns's, and the initial polarization, $r_T^{(0)} = 1$, all other $r_i = 0$ (no initial grating assumed). About 40 % of the stored energy in the upper level is released from two ends in this example. Vibrational transition $Xv = 1 \rightarrow Xv = 0$ of pH₂ is considered. Right- and left-moving fluxes at two ends are identical.

2.3. Dynamics of PSR

For numerical simulations in this section, we have in mind two types of targets as exemplified by pH₂ and Xe, which has E1 \times E1 and M1 \times E1. These target atoms are candidates for PSR and RENP. Their coupling matrices (α_{ab}) and other important parameters are as follows:

$$\text{pH}_2; \quad \epsilon_{eg} = 0.52 \text{ eV} \quad (44)$$

$$(\alpha_{ab}) = \begin{pmatrix} 0.87 & 0.055 \\ 0.055 & 0.80 \end{pmatrix} 10^{-24} \text{ cm}^3, \quad \frac{1}{t_*} \sim \frac{1}{1 \text{ cm}} \frac{n}{10^{21} \text{ cm}^{-3}},$$

$$\text{Xe}; \quad |e\rangle = 5p^5 ({}^2P_{3/2}) 6s^2 [3/2]_2, \quad |g\rangle = 5p^6 {}^1S_0, \quad |p\rangle = 5p^5 ({}^2P_{3/2}) 6s^2 [3/2]_1, \quad (45)$$

$$\epsilon_{eg} = 8.3153 \text{ eV}, \quad \epsilon_{pe} = 0.1212 \text{ eV}, \quad \gamma_{pg} = 0.28 \text{ GHz},$$

$$(\alpha_{ab}) = \begin{pmatrix} -2.6 \times 10^{-9} & 0.47 \times 10^{-3} \\ 0.47 \times 10^{-3} & 6.9 \end{pmatrix} 10^{-24} \text{ cm}^3, \quad \frac{1}{t_*} \sim \frac{1}{8 \text{ cm}} \frac{n}{10^{21} \text{ cm}^{-3}}.$$

Coupling parameters α_{ab} for pH₂ are given by the polarizability which is justified when $\omega \ll \epsilon_{eg}$ [14].

Results for fields and Bloch vector components have been numerically computed. Previous computations [14] have been done without taking into account effects of spatial grating.

We first compare in Fig. 9 and Fig. 10 results of two calculations; one with spatial grating modes included as dynamical variables and another without them, in both cases assuming no initial grating modes. Results show a quantitative difference, but qualitatively they show similar behaviors of time evolution. In any event it seems difficult to experimentally resolve this level of temporal features. All the rest of illustrated outputs are results including grating modes as dynamical variables.

We present in Fig. 9 ~ Fig. 13 (see also Fig. 4 in Sec.1), numerical results for pH₂, including the spatial grating effect. The quantity $r_T^{(i)} = r_1^{(i)} + ir_2^{(i)}$ is defined for the total polarization

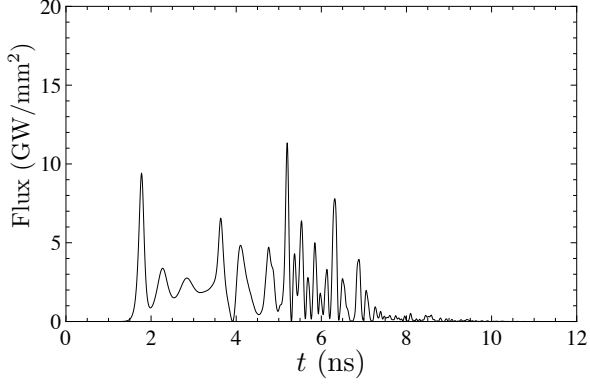


Fig. 10 Flux outputs when spatial grating terms are absent, using the same parameter set of Fig. 9

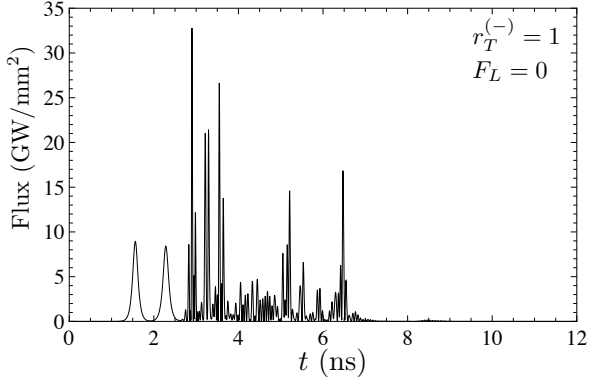


Fig. 11 Time-evolving PSR right moving output (left moving flux negligibly small), resulting from the symmetric trigger irradiation of the power 1 mWmm^{-2} under the conditions of the target number density $n = 1 \times 10^{21} \text{ cm}^{-3}$, target length = 100cm, relaxation times $T_2 = T_3 = 10, T_1 = 10^3$ ns's, and the initial polarization of fully grating mode, $r_T^{(-)} = 1$, all other $r_i = 0$. About 30 % of the stored energy is released in this case. Vibrational transition $Xv = 1 \rightarrow Xv = 0$ of pH₂ is considered.

of initial state in these computations. Results of different initial conditions for the spatial grating are shown; (1) case of full spatial grating without homogeneous component of the coherence, (2) case of null spatial grating, (3) mixture of grating and homogeneous components. With full grating and without any homogeneous component the output shows the greatest left-right (LR) asymmetry, a one-sided flux despite of LR symmetric trigger irradiation. The directionality of the output flux satisfies the phase matching or the momentum conservation assuming that the imprinted grating effectively gives medium a momentum. The excitation laser is expected to imprint a certain level of spatial grating, and it would be important to control this grating for determining the asymmetry of outputs.

The space-time evolution of Bloch vector components are shown in Fig.13. It is striking that even after dephasing times T_2, T_3 interesting spatial structures remain finite, suggesting

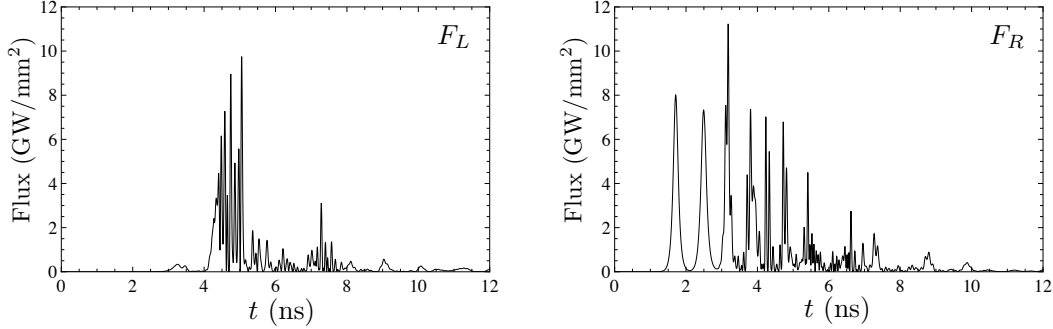


Fig. 12 Time-evolving PSR output fluxes at the left target end in the left panel and at the right end in the right panel, resulting from the symmetric trigger irradiation at two target ends of the power 1 mWmm^{-2} under the conditions of the target number density $n = 1 \times 10^{21} \text{ cm}^{-3}$, target length = 100cm, relaxation times $T_2 = T_3 = 10, T_1 = 10^3 \text{ ns}'s$, and the initial polarization, $r_T^{(-)} = 0.9, r_T^{(0)} = 0.1$, all other $r_i = 0$. About 20% from the right and 10% from the left of the stored energy are released. Vibrational transition $Xv = 1 \rightarrow Xv = 0$ of pH_2 is considered.

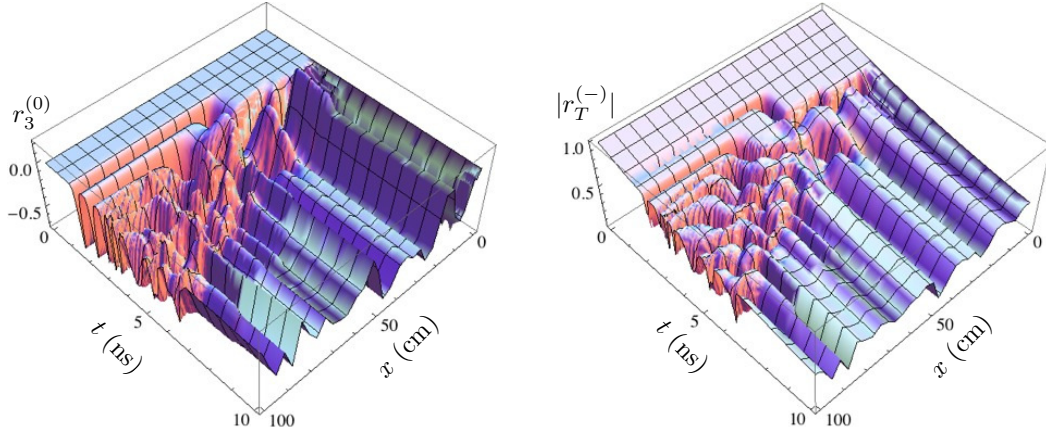


Fig. 13 Space-time diagram of grating and non-grating Bloch vector components corresponding to the parameter choice of Fig. 11.

that explosive PSR event alone is not the whole story of macro-coherent two-photon process. Below we shall discuss static or steady state solutions of the Maxwell-Bloch system.

Summarizing outputs, we may say that effects of grating modes are large when initial grating modes are present, but when they are absent, differences are minor.

The local quantity defined by $|\vec{E}^-(R_1 - iR_2)|^2/(4\epsilon_{eg}n^3)$ at each site within the target expresses a potentiality of PSR emission, which shall be reflected in fluxes at two ends in later times. The spatial integration of this local quantity is denoted by $\eta_\omega(t)$, which gives an instantaneous potentiality of PSR activity. This global function is illustrated in Fig.14 up to a time of order T_2 . The time duration of the plateau region roughly gives the duration of explosive PSR emission.

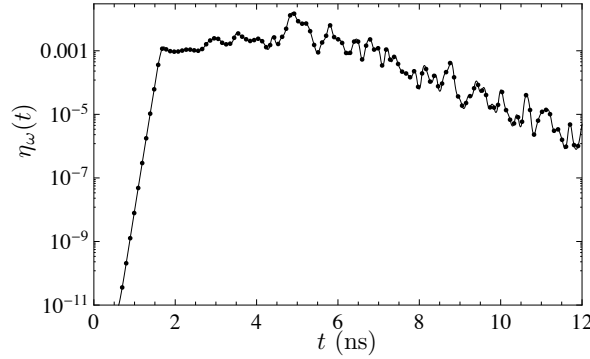


Fig. 14 Potentiality of PSR emission given by the spatial integral of $|\vec{E}^-(R_1 - iR_2)|^2/(4\epsilon_{eg}n^3)$ corresponding to the parameter set of Fig.9.

In Sec. 4 we show the case of weak PSR outputs in which the output flux is linearly proportional to the trigger flux. There is a set of threshold parameters that divides the explosive and the linear PSR events. But due to a high level of non-linearity it is difficult to locate this threshold exactly.

The results so far are outputs for pH₂. Xe results have different aspects, since their two-photon coupling is caused by M1×E1, much weaker than E1×E1 of pH₂ vibrational transition.

3. Theory of macro-coherent radiative emission of neutrino pair (RENP)

In this section, we present a theory of RENP [8], [9] and numerical results based on theoretical formulas thus derived. The RENP process is treated in the second-order perturbation of QED and the weak four Fermi interaction, while the time evolution of the electromagnetic field in the target medium is dealt with non-perturbatively in the semi-classical approximation. A Feynman-like diagram of the elementary RENP process is depicted in Fig. 15, in which the nuclear Coulomb interaction is emphasized. The non-perturbative part requires numerical solutions of the master equation of Maxwell-Bloch type under two color trigger irradiation.

In Appendix A a brief description of electroweak interaction of atomic electron is given, which is the basis of our following computations.

3.1. Coherent neutrino pair emission from atoms / molecules

We begin with a description of the elementary process $|e\rangle \rightarrow |g\rangle + \gamma(\vec{k}) + \nu_i(\vec{p}) + \bar{\nu}_j(\vec{p}')$, in which an electron bounded in an atom of the macroscopic target undergoes the QED and weak interactions. The amplitude is expressed as

$$\mathcal{A}_{ij} = \frac{i\mathcal{M}_d\mathcal{M}_W^{ij}}{\epsilon_{pg} - \omega} e^{-i(\vec{k} + \vec{p} + \vec{p}') \cdot \vec{x}_a} (2\pi) \delta(\epsilon_{eg} - \omega - E_p - E_{p'}), \quad (46)$$

where $\epsilon_{pg} = \epsilon_p - \epsilon_g$, $\omega = |\vec{k}|$ is the energy of the photon, $\mathcal{M}_{d(W)}$ denotes the E1 (weak) matrix element and the possible sum over the intermediate state $|p\rangle$ is to be understood. We assume that the transition between $|e\rangle$ and $|p\rangle$ is the M1 type responsible to the neutrino pair

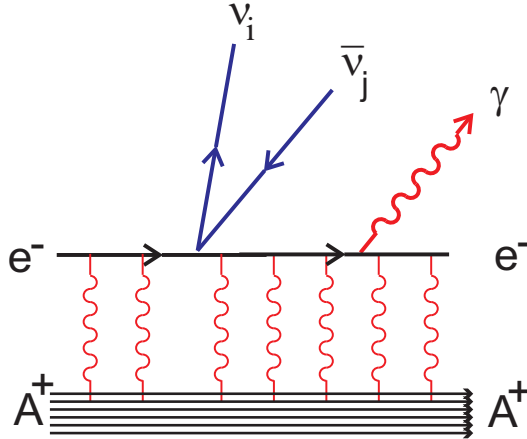


Fig. 15 RENP process. The many wavy lines between e^- and A^+ represent frequent Coulomb interaction between atomic electron and nucleus.

emission and that between $|p\rangle$ and $|g\rangle$ is the E1 type responsible for the photon emission. We explicitly show the dependence on the position of the target atom \vec{x}_a in Eq. 46.

For an ensemble of atoms, the total amplitude is the superposition of the contributions from all the atoms and proportional to $\sum_a \exp[-i(\vec{k} + \vec{p} + \vec{p}') \cdot \vec{x}_a]$. For a macroscopic ensemble of N atoms with a volume V , this summation approximates to $(N/V)(2\pi)^3 \delta^3(\vec{k} + \vec{p} + \vec{p}')$, which means the momentum conservation among the emitted photon and the neutrino pair in addition to the energy conservation represented by the δ function in Eq. 46. Thus, the kinematic configuration that satisfies the momentum conservation acquires an extra enhancement in the rate. This is the essence of the macro-coherent amplification mechanism.

Due to the energy-momentum conservation, the RENP process with the macro-coherence resembles a relativistic three-body decay of the parent particle of mass ϵ_{eg} into a photon and a pair of neutrinos. However, the energy and the momentum of the photon are dictated by the classical radiation field induced by the trigger laser. Therefore, the emitted photon has no phase space and we do not have to introduce the three-body phase space. Thus, the differential rate of the process for a macroscopic ensemble of atoms is written as

$$d\Gamma_{ij} = n^2 V \frac{|\mathcal{M}_d \mathcal{M}_W^{ij}|^2}{(\epsilon_{pg} - \omega)^2} d\Phi_2, \quad (47)$$

where n is the number density of atoms, $d\Phi_2$ represents the Lorentz invariant two-body phase space of the neutrino pair, and the summations over the atomic spin states and the neutrino helicities are implicit. The explicit form of $d\Phi_2$ is given by

$$d\Phi_2 = (2\pi)^4 \delta^4(q - p - p') \frac{d^3 p}{(2\pi)^3 2E_p} \frac{d^3 p'}{(2\pi)^3 2E_{p'}}, \quad (48)$$

where $E_{p^{(\prime)}} = \sqrt{m_{i(j)}^2 + \vec{p}^{(\prime)2}}$ is the neutrino energy of mass $m_{i(j)}$ and $q^\mu = (\epsilon_{eg} - \omega, -\vec{k})$ represents the four momentum of the neutrino pair.

The E1 matrix element is defined as $\mathcal{M}_d = -\langle g | \vec{d} | p \rangle \cdot \vec{E}$ with \vec{E} being the radiation field developed in the target by the trigger laser irradiation, while the weak matrix element is

expressed by

$$\mathcal{M}_W^{ij} = \frac{G_F}{\sqrt{2}} \langle \nu_i(p, \lambda) \bar{\nu}_j(p', \lambda') | \sum_{a,b} \bar{\nu}_a \gamma_\mu (1 - \gamma_5) \nu_b | 0 \rangle (v_{ab} J_V^\mu - a_{ab} J_A^\mu), \quad (49)$$

where the atomic vector (axial-vector) current $J_V^\mu (J_A^\mu)$ is defined by $J_V^\mu = \langle g | \bar{e} \gamma^\mu e | p \rangle$ ($J_A^\mu = \langle g | \bar{e} \gamma^\mu \gamma_5 e | p \rangle$). Coefficients v_{ab} and a_{ab} are given in terms of elements of neutrino mass matrix, as given by Eq. A12 of Appendix A. In the non-relativistic approximation for the atomic wave functions, $J_V^\mu \simeq 0$ and $J_A^\mu \simeq (0, 2\langle p | \vec{S} | e \rangle)$ in the rest frame of the atomic system. Hence, we neglect J_V^μ hereafter. Evaluating the neutrino matrix element, we obtain

$$\mathcal{M}_W^{ij} = -\frac{G_F}{\sqrt{2}} \left(a_{ij} L_{ij}^\mu - \delta_M a_{ji} R_{ij}^\mu \right) J_{A\mu}, \quad (50)$$

where

$$L_{ij}^\mu (R_{ij}^\mu) = \bar{u}_i(p, \lambda) \gamma^\mu (1 \mp \gamma_5) v_j(p', \lambda'), \quad (51)$$

and $\delta_M = 0(1)$ for Dirac(Majorana) neutrinos. The left-handed current L_{ij}^μ , which comes from $(a, b) = (i, j)$ in Eq. 49, is common for both Dirac and Majorana cases; while the right-handed current R_{ij}^μ from $(a, b) = (j, i)$ with the use of the relation between the four-component spinor, $C\bar{u}^T = v$, is allowed only for the latter case. Technically, this chirality flip is understood as a property of the charge conjugation operation in the Dirac theory.

The square of the weak amplitude Eq. 50 consists of four terms: $L_{ij}^\mu L_{ij}^{\dagger\nu}$, $R_{ij}^\mu R_{ij}^{\dagger\nu}$, $L_{ij}^\mu R_{ij}^{\dagger\nu}$ and $R_{ij}^\mu L_{ij}^{\dagger\nu}$. The sum over the neutrino helicities and momenta leads to

$$\begin{aligned} \int d\Phi_2 \sum_{\lambda, \lambda'} L_{ij}^\mu L_{ij}^{\dagger\nu} &= \int d\Phi_2 \sum_{\lambda, \lambda'} R_{ij}^\mu R_{ij}^{\dagger\nu} \\ &= \frac{\Delta_{ij}}{6\pi} \left[\left\{ \Delta_{ij}^2 - 3 \left(1 - \frac{m_i^2 + m_j^2}{q^2} \right) \right\} q^2 g^{\mu\nu} + 2 \left\{ 1 + \frac{m_i^2 + m_j^2}{q^2} - 2 \frac{(m_i^2 - m_j^2)^2}{q^4} \right\} q^\mu q^\nu \right] \quad (52) \end{aligned}$$

$$\int d\Phi_2 \sum_{\lambda, \lambda'} L_{ij}^\mu R_{ij}^{\dagger\nu} = \int d\Phi_2 \sum_{\lambda, \lambda'} R_{ij}^\mu L_{ij}^{\dagger\nu} = -\frac{\Delta_{ij}}{\pi} m_i m_j g^{\mu\nu}, \quad (53)$$

where

$$\Delta_{ij}^2 = 1 - 2 \frac{m_i^2 + m_j^2}{q^2} + \frac{(m_i^2 - m_j^2)^2}{q^4}, \quad (54)$$

and $q^2 = \epsilon_{eg}(\epsilon_{eg} - \omega)$ is the invariant mass of the neutrino pair. The cross terms Eq. 53 exhibit the identical particle effect inherent in Majorana neutrinos. They arise from the interference of two currents of different chirality L_{ij}^μ and R_{ij}^μ defined in Eq. 51 and disappear in the massless limit as it should.

Thus, taking the statistical factor for the Majorana case into account, the single photon spectral rate at frequency ω from the position x of unpolarized targets is given by

$$d\Gamma_{\gamma 2\nu}(\omega, x, t) = \frac{G_F^2 V dx}{6\pi L} \left| \vec{E}^-(\omega, x, t) \frac{R_1(x, t) - iR_2(x, t)}{2} \right|^2 C_{eg}(\omega) F(\omega) \quad (55)$$

$$C_{eg}(\omega) = \sum_p \frac{\langle g | \vec{d} | p \rangle \cdot \langle p | \vec{d} | g \rangle \langle e | \vec{S} | p \rangle \cdot \langle p | \vec{S} | e \rangle}{(\epsilon_{pg} - \omega)^2} \quad (56)$$

$$F(\omega) = \sum_{ij} \Delta_{ij} (B_{ij} I_{ij}(\omega) - \delta_M B_{ij}^M m_i m_j) \theta(\omega_{ij} - \omega), \quad B_{ij} = |a_{ij}|^2, \quad B_{ij}^M = \Re(a_{ij}^2), \quad (57)$$

$$I_{ij}(\omega) = \frac{q^2}{6} \left[2 - \frac{m_i^2 + m_j^2}{q^2} - \frac{(m_i^2 - m_j^2)^2}{q^4} \right] + \frac{\omega^2}{9} \left[1 + \frac{m_i^2 + m_j^2}{q^2} - 2 \frac{(m_i^2 - m_j^2)^2}{q^4} \right], \quad (58)$$

where $\vec{E}^-(\omega, x, t) = \vec{E}_R^- + \vec{E}_L^-$ is the negative energy part of right- and left-moving fields within the target developed from trigger laser of frequency $\omega < \epsilon_{eg}/2$ and is limited in its magnitude by the maximum energy stored in the target, $|\vec{E}|^2 \leq \epsilon_{eg} n$.

We note that the rate $d\Gamma_{\gamma 2\nu}$ is proportional to the space-time dependent factor,

$$\left| \vec{E}^- \frac{R_1 - iR_2}{2} \right|^2, \quad (59)$$

which signifies how much the field-medium system has been activated in favor of RENP. It is thus important to obtain this factor as large as possible in the target. We define the following dimensionless quantity to express the field-medium activity for RENP,

$$\eta_\omega(\xi, \tau) = \frac{1}{\epsilon_{eg} n^3} \left| \vec{E}^- \frac{R_1 - iR_2}{2} \right|^2 = \left| \left(e_R^* e^{-i\omega t_* \xi} + e_L^* e^{i\omega t_* \xi} \right) \frac{r_1 - ir_2}{2} \right|^2, \quad (60)$$

where $(\xi, \tau) = (x/t^*, t/t^*)$ with t_* given in Eq.31, the slowly varying dimensionless envelope functions $e_{R,L}(\xi, \tau)$ are introduced as

$$E^- = \sqrt{\epsilon_{eg} n} \{ e_R^* e^{i\omega t_* (\tau - \xi)} + e_L^* e^{i\omega t_* (\tau + \xi)} \}, \quad (61)$$

and the dimensionless Bloch vector components $r_i(\xi, \tau)$ are defined by $R_i = nr_i$. Further, using the grating modes $r_i = r_i^{(0)} + r_i^{(+)} e^{2ikt_* \xi} + r_i^{(-)} e^{-2ikt_* \xi}$, we obtain

$$\eta_\omega(\xi, \tau) = \eta_\omega^R(\xi, \tau) + \eta_\omega^L(\xi, \tau), \quad (62)$$

where

$$\eta_\omega^{R(L)}(\xi, \tau) = \frac{1}{4} \left[|e_{R(L)}|^2 (|r_T^{(0)}|^2 + |r_T^{(+)}|^2 + |r_T^{(-)}|^2) + \Re \{ e_R^* e_L (r_T^{(0)*} r_T^{(+)} + r_T^{(0)} r_T^{(-)*}) \} \right] \quad (63)$$

with $r_T^{(0,\pm)} = r_1^{(0,\pm)} + ir_2^{(0,\pm)}$. We expect that the η factor weakly depends on the frequency ω as is described below.

The formula here gives rate of a kind of stimulated emission from the developed trigger laser of field strength $|\vec{E}|^2$. Although both the energy and the momentum is conserved at the level of elementary process, the phase space factor is different from a typical electron spectral shape of three body decay into almost massless particles such as the muon decay, since the quantity $|\vec{E}|^2$ here is replaced by a kinematic factor $\propto \omega$ (electron energy) in the muon decay. Thus, the photon spectral rate as a function of ω is markedly different in the small energy region from that of muon decay. Near the neutrino pair threshold region

the spectrum resembles that of muon decay, although the difference reflects effects of finite neutrino masses.

As stated in Section 1, RENP may occur at any point of target since even condensate or soliton formation, capable of blocking PSR, cannot stop RENP. RENP is a bulk process, while PSR occurs only at target ends after soliton formation. The total RENP rate observed at both ends of the target is given by integrating Eq. (55) over x . As a result, assuming the sum over possible intermediate states is dominated by a single state $|p\rangle$, we obtain

$$\Gamma_{\gamma 2\nu}(\omega, t) = \Gamma_0 I(\omega) \eta_\omega(t), \quad (64)$$

$$\Gamma_0 = \frac{3n^2 V G_F^2 \gamma_{pg} \epsilon_{eg} n}{2\epsilon_{pg}^3} (2J_p + 1) C_{ep}, \quad (65)$$

where $I(\omega) = F(\omega)/(\epsilon_{pg} - \omega)^2$, and γ_{pg} denotes the E1 transition rate from $|p\rangle$ to $|g\rangle$. The atomic spin factor C_{ep} is defined by

$$\frac{1}{2J_e + 1} \sum_{M_e} \langle pM_p | \vec{S} | eM_e \rangle \cdot \langle eM_e | \vec{S} | pM'_p \rangle = \delta_{M_p M'_p} C_{ep}, \quad (66)$$

and $C_{ep} = 2/3$ for Xe atom. The dynamical factor $\eta_\omega(t)$ is given by

$$\eta_\omega(t) = \eta_\omega^R(t) + \eta_\omega^L(t), \quad (67)$$

where

$$\eta_\omega^R(t) = \frac{t_*}{4L} \int_0^{L/t_*} \eta_\omega^R(\xi, t/t_* - L/t_* + \xi) d\xi, \quad (68)$$

and

$$\eta_\omega^L(t) = \frac{t_*}{4L} \int_0^{L/t_*} \eta_\omega^L(\xi, t/t_* - \xi) d\xi, \quad (69)$$

correspond to the rates at the right and left ends respectively. The overall rate Γ_0 has a dimension in 1/time, while $I(\omega)$ and $\eta_\omega(t)$ are dimension-less.

A nice feature of the formula Eq. 64 is that one can separate the spectral feature given by $I(\omega)$ that serves to determine neutrino properties from the absolute rate Γ_0 and the dynamical factor $\eta_\omega(t)$. The time dependent function $\eta_\omega(t)$ is sensitive to how the initial coherence between $|e\rangle$ and $|g\rangle$ has been prepared and to the quality of trigger laser. Indeed, calculation of $\eta_\omega(t)$ requires numerical solutions of the master equation. We thus discuss two issues, the spectral shape and the overall dynamical rate factor, separately in the following.

The limit of massless neutrinos gives the spectral form,

$$I(\omega; m_i = 0) = \frac{\omega^2 - 6\epsilon_{eg}\omega + 3\epsilon_{eg}^2}{12(\epsilon_{pg} - \omega)^2}, \quad (70)$$

where the prefactor of $\sum_{ij} B_{ij} = 3/4$ is calculated using the unitarity of the neutrino mixing matrix. On the other hand, near the threshold these functions has the behavior of $\Delta_{ij}(\omega) \propto \sqrt{\omega_{ij} - \omega}$.

In what follows we first calculate numerically (analytic results are of little use to experimental design) the spectral shape $I(\omega)$ for two target candidates, Xe atom and I_2 molecule, which greatly differ in their available energies, 8.32 eV (Xe) and 0.88 eV (I_2 relevant vibrational transition). These two targets have been selected for their large $M1 \times E1$ couplings and their large difference in closeness to the minimum expected mass of neutrino heaviest pair ~ 0.1 eV. This makes it possible to determine the relative easiness of undetermined neutrino parameters in realistic experiments.

Table 1 The threshold weight $B_{ij} = |a_{ij}|^2 = |U_{ei}^* U_{ej} - \delta_{ij}/2|^2$.

B_{11}	B_{22}	B_{33}	$B_{12} + B_{21}$	$B_{23} + B_{32}$	$B_{31} + B_{13}$
$(c_{12}^2 c_{13}^2 - 1/2)^2$	$(s_{12}^2 c_{13}^2 - 1/2)^2$	$(s_{13}^2 - 1/2)^2$	$2c_{12}^2 s_{12}^2 c_{13}^4$	$2s_{12}^2 c_{13}^2 s_{13}^2$	$2c_{12}^2 c_{13}^2 s_{13}^2$
0.0311	0.0401	0.227	0.405	0.0144	0.0325

3.2. Neutrino properties extractable from the photon spectrum

Recent reactor and T2K experiments have given compelling evidence for a sizable θ_{13} , which determines relative weights of neutrino pair emission thresholds in our RENP process. Here we summarize the neutrino parameters employed in the following numerical calculation:⁴

$$\Delta m_{21}^2 = 7.5 \times 10^{-5} \text{ eV}^2, \quad |\Delta m_{31(32)}^2| = 2.32 \times 10^{-3} \text{ eV}^2, \quad (71)$$

$$\sin^2 \theta_{12} = 0.31, \quad \sin^2 \theta_{13} = 0.025, \quad \sin^2 \theta_{23} = 0.42, \quad (72)$$

for the NH(IH) case. It is useful to recall weight factors Table(1) given in reference [12]. These absolute weights are applied to the Dirac neutrino pair production, while the rate of the Majorana neutrino pair production at the crossed channel $\omega_{ij}, i \neq j$ contains the additional term proportional to B_{ij}^M in Eq. 57, which depends on Majorana phase combinations,

$$\cos 2\alpha, \quad \cos 2(\beta - \delta), \quad \cos 2(\alpha - \beta + \delta), \quad (73)$$

at (1,2), (1,3) and (2,3) thresholds.

On the other hand, the threshold locations are separated by energy differences $\epsilon_{eg}/2 - \omega_{ij} = (m_i + m_j)^2/2\epsilon_{eg}$. Hence the separation becomes larger as the atomic energy ϵ_{eg} is smaller for fixed neutrino masses. A numerical illustration of the threshold locations is given below for Xe atom in Fig.17.

3.2.1. Absolute masses and mass hierarchy. Experiments are easier when detectable rates are larger. The single photon spectral rates for macro-coherent RENP are larger for larger available energy if dipole and spin matrix elements are the same. Thus, we first calculate RENP rate for Xe which has a large energy difference between the first excited state, as seen in Fig. 16, which is metastable, and the ground state. The overall rate for Xe is estimated as $\Gamma_0 \sim 1 \text{ Hz} (n/10^{22} \text{ cm}^{-3})^3 (V/10^2 \text{ cm}^3)$.

In Fig. 17, we show the threshold locations, that is, the threshold displacements from the maximal photon energy for the massless neutrinos, as functions of the lightest neutrino mass. The multiplet structure is clear: a triplet, a doublet and a singlet for the NH case and the ordering of the multiplets is inverted for the IH case. Since the energy resolution of trigger lasers is not worse than $O(10^{-6}) \text{ eV}$, the identification of thresholds is possible provided that we have a sufficient statistics of data. The expected number of events at each threshold is proportional to the corresponding weight factor shown in Table 1. The threshold of (1,2) has the largest weight and (3,3) is the second one. Observing these thresholds, we will be able to determine the corresponding neutrino masses and examine their consistency with the known mass squared differences.

⁴ These values are slightly different from those quoted in Eq.2. The main conclusions in this section should not be affected by these differences.

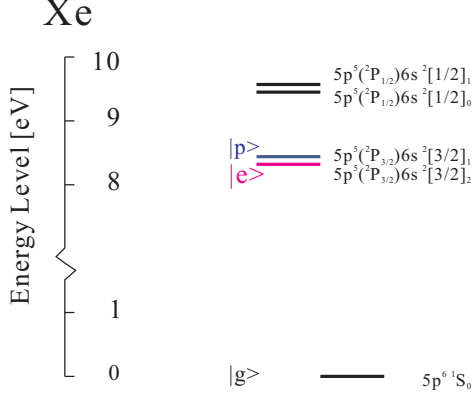


Fig. 16 Xe energy level diagram for RENP experiment.

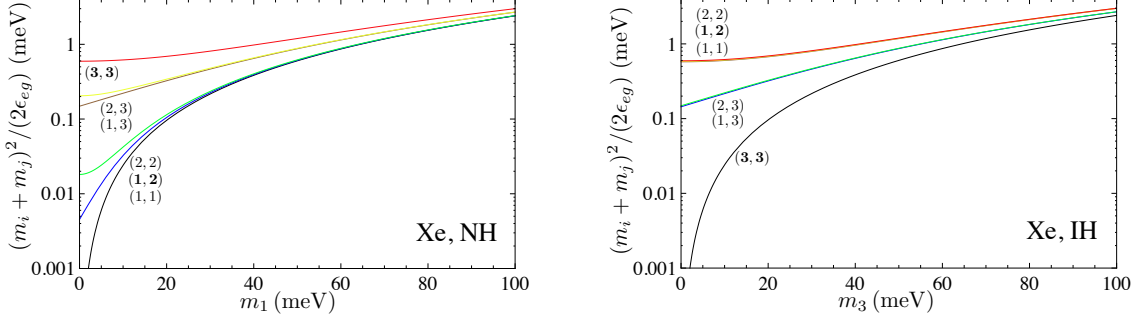


Fig. 17 The locations of the six thresholds, the distances in energy from the half of level difference $\epsilon_{eg}/2$ given in meV unit, as functions of the smallest neutrino mass for the case of Xe atom. The left(right) panel shows the NH(IH) case. The pairs of numbers in parentheses indicate the thresholds and two prominent thresholds are printed in the bold font: (1,1) in black, (1,2) in blue, (2,2) in green, (1,3) in brown, (2,3) in yellow and (3,3) in red for the NH case; (3,3) in black, (1,3) in blue, (2,3) in green, (1,1) in brown, (1,2) in yellow and (2,2) in red for the IH case.

The global spectral feature of RENP from Xe $J = 2$ excited state $5p^5(^2P_{3/2})6s^2[3/2]_{J=2}$ is shown in Fig. 18, while the enlarged threshold region is shown in Fig. 19. The locations of the thresholds corresponding to the three values of the smallest neutrino mass m_0 differ substantially. This feature can be used to determine the absolute neutrino mass.

There are two dominant thresholds and they are supposed to be identified in a relatively earlier stage of experiment. The most significant threshold comes from the emission of the neutrino pair (1,2) and the second one is due to the (3,3) pair in both the NH and IH cases. The relative strength of these two thresholds is a powerful tool to determine the hierarchy pattern: The threshold at higher photon energy is stronger than the one at lower energy in the NH case. While the former is weaker than the latter in the IH case.

3.2.2. Dirac or Majorana. Although Xe gives a good chance of determining the overall neutrino mass scale or the largest neutrino mass, along with distinction of IH and NH, it would be too demanding to differentiate Majorana neutrinos from Dirac neutrinos in Xe

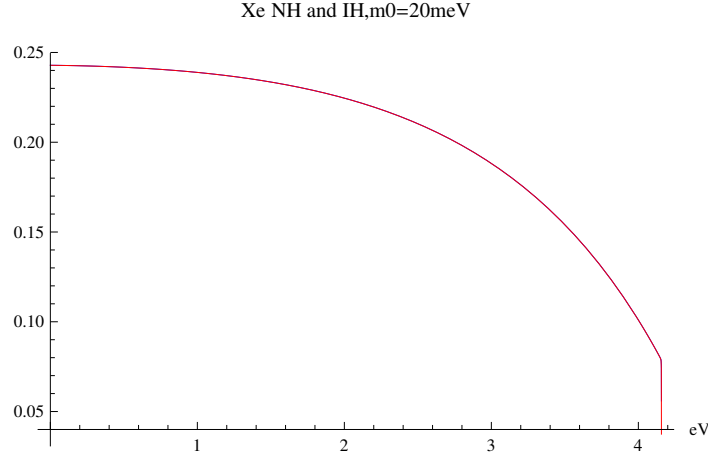


Fig. 18 Xe RENP spectrum $I(\omega)$. In this global plot, the NH and IH spectra completely overlap each other, and it is difficult to extract neutrino parameters.

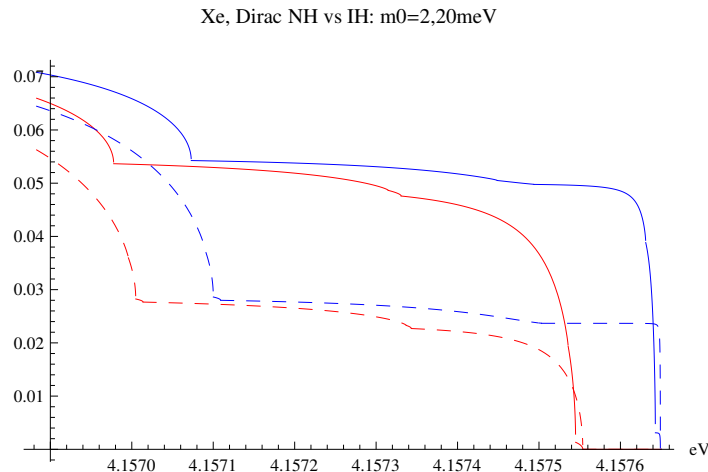


Fig. 19 Xe RENP spectrum $I(\omega)$ in the threshold regions, using values of the smallest neutrino mass, 2 and 20 meV, for two cases of IH (in dashed curves) and NH (in solid).

experiment, since their rate difference due to the interference term is too small in this case. We may characterize Xe RENP measurement as the first generation RENP experiment, since it serves to identify the process itself along with determination of an important neutrino parameter, the largest neutrino mass, although there are better targets for determination of other neutrino parameters.

In a recent paper [12] it was suggested that a smaller available energy of a fraction of eV, but still much larger 0.1 eV, might work for Dirac vs Majorana distinction. A candidate target is I_2 molecule, which has about 1/10 of Xe available energy. The I_2 RENP experiment can be characterized by the next generation experiment of precision neutrino mass spectroscopy.

Before presenting RENP spectral shape from I_2 molecule, it might be instructive to comment on molecular energy levels and their associated wave functions [17]. As is well known, di-atomic molecules have vibrational and rotational energies associated with relative atomic

Table 2 I₂ parameters.

Electronic state of I ₂	D_e (eV)	T_e (eV)	r_e (10 ⁻⁸ cm)	ω_e (cm ⁻¹)
X 0 ⁺ (¹ Σ_g^+)	1.556	0	2.666	214.5
A' 2u(³ Π_u)	0.311	1.245	3.079	108.8
A 1u(³ Π_u)	0.203	1.353	3.129	88.3

motion besides electronic motions. Electronic, vibrational, and rotational energies are well separated due to three well separated velocities. This makes it possible to compute electronic energy levels assuming fixed positions of two nuclei, leading to the concept of the potential energy curve of each electronic configuration as a function of nuclear distance. Near the equilibrium position of nuclei the potential curve may be approximated by a harmonic function whose frequency ω_v gives energy levels of harmonic oscillator $\omega_v(v + 1/2)$. We must deal with two potential curves corresponding to two different electronic configurations, both for M1 and E1 transitions. This gives two overlapping integrals of vibrational wave functions. Each of these overlaps is called the Franck-Condon (FC) factor and calculated assuming relevant vibrational quantum numbers of respective electronic configuration. Some rudimentary example of these is illustrated in Appendix, using the Morse potential for vibrational motion. A work is in progress for accurate computation of relevant potential curves for I₂, in collaboration with theoretical chemists [24].

We have found that three relevant electronic states for RENP are X (electronically ground state) for $|g\rangle$, A' (metastable state) for $|e\rangle$, and the largest overlap comes from A ($|p\rangle$). Their experimental data are taken from experimental values tabulated in Table 2. They are also used to construct the Morse potential in Appendix.

Here the energy unit 1cm⁻¹ = 1/8065.73eV is used for the curvature of the potential curve. The dissociation energy D_e is the energy difference between the potential minimum at T_e and level at dissociated atoms. Conceptual diagram of relevant potential curves that fit to these experimental data is shown in Fig. 20.

We show a threshold feature of RENP photon spectra for the transition between A'v=1 and Xv=15 of I₂ in Fig. 3. Although the difference in the spectral rates between Dirac and Majorana is not so significant even in I₂, it is possible to discriminate between them in principle.

3.2.3. CP violating phases. The rates of emission of $\nu_1\nu_3$ and of $\nu_2\nu_3$ are suppressed by the weights $B_{13} + B_{31} = 0.033$ and $B_{23} + B_{32} = 0.014$, respectively. Thus, it is most advantageous to obtain information on the Majorana phase α at the (1,2) threshold, provided that the corresponding interference term is not suppressed by the smallness of the factor m_1m_2 .

We note that a linear combination of the CP violating phases given in Eq. 73 enter into the expression for the effective Majorana mass measurable in the neutrinoless double beta decay:

$$\begin{aligned}
 \left| \sum_i m_i U_{ei}^2 \right|^2 &= 5.8 \times 10^{-4} m_3^2 + 9.2 \times 10^{-2} m_2^2 + 4.5 \times 10^{-1} m_1^2 + 4.1 \times 10^{-1} m_1 m_2 \cos(2\alpha) \\
 &\quad + 3.2 \times 10^{-2} m_1 m_3 \cos(2(\beta - \delta)) + 1.5 \times 10^{-2} m_2 m_3 \cos(2(\alpha - \beta + \delta)), \quad (74)
 \end{aligned}$$

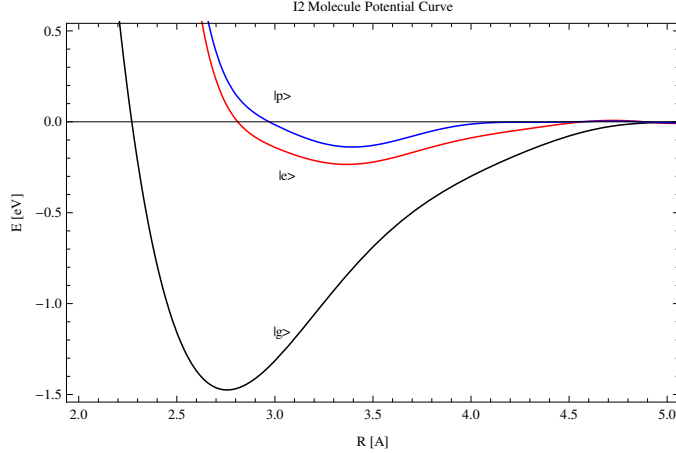


Fig. 20 Conceptual diagram of potential curves of relevant electronic states of I_2 for RENP; $|e\rangle = A'$, $|g\rangle = X$, $|p\rangle = A$. Vibrational levels are suppressed for simplicity. The curves are drawn based on [25].

where the values given in Eq. 1 are used for the mixing angle parameters. The RENP experiment has an advantage of independently determining all three CP factors Eq. 73 instead of their single linear combination.

Sensitivity to the CP violating phases in I_2 RENP spectrum is not as great as one might have expected, but differences for different parameter sets (α, β) reaches several to 10% for the inverted hierarchy case, as seen in Fig.3 of Section 1. For measurements of CP phases in the NH case one should perhaps look for better candidate targets of smaller available energy than I_2 .

We show here I_2 RENP spectrum results for a smaller $m_0 = 5\text{meV}$, which gives smaller differences, as given in Fig.21.

3.3. Estimation of the dynamical RENP factor based on asymptotic solution

Our numerical outputs on RENP have so far been limited to the spectral shapes, which are crucial to determine the neutrino parameters. Some comments on the ω dependence of $\eta_\omega(t)$ in the fundamental formula $\Gamma_{\gamma 2\nu}(\omega, t) = \Gamma_0 I(\omega) \eta_\omega(t)$ are now in order. Numerical simulations are necessary to compute this quantity at each photon energy ω , solving the master equation Eq. B11 \sim B18 in Appendix B for two-color trigger irradiation. The ω dependence of $\eta_\omega(t)$ thus originates from ω dependence of basic couplings $\alpha_{ab}(\omega)$ that appears in the master equation, in particular through $\gamma_- = (\alpha_{ee} - \alpha_{gg})/2\alpha_{ge}$ and α_{ge} . As seen in the formulas for these in Appendix B, both of these are smooth functions of ω . Furthermore, if the upper level $|p\rangle$ lies much above ϵ_{eg} (the energy difference between $|e\rangle$ and $|g\rangle$), these $\alpha_{ab}(\omega)$'s are nearly ω independent. In any event, one expects that variation of $\eta_\omega(t)$ in the vicinity of each threshold ω_{ij} can be neglected, and the theoretical formula of $I(\omega)$ reflects the spectral shape of experimental data in the threshold regions. This way one can extract important information of neutrino parameters directly from measured data. It is however desirable to measure the quantity $\eta_\omega(t)$ or their asymptotic value at times $\gg T_2, T_3$ for the overall fitting to the entire spectral shape. This method is described in Sec. 4.

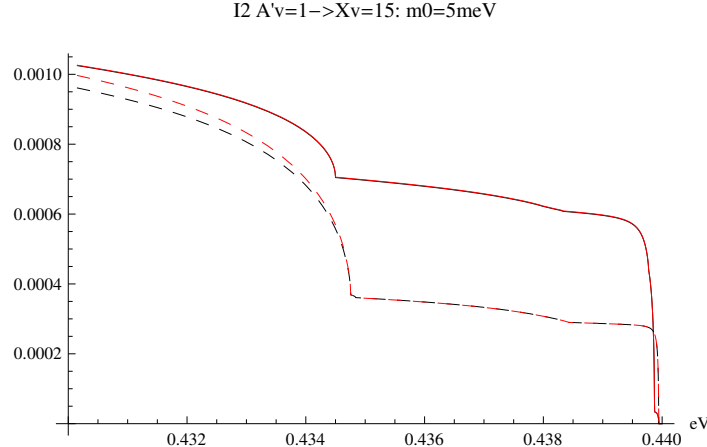


Fig. 21 I_2 RENP spectrum between $A' v=1$ and $Xv=15$. The Majorana (in colored solid for NH and in colored dashed for IH) vs Dirac (in black solid for NH and in black dashed for IH) cases are compared. A Majorana CP phase combination $(\pi/2, 0)$ (in red) is taken, with the smallest neutrino mass 5 meV. The vertical scale is in arbitrary units.

Whether one can actually perform RENP experiments with meaningful results depends on the absolute magnitude of rate Γ_0 : if it is too small, the spectral shape computation would be useless. For instance, although the Xe RENP rate Γ_0 is of order $1 \text{ Hz} (n/10^{22} \text{ cm}^{-3})^3 (V/10^2 \text{ cm}^3)$, the dynamical factor $\eta_\omega(t)$ might give a further large suppression.

Due to the complexity of our non-linear system our simulations so far are limited to the explosive cases and the linear regime, mainly for pH_2 . We feel that the late time evolution in the intermediate output regime (case of large $M1 \times E1$ coupling) is very important for RENP, which has not been explored extensively due to technical complexity. Moreover, the RENP target choice is very limited so far: Xe and I_2 (whose absolute rate is under study[24]). The case of Xe transition involves a smaller α_{ge} (due to $M1 \times E1$ nature of RENP), but a larger $\gamma_- \sim -7300$ (the corresponding number for $\text{pH}_2 \sim 0.6$), which makes numerical simulations for $\eta_\omega(t)$ harder. Under this circumstance our conclusion on the absolute rate is premature and we shall further update the simulation. Nonetheless, it would be useful to summarize what we have done so far.

We expect that the final stage of field and target state within the medium is described by static solutions of our master equation, which gives a long time behavior and is stable beyond the largest relaxation time T_1 . These static states are solutions obtained by taking vanishing time derivatives of the master equation, Eq. B11 \sim B18 in Appendix B. We first solve Bloch vector components, both grating and spatially homogeneous modes, in terms of fields. These are inserted into the field equations to search for static solutions by solving the coupled system of ordinary differential equations.

Results of spatial profiles of the static asymptotic solutions are illustrated in Fig.22 and Fig.23 in dimensionless units. The master equation for the single color mode, Eq. 34 \sim 40, has been used for simplicity. Due to the choice of a small τ_3 this solution resembles the soliton solution given in [14], but it gives a relatively large η_ω (defined by Eq. 67 \sim 69), too. This

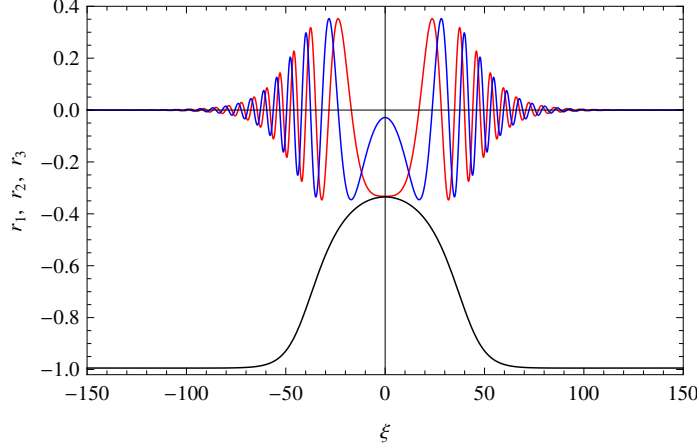


Fig. 22 Example of an asymptotic solution for the input parameters $\gamma_{\pm} = 1, \tau_1 = 200, \tau_2 = 100, \tau_3 = 0.001$. The red, blue and black curves show $r_1^{(0)}, r_2^{(0)}$ and $r_3^{(0)}$, respectively.

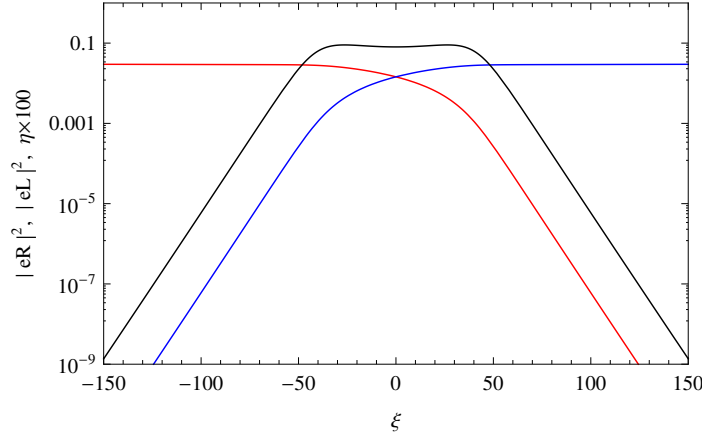


Fig. 23 Field intensity and the dynamical factor η_{ω} for the same parameter as in Fig.22. The red (blue) curve shows e_R^2 (e_L^2), and the black line is $\eta_{\omega} \times 100$.

asymptotic case gives a time independent dynamical factor; $\eta_{\omega}(t) = \eta_{\omega}(\text{constant})$. Whether a large η_{ω} factor is realized or not in actual experimental situation needs further study, both from theoretical and experimental sides. Moreover, it should be clarified how the time-evolving dynamical factor $\eta_{\omega}(t)$ approaches the asymptotic constant η_{ω} . Also, relevance of the field condensate making up the asymptotic η_{ω} value to solitons in [14] should be investigated. (The soliton is distinguished from a mere condensate by the presence of topological quantum number.)

4. Experimental aspects of PSR and RENP

4.1. Overview and strategy towards PSR/RENP experiments

4.1.1. Experimental principle of the neutrino spectroscopy with atoms. We begin this Section by reviewing the experimental principle of our neutrino spectroscopy. First of all, we prepare a collection of excited state of atoms or molecules. We then observe photon spectrum in a radiative emission of neutrino pair (RENP) process denoted by

$$|e\rangle \rightarrow |g\rangle + \gamma + \nu_i + \nu_j, \quad (75)$$

where ν_i 's are neutrino mass eigenstates. Rich physics information exists in the photon spectrum, especially near the threshold regions given by

$$\omega_{ij} = \frac{\epsilon_{eg}}{2} - \frac{(m_i + m_j)^2}{2\epsilon_{eg}}, \quad (76)$$

where ϵ_{eg} is the energy difference between $|e\rangle$ and $|g\rangle$, and $m_{i(j)}$ denotes the neutrino masses. The physics observables include

- neutrino absolute mass scale,
- mass hierarchy pattern, normal or inverted,
- mass type, Dirac or Majorana,
- CP violating phases, α and $\beta - \delta$,

among others. Detailed discussion of the physics objectives can be found in Sec. 3.

A key notion in our experimental principle is the macro-coherent amplification mechanism. In a word, the amplification is based on their collective de-excitation among all of the coherent atoms. It enhances not only the rate of the de-excitation process but also guarantees a “momentum conservation law” among the emitted particles (photon and two neutrinos in the case of RENP). The physics information can be extracted from the photon spectrum with the help of this momentum conservation law. Since we crucially rely upon this macro-coherent amplification mechanism, we plan to prove its validity by a separate experiment. We discuss this proof-of-principle experiment in more detail below. The readers are referred to Sec. 2 for detailed discussion on the theory of the macro-coherent amplification.

Another important feature in our experiment is use of the trigger laser. It initiates coherent de-excitation process, and in effect selects the portion of the photon spectrum we like to investigate. In this sense, our neutrino spectroscopy uses a “narrow-band spectrometer”. We note that energy resolution of the spectrometer is determined by the laser line width, which can be much less than a few hundred MHz, or $\sim 1\text{ }\mu\text{eV}$. Detector energy resolution is not critically needed for spectroscopic information, but it helps to reject background signals. The role of the trigger laser goes beyond the initiation of coherent de-excitation process; it helps developing condensate formation, another key notion in the RENP neutrino spectroscopy. The condensate, a system of coherent atoms and fields, is an ideal target state for RENP process.

As discussed in Sec. 3 in detail, the final RENP rate $\Gamma_{\gamma 2\nu}$ is given by

$$\Gamma_{\gamma 2\nu}(\omega, t) = \Gamma_0 I(\omega) \eta_\omega(t) \quad (77)$$

where Γ_0 is the overall constant rate and $I(\omega)$ is the spectrum function containing physics information. The third factor η_ω , termed as the dynamical RENP factor, is proportional to

the squared product of the field E^- and the medium's coherence $(R_1 - iR_2)/2$, averaged over along the target. In order to extract $I(\omega)$, we need to divide experimentally observed rate $\Gamma_{\gamma 2\nu}$ by Γ_0 and η_ω . The constant Γ_0 can be calculated accurately while the RENP factor η_ω may be obtained by detailed simulations. It is, however, highly desirable to measure η_ω more directly. We plan to determine it experimentally by measuring the coherence and population difference (r_3) of the target medium as well as the field intensities at both ends. With aid of the master equations, η_ω can be determined from those quantities determined above. One method of measuring coherence (r_1, r_2) for the case of Xe atoms is described in Sec. 4.3.

We detect single photon emission by an appropriate photon detector. The detector may be UV to IR photo sensors, depending upon the value of initial energy gap between metastable and ground states, but most likely we must use IR sensors to investigate the detailed nature of neutrinos such as Majorana-Dirac distinction and CP phases. We expect the photon emission direction to be along the trigger laser direction because macro-coherence mechanism preferentially develops the process with this mode. Thus detector solid angle coverage need not be large.

4.1.2. Paired Super-Radiance. Exploitation of the macro-coherent amplification mechanism is an essential feature in our neutrino spectroscopy. Since this is a new phenomenon not discussed in the past literature, we should first prove and study it in detail experimentally. We like to do it with a QED process called paired super-radiance (PSR), a process which emits two photons in the decay from an excited state to the ground state ($|e\rangle \rightarrow |g\rangle + \gamma\gamma$). If the macro-coherent amplification is in operation, a collection of atoms emit coherently a pair of photons with the same energies. In particular, direction of the two photons is opposite (back-to-back) when the medium's initial macroscopic polarization (coherence) is spatially-homogeneous. Thus observation of such radiations in a similar fashion to SR is an unambiguous proof of the principle. There are several advantages of proving the new principle with PSR. The most important is its rate: it is expected to be much larger than RENP since it is a QED interaction. Characteristic features of the radiation, back-to-back with equal energies, make experimental distinction easy from other possible backgrounds. The conditions and natures of PSR, mainly explosive PSR, are already shown in Sec. 2. We summarize them here briefly, adding some more studies concerning to non-explosive events. As shown in Sec. 2, explosive PSR events have the following characteristics:

- Major part of energy stored initially in medium is released as two photons in an extremely short period of time compared with medium's natural lifetime.
- There exists certain threshold conditions above which explosive events take place.
- The threshold conditions are governed predominantly by target density and length, initial coherence and de-phasing time, *etc.*
- Left-right symmetric (back-to-back) events occur when initial coherence is spatially-homogeneous (*i.e.* $r_1^{(0)}$ or $r_2^{(0)} \simeq 1$) and trigger laser is injected from both ends.
- Asymmetry between left and right flux grows as a larger initial value is assumed for the spatially-inhomogeneous coherence.

It is of great importance, from both theoretical and experimental view points, to study what is expected if some of the threshold conditions are not fulfilled. Below we show some results obtained by numerical studies performed with these motivations. The process of interest is

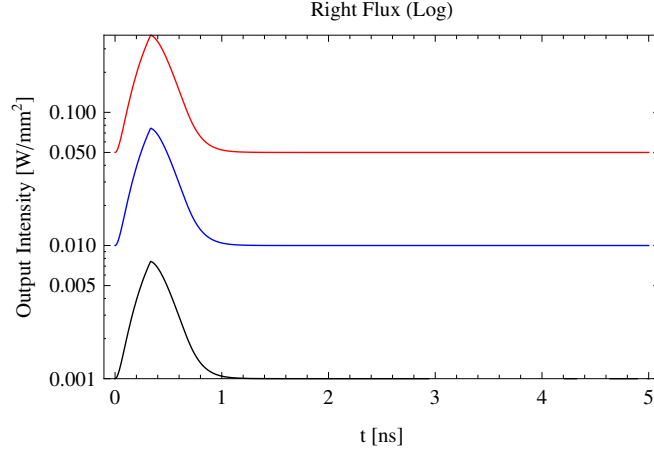


Fig. 24 Right-moving output flux from pH₂ vibrational excitation level ($Xv = 1$). The initial coherence is assumed to be spatially homogeneous ($r_1^{(0)} = 1$). The black, blue and red lines correspond to trigger laser intensities of 1 mW/mm^2 , 10 mW/mm^2 , and 50 mW/mm^2 . Note logarithmic scale for the vertical axis. Left flux is identical to the right flux.

the same process treated in Sec. 2; de-excitation process of para hydrogen molecules from a vibrationally-excited state ($Xv = 1$) to the ground state ($Xv = 0$). Figure 24 shows right-moving output flux. The three different curves in black, blue and red, correspond to three different input trigger laser intensities of 1 mW/mm^2 , 10 mW/mm^2 , and 50 mW/mm^2 . Other important parameters are

$$n = 8 \times 10^{20} \text{ [cm}^{-3}\text{]}, \quad L = 10 \text{ [cm]}, \quad r_1^{(0)} = 1, \quad T_2 = T_3 = 0.2 \text{ [ns]} \quad (78)$$

where $r_1^{(0)}$ means initial coherence of spatial homogeneous mode, with all other coherence set to zero. The important fact to these results is the values of T_2 and T_3 ; here a factor 50 smaller value is assumed than the typical values employed in Sec. 2. As shown in Fig.24, events are found to have much simpler time structure compared with explosive events shown in Sec. 2. Also their peak heights are much smaller and proportional to the input trigger intensity. Although these events appear less dramatic, if observed, they bear great significance because the two-photon process, which has the natural life time of $\sim 10^{16} \text{ sec}$, is seen in a time period of nsec.

Initial coherence of spatial grating modes, $r_{1,2}^{\pm}$, affects substantially partition between left and right output flux, as already pointed out in Sec. 2. Figure 25 shows an output flux when the initial coherence is set to

$$r_1^{(0)} = 0.1, \quad r_1^{(+)} = 0.9, \quad (79)$$

with all other parameters left same as in Fig.24. In this case, the right output flux is much smaller than the left. The fact remains true that the output flux is proportional to the input laser intensity.

The requirements for the PSR target, different from those for RENP in certain aspects, can be summarized as follows.

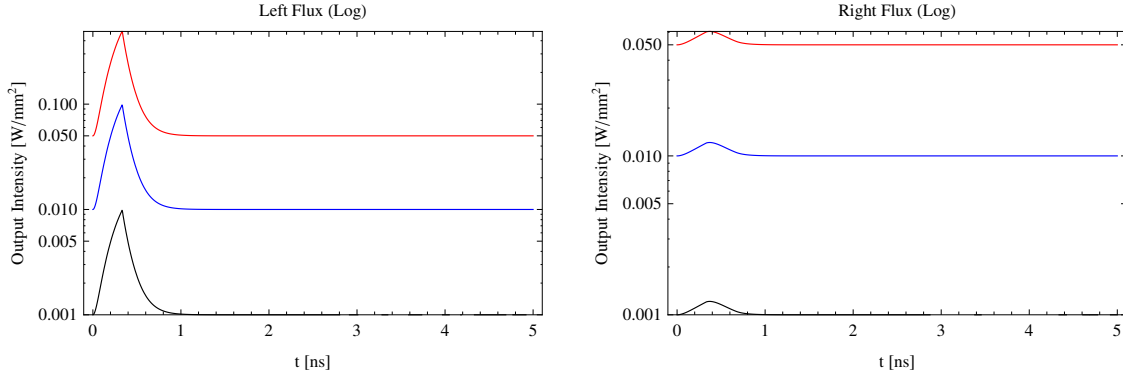


Fig. 25 Left and right moving output flux from pH₂ vibrational excitation level ($Xv = 1$). The initial coherence assumed is $r_1^{(0)} = 0.1$ and $r_1^{(+)} = 0.9$. The black, blue and red lines correspond to trigger laser intensities of 1 mW/mm², 10 mW/mm², and 50 mW/mm². Note logarithmic scale for the vertical axis.

- The initial state must be metastable (E1 forbidden), and must have at least one intermediate state of higher energy connecting between initial and final (ground) states via E1 \times E1 allowed transitions.
- Both longitudinal (T_1) and transverse (T_2, T_3) relaxation times must be longer than the PSR characteristic time scale, the time required to develop collective and coherent de-excitation process.
- The initial atomic state must be prepared to have large coherence.
- The atomic density in the initial state must exceed a certain threshold value.

At present we plan to realize a PSR experiment with para-hydrogen (pH₂) molecules, and details of the experiment will be described in the subsequent section. We would like to end this topic by emphasizing two characteristic features of the PSR experiment. First, it is a type of an experiment in which one tries to realize required experimental parameters or conditions. This is because, due to its highly non-linear nature, PSR event has a clear threshold above which signal can be observed without fail. This is in contrast to an experiment in which events occur proportional to elapse time. Second, the role of trigger laser is important as in the case of RENP. As stated already, the trigger laser initiates collective and coherent de-excitation process. Without the trigger laser, PSR events would not be initiated; this is in sharp contrast to the Dicke type super-radiance, in which quantum fluctuation can actually start coherent de-excitation process.

4.1.3. Experimental strategy toward neutrino spectroscopy with atoms . There are two crucial features in realizing the neutrino spectroscopy with atoms/molecules. One is the experimental proof of the macro-coherent amplification mechanism, and the other is formation of the stable condensate; both are related to the dynamical RENP factor $\eta_\omega(t)$. Thus our strategy is to establish macro-coherent amplification mechanism by PSR first. As was stated already, we plan to realize PSR experiments with vibrational levels of pH₂ molecules. The current status of PSR experiment with pH₂ is described in detail in Sec. 4.2.

Studies on condensate formation are one of the crucial step after establishing the PSR process. The points of condensate studies are

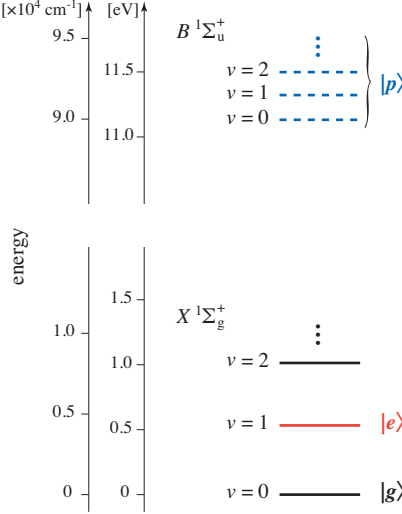


Fig. 26 Energy levels of pH₂ relevant to the PSR experiment.

- condensate formation method
- time development of stored energy and coherence
- experimental stability against PSR.

These studies will be performed with Xe atom and other heavy atoms/molecules. Simultaneously with this condensate study, target selection studies for the neutrino spectroscopy will be pursued. The requirements for the target are qualitatively the same as in the case of PSR except that the intermediate state(s) must connect the initial and final states via E1 and M1 transitions. In addition, the initial and final energy difference has profound impact on the neutrino spectroscopy since important physics objectives such as Dirac-Majorana distinction and/or CP violating phase determination can only be achieved with energy difference comparable to the neutrino mass scale (< 0.5 eV). Experimental studies on those new challenging subjects are described in Sec. 4.3. Results of the some preliminary studies using other methods are presented in Appendix E.

4.2. PSR experiment with para-hydrogen molecule

In this Section we describe PSR experiment with pH₂ in detail. The diagram of the pH₂ energy levels relevant to this experiment is shown in Fig. 26. The two-photon process from the vibrationally excited state ($Xv = 1$) to the ground state ($Xv = 0$) is measured. We note vibrational transitions of the E1 type is strictly forbidden in homo-nuclear diatomic system. Figure 27 shows a schematic diagram of the experimental setup. It mainly consists of three parts: (a) the target, (b) the excitation laser system, and (c) the trigger laser system. The target is LN₂-temperature pH₂ gas contained in a cell. The initial $v = 1$ state is prepared by the excitation laser system. The system consists of two color pulse lasers whose wavelengths are 532 nm and 683 nm. The trigger laser is a continuous wave (CW) laser and its wavelength is 4.8 μ m. The excitation laser beams are combined with the trigger laser beam by a dichroic mirror (DCM) so that they propagate collinearly in the target. PSR outputs (left moving outputs) and excitation lasers are dispersed by a prism and separately detected with a photodiode (PD). The backward components (i.e. right moving outputs) pass through the Faraday

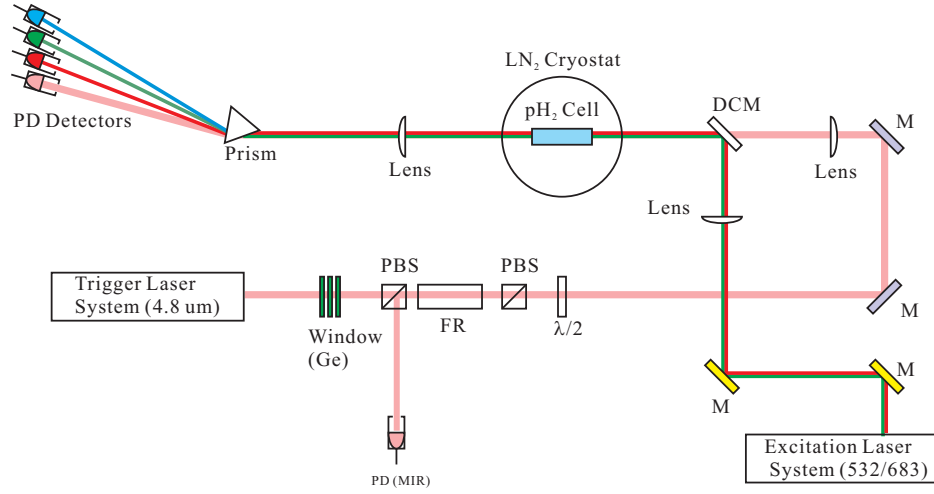


Fig. 27 Schematic diagram of the PSR experiment with pH₂. FR: Faraday rotator, $\lambda/2$: half-wave plate, PD: photo-diode, M: mirror, DCM: dichroic mirrors, PBS: polarizing beam splitter.

rotator and are reflected by the polarizing beam splitter; then they are detected by another PD. In the following, details of the target and laser systems are described.

4.2.1. Gas and solid para-hydrogen target. Preparation of target, namely selection of atom/molecule species, choice of transition levels, preparation of initial conditions *etc.*, is decisive factor for successful PSR experiments. From the point of view of atom/molecule selection, important parameters to be considered are:

- Number density of atoms/molecules
- Target length
- Damage threshold (the maximum laser intensity which a medium can receive without damage)
- Relaxation time (T_1 , T_2).

Particularly important are the number of excited atoms/molecules and coherence of $|e\rangle$ and $|g\rangle$. Both are determined by the number density of ground state atoms/molecules, target length and the excitation laser power. A higher density, a longer target and a higher damage threshold provide better conditions. However, the high-density and long-coherence are contradictory, because frequent interaction in high-density samples makes the coherent time short; thus compromise is essential for this purpose.

For PSR, relevant transition between two levels should be E1 forbidden and E1 \times E1 allowed to have a large two-photon transition moment. Vibrational transitions of homonuclear diatomic molecules fulfill these conditions. Numerical simulation in Sec. 2 and Sec. 4.1 suggests that vibrational transition of para-hydrogen (pH₂) with a large initial coherence is one of the ideal target for PSR experiments. Below properties of both gaseous and solid pH₂ are described and compared. Atoms or molecules trapped in solids (pH₂ for example) are also interesting targets for PSR/RENP; experimental studies in this direction are presented in Appendix E.

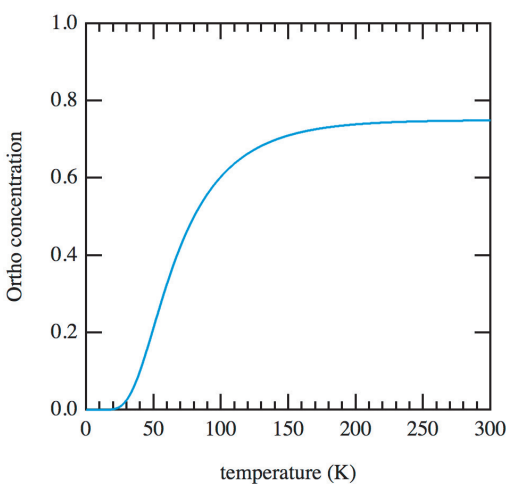


Fig. 28 Ortho-para ratio (o/p) of thermally equilibrium hydrogen at 0 to 300 K. The o/p can be controlled from almost zero to 0.75 by magnetic catalysts kept at corresponding temperature.

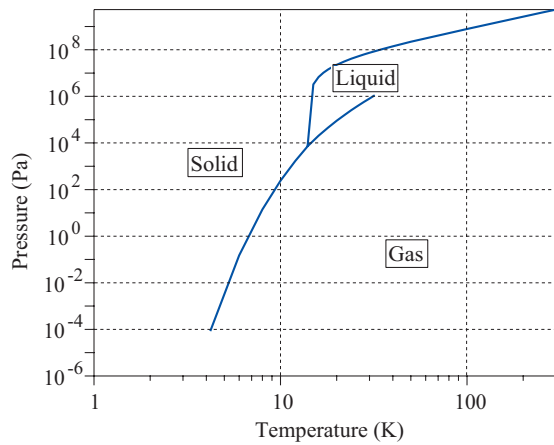


Fig. 29 Phase diagram of eH₂.[26] Temperature and pressure at the triple point of eH₂ is about 13.8 K and 7000 Pa, respectively. Structure of solid pH₂ is h.c.p. at low temperature, low o/p.

Properties of molecular hydrogen. The molecular hydrogen, the simplest diatomic molecules, has attracted great interest in various fields, both theoretical and experimental. Physical properties of the molecular hydrogen are well summarized in P. Clark Souers' book.[26] The nuclear spin isomers of hydrogen molecules show different nature. The nuclear spin of proton ($I = 1/2$) causes two spin states of molecular hydrogen, para ($I = 0$) and ortho ($I = 1$). The nuclear spin wavefunction of pH₂ is anti-symmetric under the exchange of two identical protons while that of ortho-hydrogen (oH₂) is symmetric. Therefore, the rotational quantum number J of pH₂ and oH₂ should be even and odd in the vibronic ground state, respectively, because overall wavefunction should be anti-symmetric under the exchange of nuclei. Conversion between these two states is very slow without external magnetic fields so that it is possible to treat them as different molecules. On the other hand, ortho-para ratio (o/p) easily reaches thermal equilibrium with a magnetic catalyst. The o/p ratio of thermally equilibrium hydrogen (denoted by eH₂) at room temperature is 3:1 and it converges to zero at the limit of 0 K (Fig. 28) and can be controlled from almost zero to 0.75 by passing gaseous or liquid hydrogen into magnetic catalysts kept at corresponding temperature. It is worth noting that even at the triple point (13.8 K) o/p $\sim 10^{-5}$, which is the lower limit by this method.

The phase diagram of eH₂ is shown in Fig.29. The temperature and pressure at the triple point of eH₂ is about 13.8 K and 7000 Pa, respectively. The low melting point allows us to use gaseous sample at wide temperature ranges while solid sample should be kept around liquid Helium temperature. Structure of solid pH₂ is known to be hexagonal closed packing (h.c.p.) at low temperature and low o/p. Spectroscopic data of molecular hydrogen are also well known. The light mass makes the rotational constants and vibrational frequency

fairly large. Energy splitting between $J = 0$ and $J = 2$ (pH_2) and $J = 1$ and $J = 3$ (oH_2) in the vibronic ground states is 354.38 cm^{-1} (510 K) and 587.06 cm^{-1} (845 K). This large energy separation strongly suppresses the population of rotationally excited states in thermal equilibrium at low temperatures. Even at 77 K, the Boltzman factor of the $J = 2$ state is less than 10^{-2} . The vibrational frequency is 4401.2 cm^{-1} . The first electronic excited state lies at 91700 cm^{-1} above the ground state and can be treated as a far-resonant state in our experimental scheme. Rovibronic energy states are not largely changed in solid pH_2 because of weak inter-molecular interaction. Hydrogen is homo-nuclear diatomic molecule with no permanent electric dipole moment so that both pure rotational transition and rovibrational transition are dipole-forbidden although weak electric quadrupole transition between $v = 1$ and $v = 0$ was observed with long optical path. [27] On the other hand, Raman transition is allowed and has been studied extensively, especially vibrational Raman transition. Because of the large vibrational energy, molecular hydrogen is often used as a medium of a Raman shifter. Both solid and gaseous hydrogen have been investigated as coherent Raman media by adiabatic manipulations. [28] [29] [30] [31] These approaches are suggestive because coherence of system is constitutive for PSR.

Gaseous hydrogen. The coherence time of vibrational states of gaseous hydrogen can be estimated from the linewidth of vibrational Raman transitions. The linewidth depends on the number density (pressure) and temperature. Hereafter, the relation of number density and coherent time is discussed.

In general, linewidth of gaseous sample is determined by

- Natural lifetime
- Doppler broadening
- Collisions (Pressure broadening)
- Power broadening
- Transit-time broadening.

The power broadening and transit-time broadening is not intrinsic linewidth of sample. It is to be noted that the type and nature of decoherence (homogeneous or inhomogeneous) are not distinguished here and only total coherence time is discussed. The parameter T_1 describes the lifetime due to the spontaneous emission and represented by the Einstein's A coefficient of samples. In the case of molecular hydrogen gas, its rovibrational transition is dipole-forbidden. It means that the lifetime of rovibrational excited states is substantially long. Actually, lifetime due to the quadrupole transition of the $v = 1$ state is in the order of 10^6 sec. [27] Natural lifetime broadening can be neglected in what follows.

Doppler broadening, which is attributed to inhomogeneous Doppler effect caused by Maxwell-Boltzman distribution of molecular velocity, is dominant in low pressure gases. Neglecting a small relativistic correction, the full width at half maximum (FWHM) of Doppler broadening is given by

$$\Delta\nu_D = \nu_0 \sqrt{\frac{2kT \log(2)}{mc^2}} \quad (80)$$

where ν_0 , T , m and c is the transition frequency, temperature, mass of molecules and the velocity of light, respectively.

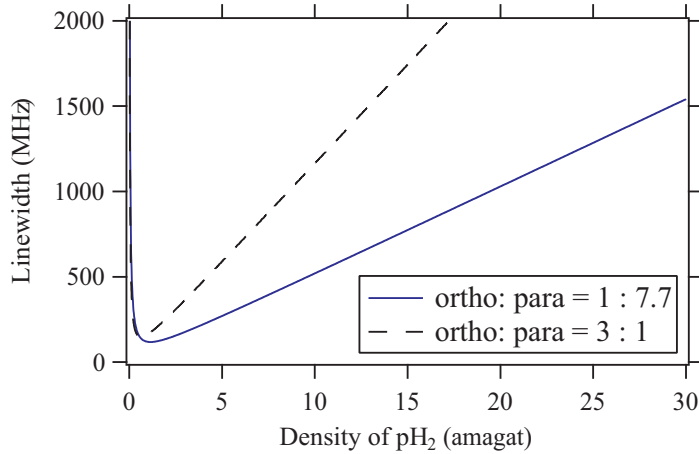


Fig. 30 Linewidth of $Q_1(0)$ Raman transition of gaseous pH_2 at 81 K with ortho-para ratio of 1:7.7 and 3:1 as a function of density of pH_2 .

Collisional broadening, also called as pressure broadening, is dominant in high pressure gas. Detailed analysis of their lineshape is difficult because complicated inter-molecular interactions should be considered. [32] However, its lineshape is approximately Lorentzian and its FWHM is proportional to the pressure. Pressure-broadening coefficients are species-dependent values and typically 10 MHz per Torr.

In the case of rovibrational transitions of molecular hydrogen gas, the pressure and temperature dependence of Raman linewidth is well studied. Bischel and Dyer [33] reported experimental linewidth and fitting coefficients using phenomenological equation as

$$\Delta\nu_{hydrogen} = \frac{A}{\rho} + B \times \rho \quad (81)$$

where ρ is the total number density of pH_2 and oH_2 in amagat ($1 \text{ amagat} = 2.69 \times 10^{19} \text{ cm}^{-3}$) and A, B is fitting coefficients. (Table 3). The second term corresponds to pressure broadening. The first term represent effect of Doppler broadening and "Dicke-narrowing". The Dicke-narrowing appears between the Doppler dominant region and the collision dominant region. This narrowing is due to a smaller Doppler shift caused by frequent velocity-changing collisions. Fig. 30 shows linewidth of the $Q_1(0)$ Raman transition at 81 K and ortho:para = 1:7.7 and 3:1 as a function of density of pH_2 . The minimum linewidth of the o/p = 1:7.7 sample at 81 K is 117.4 MHz (corresponds to 2.7 ns) at 1.15 amagat ($= 3.09 \times 10^{19} \text{ cm}^{-3}$). It is easy to prepare $\sim 10^{21} \text{ cm}^{-3}$ pH_2 gas. However, T_2 is in the order of 0.1 ns at such high pressure.

Damage threshold by laser field of gaseous hydrogen depends on frequency of the applied field and is probably determined by non-resonant multi-photon ionization in most of our frequency region. Recent ultrafast experiments reported multi-photon ionization of hydrogen molecules by visible light is dominant at $> \sim \text{TW cm}^{-2}$. [34] It is easy to elongate the sample cell of gaseous hydrogen to 1 m or more and possible to achieve longer pass length by using a multi-pass cell or a cavity.

Table 3 Linewidth coefficients of Raman $Q_1(0)$ transition of gaseous pH₂.[33]

T(K)	ortho:para	A (MHz amagat)	B (MHz /amagat)
81	3:1	189 ± 40	29.0 ± 1.0
81	1:7.7	76 ± 6	45.4 ± 0.8
298	3:1	257 ± 12	76.6 ± 0.8

Table 4 Typical properties of gaseous and solid pH₂ Parameters of gas is at the minimum linewidth condition at 81 K. Parameters of the solid is at around 4 K.

	gas	solid
Density (cm ⁻³)	$10^{19} \sim 10^{21}$	2.6×10^{22}
T_1 (s)	10^6	4×10^{-5}
T_2 (ns)	$3 \sim 0.1$	~ 10
Damage threshold (W cm ⁻²)	$\sim 10^{12}$	$\sim 10^8$
Target length (m)	$0.1 \sim 1$	≤ 0.1

Solid hydrogen. Solid pH₂ is an attractive target from the point of coherent experiments because it fulfills high density and long coherence simultaneously. The number density of saturated solid pH₂ is about 2.6×10^{22} cm⁻³ at 4 K, which corresponds to that of gaseous sample at 1000 atm, 300 K. Due to weak interaction, not only vibrational motion but also rotational motion of hydrogen are quantized and coherence time is much longer than classical solids. The long coherence time of the excited vibrational state is estimated to be on the order of 10 ns from linewidth of stimulated Raman spectroscopy. [35] The time-resolved coherent anti-Stokes Raman spectroscopy (TRCARS) also supported this value. Introduction of the TRCARS experiment and discussion of the long T_2 of solid pH₂ are in Appendix D. Long T_1 (not radiative) of the $v = 1$ state in solid pH₂ was also reported to be $\sim 40 \mu\text{s}$ at 4.8 K.[36]

However, damage threshold of solid pH₂ was reported to be 180 MW cm⁻², which is fourth order smaller than that of gaseous sample. [30] Furthermore, it may be troublesome to prepare longer solid pH₂ than 10 cm with optically transparent quality. Application of multi-pass or cavity is also difficult because of scattering in the solid.

Comparison between pH₂ gas and solid targets. Table 4 lists a set of parameters and their typical values relevant to the PSR experiment, comparing between gaseous and solid pH₂. As seen, the solid phase is better from the view points of the number density and de-phasing time T_2 . Demerit of using solid phase is its low damage threshold. It limits attainable number density and initial coherence low; actually too low to observe PSR events with our current technique. On the other hand, the numerical simulation of Sec. 4.1 shows that the linear regime PSR may well be observed with gas phase pH₂. We have thus chosen gas phase pH₂ aiming at the first observation of PSR events. It should be noted however that solid pH₂ is much more attractive once the damage threshold limitation is overcome. Some development efforts along this line are described below and Appendix D.



Fig. 31 The cryostat for gas experiments (Infrared Laboratories, ltd. HDL-8). Both liquid N₂ (77 K) and He (4.2 K) can be used as cryogenic liquids. Temperature of a cold stage can be controlled by a heater with a PID circuit. There are two view ports with IR windows for optical experiments.

Experimental techniques. In solid pH₂, the coherence time depends largely on the oH₂ concentration. The linewidth of vibrational Raman transition to the $v = 1$ state is about 10 MHz at o/p of 2000 ppm while this becomes 60 MHz at 20000 ppm.[35] Then, a highly purified pH₂ is desired. Purity of pH₂ is also important in gaseous pH₂ because FWHM of gaseous hydrogen at the same pH₂ density is probably smaller for the pure pH₂ sample as seen in Fig. 30, although there is no precise data at various ortho-para ratios. Almost pure pH₂ can be obtained by passing hydrogen gas into magnetic catalysts such as FeO(OH) kept at about 14 K. The o/p ratio of prepared samples can be estimated in several ways. By measuring IR absorption spectra of solid hydrogen, the o/p ratio is determined by intensity of oH₂ induced pH₂ vibrational transition, which can be observed in solid phase. A typical value of ortho-para ratio in our laboratory is about 500 ppm.

For gaseous experiments, a sample cell was attached to a cold stage of a cryostat (Fig. 31). The temperature of cell was measured by Si diodes and controlled by a heater with a PID circuit. The cell was made of oxygen-free copper and both sides were sealed by IR windows with indium gaskets for an optical path. We usually use BaF₂ windows for both cell and cryostat because of its excellent IR transmittance. The optical path is 7.5 cm in length and 2 cm in diameter (Fig. 32). Sample gas was installed via stainless tubing connected to cell with silver soldering. Pressure capacity of the cell is around 500 kPa. For higher pressure experiments, it is better to use small diameter cell and CaF₂ or Sapphire windows. For example, pressure capacity of a cell with 4 mm diameter and windows of 2 mm thickness is 8 MPa (CaF₂ windows) or 40 MPa (Sapphire windows).

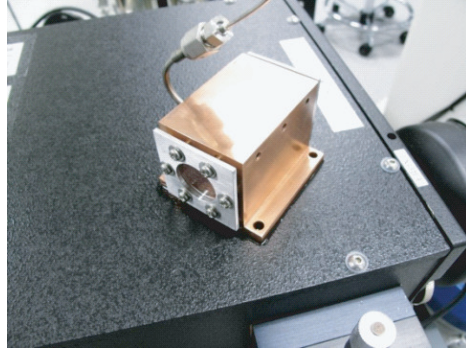


Fig. 32 The home-made gas cell of 7.5 cm length and 2 cm diameter applicable to ~ 1 K and ~ 500 kPa. The cell was made of oxygen-free copper and both sides were sealed by IR windows with indium gaskets for an optical path. Sample gas was installed via stainless tubing connected to cell with silver soldering.

For solid experiments, a vacuum chamber with a liquid Helium bath or a closed cycle refrigerator (cooling power should be larger than 1.0 W at 4 K) are used. The optical grade crystal is prepared typically by the closed cell method. This method was originally developed by Oka et al.[37] The prepared almost pure pH₂ gas is introduced through a thin stainless steel tube into a copper cell cooled by a cryostat. The cell is similar to that shown in Fig. 32. The inlet gas flow rate is controlled to keep the cell temperature at about 8 K. The solid pH₂ grows radially inward from the cell wall and forms a polycrystalline aggregate of h.c.p. crystals having their c axes normal to the wall of the cell. The sample thus grown is transparent. The crystals prepared by this method sometimes suffer from the cracking especially during the cooling cycle after the crystal growth and the inhomogeneity due to the polycrystalline structure.

To prepare higher quality crystals, pressurized liquid method was developed by Hakuta et al.[38] Crystals in the closed cell method are obtained by direct condensation from gaseous hydrogen. In contrast, this method produces crystals from the pressurized liquid phase by which crack free single crystal can be obtained. Solid pH₂ on the melting curve about 15 K has a similar molar volume as the solid at ~ 4 K under the saturated vapor pressure. Thus, a homogeneous crystal is grown at about 15 K by pressurizing the liquid-phase first, and then the transparent crystal is cooled down to the experimental temperature. The obtained pH₂ crystal is transparent and uncracked and have a higher damage threshold for laser irradiation.

4.2.2. Laser system for coherence preparation and trigger. In this section, we explain laser systems for the PSR experiment using para-H₂ vibrational states. We explain the excitation laser system first, and the trigger laser system is described later. Since we employ a nonlinear optical frequency-conversion technique for the laser systems, we also explain this technique briefly. For detail, the reader is referred to a standard textbook such as Ref. [39] or Ref. [40].

As described in Sec. 4.1, it is important to prepare a large atomic (or molecular) coherence in the ground state $|g\rangle$ and the excited state $|e\rangle$ for the experiment. To prepare a large coherence, we manipulate the stimulated Raman process adiabatically as depicted in Fig.

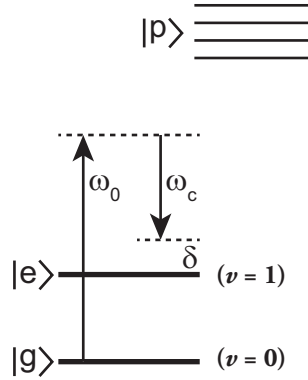


Fig. 33 Energy level diagram to prepare coherence ρ_{eg} in an atomic or molecular system. Two color driving laser fields at frequencies of ω_0 and ω_c are applied. A small detuning of δ is negative in this diagram. When the detuning δ is appropriate and the intensity of driving lasers is sufficiently large, the magnitude of the coherence of this transition becomes its maximum value.

33. For adiabatic manipulation, we apply two-color strong driving lasers whose frequencies are slightly detuned from the two-photon resonance of a selected Raman transition. When the detuning δ is appropriate and the intensity of driving lasers is sufficiently large, the magnitude of the coherence of this transition becomes its maximum value $|\rho_{eg}| = 0.5$.

In the experiment, high power and narrow-linewidth lasers are required. The time duration of incident laser on the order of the target relaxation time (i.e. T_2) is sufficient. Thus a nanosecond pulse laser is preferred for two reasons. First, its power is sufficiently high: a peak intensity of >1 GW/cm² with a modest beam radius of 0.1 mm can easily be obtained, much higher than a continuous-wave (CW) laser. Second, the Fourier transform limited linewidth is on the order of 100 MHz, which is sufficiently narrow for the experiment. Also a good temporal overlap of these two lasers is important. Figure 34 depicts a comparison of the beam quality and wavelength coverage range of the available technologies. The choice of the most relevant technology for our experiment is a crucial issue. For one of the driving lasers, an injection-seeded Nd:YAG laser is a good choice because of its availability of high power (up to several J, peak power of hundreds MW) and narrow linewidth. The wavelength of the other driving laser is determined by the target atom or molecule. Here, we consider hydrogen molecule as a target system for the PSR experiment. When we choose the first vibrational level as the excited state $|e\rangle$ (energy of 4160 cm⁻¹) and a second harmonic of Nd:YAG laser (wavelength of 532 nm) as one of the driving laser, the wavelength of the other laser is 683 nm.

Two types of laser techniques are commercially available at this wavelength range: a dye laser and optical parametric oscillator (OPO). A dye laser may be often used, however, such liquid laser is in general unstable and its linewidth is very broad. Usually the linewidth of a dye laser is on the order of GHz: 20–30 times broader than the transform limit. Another disadvantage of the dye laser is that frequent maintenance (replacing the dye solution and re-optimization of laser cavity) is required. An OPO is solid-state system and it offers very wide tunability (205 nm to 2550 nm). However the linewidth of such OPO is much broader than that of dye laser. Typically it is about 75 GHz: 300–500 times broader than the transform

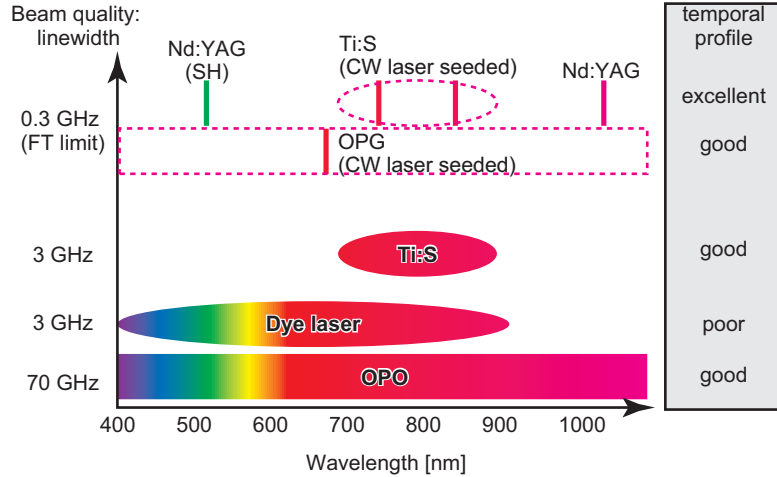


Fig. 34 Comparison of the beam quality (linewidth and temporal profile) and the spectral coverage range of available laser technique. OPO: optical parametric oscillator; OPG: optical parametric generator; Ti:S: titanium sapphire laser; Nd:YAG: neodymium-doped yttrium aluminum garnet laser. The fundamental wavelength is 1064 nm and its second harmonic (SH) is 532 nm; FT limit: Fourier-transform limit. The wavelength tuning range of dye lasers and OPOs are very wide, however, its linewidth is very broad: typically 20–500 times broader than the FT-limit. Injection seeding technique is useful to reduce linewidths of those light source.

limit. Alternatively, a titanium sapphire (Ti:S) laser may be another choice. It is a widely tunable all-solid-state laser system. In particular, injection seeded Ti:S laser offers Fourier transform limit linewidth and good beam quality. Dual-wavelength injection seeded Ti:S laser was used to produce near maximum molecular coherence [41]. In this case, however, rotational Raman transition was used. Lasing wavelength range of Ti:S laser is limited from 700 nm to 900 nm (about 3000 cm^{-1}). Thus this laser may be difficult to use for vibrational Raman process of pH_2 because the Raman transition frequency is 4160 cm^{-1} .

Whereas those light sources mentioned above are unsuitable for the experiment, injection seeded OPO or optical parametric generator (OPG) is highly suitable technique. Continuous-wave (CW) laser seeding technique is often used to generate narrow linewidth coherent light [42–51]. Injection seeding requires an external light source of modest power (from a few μW to a few mW) and good spectral properties; also the tuning bandwidth is limited by seed laser. However it offers the advantage of transform limited or nearly transform limited linewidth.

An injection seeding OPG uses the process of optical parametric amplification, which is shown in Fig. 35 (a). A strong pump wave at the frequency of ω_p and a weak signal wave at the frequency of ω_s interact in a nonlinear optical medium. As a result, an output wave at the difference frequency $\omega_i = \omega_p - \omega_s$ is generated, and the signal wave is amplified. When the nonlinear medium is placed in an optical cavity, the presence of feedback produces oscillation. In this case, the system is called OPO. Experimentally, OPGs are especially preferable for injection seeding because an OPG requires no optical cavity. Thus there is no

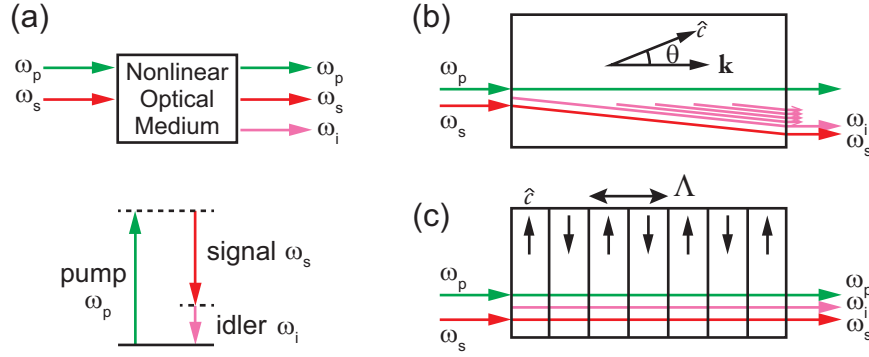


Fig. 35 (a) Schematic diagram of the injection-seeded optical parametric generation. Corresponding energy level diagram is also shown. Schematic representations of a parametric frequency conversion with (b) an angle-phase-matching homogeneous bulk crystal and (c) a periodically poled material. In (b), the polarization of the signal and the idler waves are taken as extraordinary. The generated signal and idler waves at each point in the crystal does not propagate collinearly with each other. In (c), the optical axis of the crystal alternates in orientation with period Λ (on the order of $5 \mu\text{m}$ to $10 \mu\text{m}$). This case all waves collinearly propagate the crystal.

need to actively control the cavity resonant frequency to match the frequency of the seeding laser. This makes the whole system simple.

To obtain a high conversion efficiency, a phase matching condition should be fulfilled: $\vec{k}_p = \vec{k}_s + \vec{k}_i$, where \vec{k}_j are the wave vectors corresponding to the waves with frequencies ω_j ($j = p, s, i$). The phase matching condition is interpreted as momentum conservation for the three photons participating in the nonlinear mixing process. Conventionally the condition is fulfilled in birefringent crystals that have two different refractive indices n_o and n_e for the ordinary and the extraordinary waves. The ordinary wave is polarized perpendicular to the plane containing the propagation vector \vec{k} and the optical axis. On the other hand, the extraordinary wave is polarized in the plane containing \vec{k} and the optical axis. While the ordinary refractive index n_o does not depend on the propagation direction, the extraordinary index n_e depends on the angle θ between the optical axis and \vec{k} . Therefore careful tuning of the angle (i.e. the refractive index) is required to establish the phase matching condition. A serious drawback of using angle tuning is walkoff effect, which is often observed in a birefringent crystal[52]. Whenever the angle θ is different from 0 or 90 degrees, the Poynting vector \vec{S} and the propagation vector \vec{k} are not parallel for extraordinary waves. As a result, ordinary and extraordinary waves with parallel propagation vectors quickly diverge from one another as they propagate through the crystal, as depicted in Fig. 35 (b). This walkoff effect limits the spatial overlap of the two waves and decreases the efficiency. Thus in general one cannot achieve a large single-pass parametric gain with an angle-phase-matching bulk crystal even in the perfect phase-matching condition. To overcome low conversion efficiency, many systems that have been reported in literature used optical cavity to increase the pump power and the effective interaction length. Also a pair of crystals is often used in order to compensate walkoff.

There is a relatively new technique known as quasi-phase-matching. In quasi-phase-matching, a periodically-poled material whose optical axis is inverted periodically as a function of position is used. The idea of quasi-phase-matching is schematically illustrated in Fig. 35 (c). The advantage of quasi-phase-matching is that there is no walkoff effect. Thus one can use a longer crystal than an angle phase-matching bulk crystal and therefore can get higher single-pass conversion efficiency. Since the single-pass conversion efficiency is large, an optical cavity is not necessarily required. Therefore an injection seeding OPG with a periodically poled crystal offers great simplicity of the system.

A drawback of periodically poled crystals, as compared to conventional bulk crystals, is that it is difficult to make a thick crystal with present technology. This is because a high electric field (above 20 kV/mm) must be applied to the crystal during the fabrication process of periodical inversion of crystal polarization. There is no such restriction for bulk crystals, thus fabrication of thick crystals is feasible. Since the optical parametric process uses a nonlinear effect, high conversion efficiency can be obtained with high input pump intensity. However, there is a certain damage threshold that limits maximum input intensity for all nonlinear materials. In order to keep input intensity less than the damage threshold, a thicker crystal (i.e. larger aperture crystal) is much better for high power operation.

There are various types of periodically poled crystals such as lithium niobate (LiNbO_3 , LN), lithium tantalate (LiTaO_3 , LT), and potassium titanyl phosphate (KTiOPO_4 , KTP). Among these crystals, LN has the largest nonlinear coefficient. However it also has a lower photo-induced damage resistivity. Doping of MgO improves resistivity, but its damage threshold is still not very high. The nonlinear coefficient of KTP is lower than that of LN, and the damage threshold is almost the same as that of LN. On the other hand, stoichiometric lithium tantalate (SLT) has a higher damage resistivity than LN and KTP. Although its nonlinear coefficient is about 2/3 of LN, the damage threshold is twice as large as LN [53]. Thus one can expect a higher output power by using SLT.

We employed MgO doped PPSLT crystal (Oxide Corp., Q1532-O001) for our OPG system. The thickness of PPSLT is limited to 1 mm, so we used a 8 mm wide crystal in order to reduce the input intensity. A schematic diagram and photograph of the OPG system is shown in Fig. 36 (a) and (b). The PPSLT crystal was pumped by the second harmonic of a Q-switched injection-seeded Nd:YAG laser (Litron LPY642T). The Nd:YAG laser is flash lamp pumped at repetition rate of 10 Hz with a true TEM_{00} single transverse mode ($M^2 < 1.3$) and single longitudinal mode output. Pulse energies up to 130 mJ with a pulse duration of 8 ns is available at 532 nm. The pump beam is expanded to elliptical shape ($0.68 \times 3.7 \text{ mm}^2$) by means of cylindrical lenses. For injection seeding, an extended cavity diode laser (ECDL) in the Littrow configuration was used. We used a commercially available laser diode chip (TOPTICA LD-0685-0050-3, no anti-reflection (AR) coating) for the ECDL. The output power of the ECDL is more than 10 mW with a typical mode-hop-free scanning range of 3 GHz. A polarization maintaining optical fiber was used for transverse mode cleaning. Typically, a fiber output of 2 mW was used for injection seeding. The injection seeding beam was also expanded to elliptical shape ($1 \times 8 \text{ mm}^2$). The pump and injection seeding lasers are combined with a dichroic mirror. The PPSLT crystal is 40 mm long \times 1 mm thick \times 8 mm wide (periodic domain width of 7 mm) and periodicity of 10.3 μm . Phase matching temperature at 683 nm was measured to be around 110°C. The crystal is AR coated for three wavelengths: pump (532 nm), signal (683 nm), and idler (2.4 μm). Figure 37 shows a

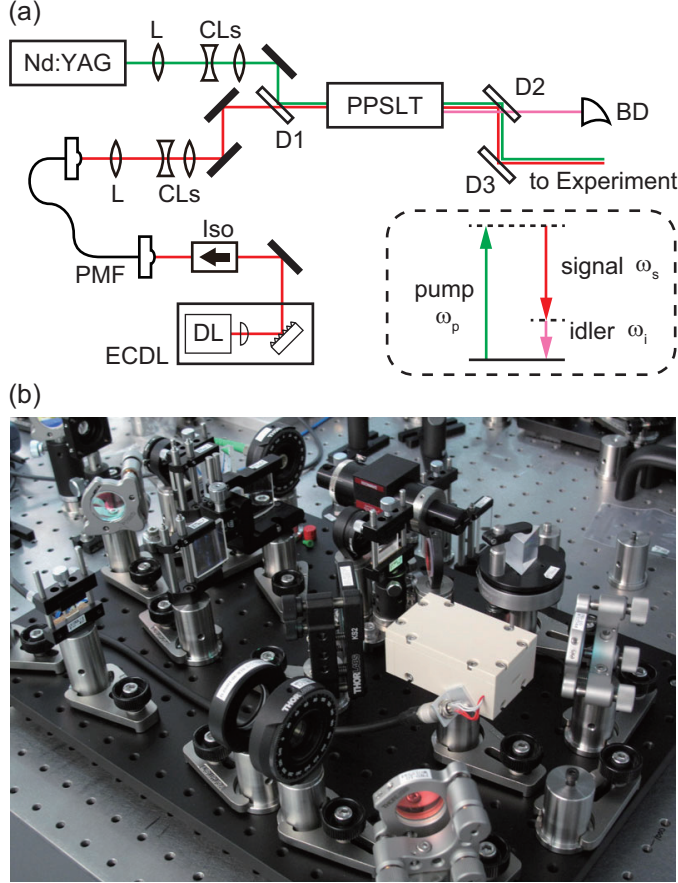


Fig. 36 (a) Schematic diagram and (b) Photograph of the excitation laser system. ECDL: extended cavity laser diode; DL: diode laser chip; Nd:YAG: pulsed Nd:YAG laser; L: spherical lens; CLs: cylindrical lenses; D1: dichroic mirror used to combine pump laser (Nd:YAG) and continuous-wave seed laser (ECDL); D2–D3: dichroic mirrors used to separate the pump plus the signal beam and the idler ($2.4 \mu\text{m}$); BD: beam dumper; Iso: isolator; PMF: polarization maintaining optical fiber; PPSLT: periodically-poled stoichiometric lithium tantalate crystal. The PPSLT crystal is pumped by the second harmonic of a Q-switched injection-seeded Nd:YAG laser, and generates signal (683 nm) and idler waves.

typical temporal profile of the transmitted pump beam and generated signal (683 nm) light. Good temporal overlap is obtained.

We next describe the trigger laser system. According to the PSR simulation (Sec. 4.1), the power of trigger laser is less important, however the narrow linewidth (<MHz) may be crucial. The wavelength of the trigger laser is $4.8 \mu\text{m}$. While there are many lasers available at visible or near-infrared (NIR) region, coherent light sources emitting mid-infrared (MIR) radiation is less common. Recently, quantum cascade lasers, which directly radiate mid-infrared wavelength light, are commercially available. However the linewidth is broad (about 45 MHz) and they are still expensive. Moreover, peripheral optical devices in the MIR spectral region such as optical isolators, gratings, high-reflectivity low-loss mirrors for high-finesse optical cavity, or a wavelength meter are also less common. Thus there are practical drawbacks when one develops laser sources with direct laser radiation devices in

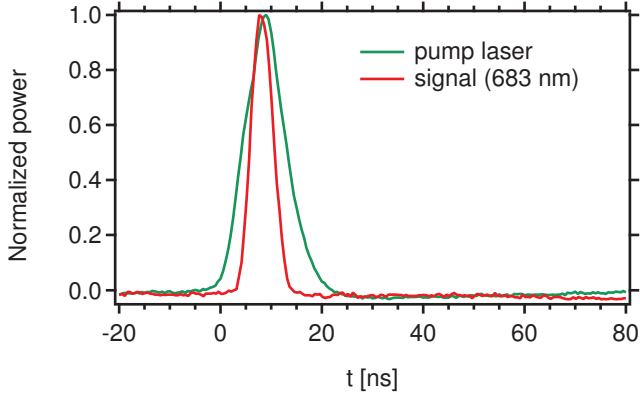


Fig. 37 Temporal profile of OPG output. Green line shows the temporal profile of the pump laser transmitted the crystal. Red line shows that of the generated signal (683 nm) light.

the MIR region. Instead, a light source based on nonlinear optical process (i.e. difference-frequency generation) with a quasi-phase-matching material pumped by NIR lasers is highly competitive. It allows to transfer the high performance characteristics of the pump laser at NIR region to the MIR: precise wavelength resolution and narrow linewidth.

Figure 38 shows the block diagram and the photograph of the trigger laser system. We employ two of master oscillator power amplifier (MOPA) systems as pump sources of DFG. The wavelength of the MIR light is determined by measuring wavelengths of both pump lasers by a wavelength meter (HighFinesse, WS6-200). One of the pump laser is combined with the other by DCM and coupled into optical fiber. We employ waveguide PP-MgO:LN crystal (NTT electronics, WD4800-000-A-B-C). A great advantage of waveguide PPLN device is that one can obtain longer interaction length with higher beam intensity, which yields two or three orders of magnitude larger single-pass frequency-conversion efficiencies than no-waveguide crystals. This is especially effective for CW laser because its beam intensity is relatively low.

4.3. Towards RENP experiment with Xe

4.3.1. RENP with Xe atoms. As described in Sec. 1, Xe atom is one of the important candidates for studying the RENP. The lowest excited state $5p^5(^2P_{3/2})6s^2[3/2]_2$ with total electron angular momentum $J = 2$ in Xe atom can decay only through M2 transition to the ground state $5p^6(^1S_0)$, and thus this $J = 2$ state is metastable with lifetime of $O(40)$ s [54]. The RENP process in Xe atom would be recognized by observing a characteristic decay spectrum of emitted photon from the metastable state, which has distinctive threshold at the photon energy of 4.16 eV, half of the energy difference between the metastable and ground states. Figure 39 shows such typical RENP spectrum, where different threshold locations ω_{ij} appear depending on mass scale of participating neutrino pair.

In order to successfully observe the RENP process, understanding and precise control of a coherent state of atoms interacting with static field condensate is inevitably important [8]. Therefore the investigation on feasibility and further research/development is needed for

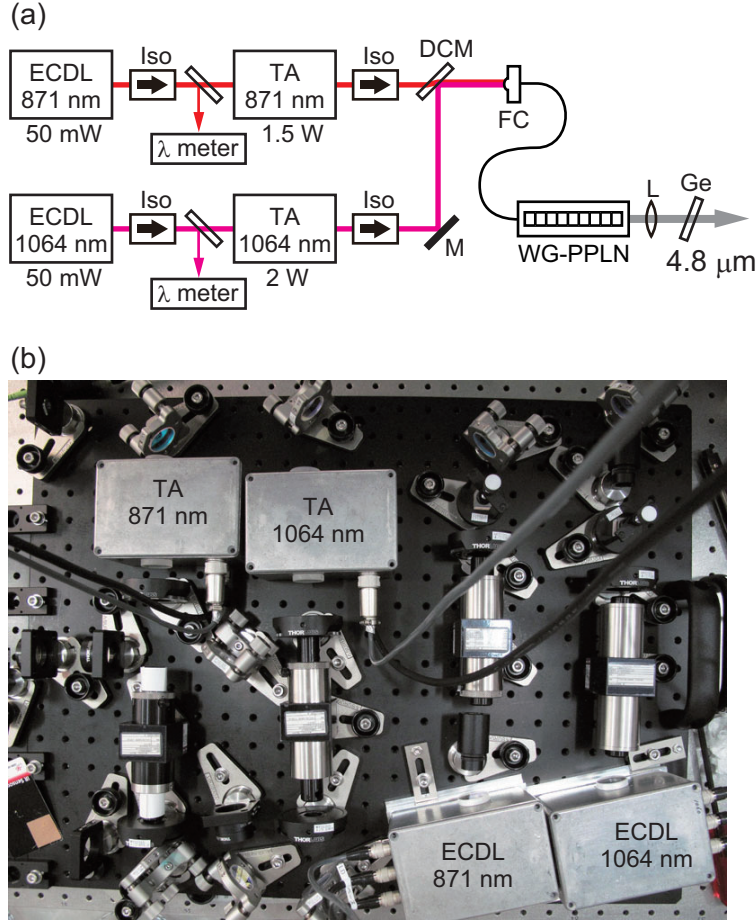


Fig. 38 Trigger laser system: (a) Block diagram of the trigger laser system. The wavelength of the trigger laser is $4.8 \mu\text{m}$. We employ difference-frequency generation (DFG) to obtain coherent light at this mid-infrared wavelength range. For pump lasers of DFG, we employ two master oscillator power amplifier (MOPA) systems at wavelength of 871 nm and 1064 nm, respectively. Both lasers are coupled into optical fiber and then coupled to the waveguide PPLN crystal. Typical output power from each device is indicated in the figure. (b) Photograph of the system. Note that MOPA systems are only shown in the photograph. ECDL: extended cavity laser diode; TA: tapered amplifier; Iso: isolator; DCM: dichroic mirror used to combine two pump lasers; FC: fiber coupler; WG-PPLN: waveguide PP-MgO:LN crystal; L: collimator lens; Ge: Germanium filter.

the preparation and confirmation of the atomic coherence between the metastable and the ground state in Xe atom. The fundamental characteristics of metastable state in Xe, numerical calculation of achievable coherence, and the prospect for experiments are described below.

4.3.2. Properties of Xe atom in gas phase. The atomic coherence between the metastable and the ground state in Xe can be produced by applying two light-fields ("pumping" and "coupling or sometime called stokes") on so-called Λ -type three-level atomic system. However, the achievable atomic coherence tends to be limited from several origins, which

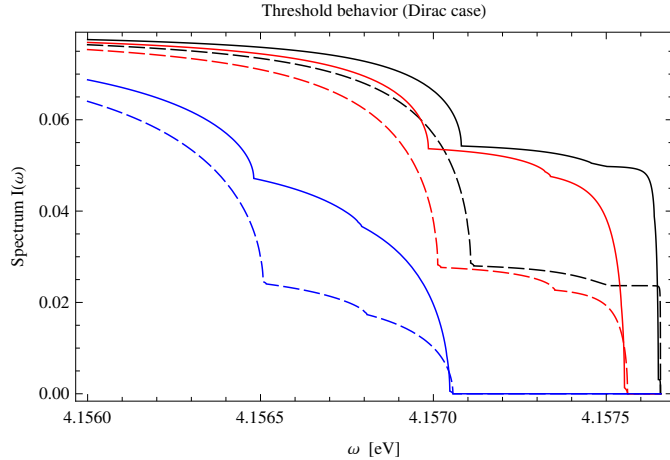


Fig. 39 Examples of Xe RENP spectra near threshold. Assumed are Dirac neutrinos with the minimum masses m_0 of 2 (black), 20 (red) and 50 (blue) in the normal (solid) or inverted (dashed) hierarchy.

broaden in effect the line widths in the relevant atomic transitions. Because these line widths are affected by physical and spectroscopic properties of Xe atom, these parameters are summarized here.

The metastable state of Xe atom has long lifetime over 40 s for even isotopes in low-pressure gas phase. The radiative lifetimes of 42.9(9) s and 42.4(13) s for ^{132}Xe and ^{136}Xe respectively, are reported where the observation was performed in MOT (Magneto-optical trap) experiment [54]. The density of Xe atom can be increased up to $2.5 \times 10^{19} / \text{cm}^3$ with a pressure of 1 atm at room temperature. If the gas is cooled to 190 K (boiling point at pressure of 1 atom) and the pressure is increased to 3 atom, the number density reaches $1.1 \times 10^{20} / \text{cm}^3$. The atomic collision should be considered for relaxation of metastable atoms in relatively high density gas phase we here consider for our purpose ($> 10^{19} / \text{cm}^3$). The collisional relaxations (atom-atom and atom-wall) of the metastable Xe in a gas cell are also reported, where the observed relaxation rate takes minimum ($\sim 10^2 \text{ s}^{-1}$; depending on cell size) at a pressure of 0.2 - 1 Torr and reaches to $1 \times 10^4 \text{ s}^{-1}$ at 10 Torr [55]. From this reported result, the collisional relaxation time of the metastable state of $O(0.1 \sim 0.01) \mu\text{s}$ is expected at a pressure of 1 atm that is enough long for experimental RENP studies.

Populating Xe atoms into the metastable state is performed through two-photon excitation from the ground state to $5p^5(^2P_{3/2})6p$ states as shown in Fig. 40. Among these 6p-blanches the two states, $5p^5(^2P_{3/2})6p\ ^2[3/2]_2$ and $5p^5(^2P_{3/2})6p\ ^2[5/2]_2$, are allowed both for the two-photon excitation from the ground state and single-photon E1 transition to the metastable state in the A-type three-state system. Both of these 6p-states have E1-transitions to the $6s\ [3/2]_2$ (metastable) and $6s\ [3/2]_1$ which promptly decays into the ground state with E1 transition. The consecutive E1 decays through $6s\ [3/2]_1$ state is one of sources for relaxations and decoherences in the three-level system. The spectroscopic parameters for these two states including the wavelength λ_{tp} for two-photon and λ_{6sJ-6p} for the 6p-6s transitions, transition probabilities $A_{6sJ \leftarrow 6p}$, are summarized in Table 5. Among these two states,

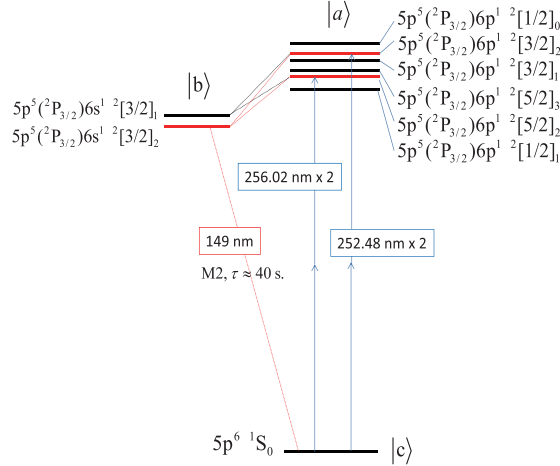


Fig. 40 Schematic energy level for populating Xe atom into metastable state.

Table 5 The parameters of relevant excited 6p states for populating Xe atoms into the metastable state $5p^5(2P_{3/2})6s^2[3/2]_2$. The values of transition probabilities $A_{6s_J \leftarrow 6p}$ are taken from [56].

-	E_{6p} (eV)	λ_{tp} (nm)	λ_{6s2-6p} (nm)	$A_{6s2 \leftarrow 6p}$ (s ⁻¹)	λ_{6s1-6p} (nm)	$A_{6s1 \leftarrow 6p}$ (s ⁻¹)
$5p^5(2P_{3/2})6p^2[3/2]_2$	9.821	252.5	823.4	2.24×10^7	895.5	9.42×10^6
$5p^5(2P_{3/2})6p^2[5/2]_2$	9.686	256.0	904.8	9.72×10^6	992.6	1.74×10^7

$5p^5(2P_{3/2})6p^2[3/2]_2$ is preferable in terms of usability of wavelength in IR region. Therefore this state is used in the following estimation for atomic coherences.

Another mechanism of the relaxation is the ionization of Xe atoms in excited 6p or 6s states due to absorption of third photon from the pump field. The first ionization energy of 12.1 eV for Xe is only 2.3 eV higher than the 6p state. The ionization rates for these states are proportional to the light field strength. There are some experimental and theoretical studies for ionization of Xe atoms in 6p states. For the state $5p^5 6p[3/2]_2$, the observed ionization rate of $\Gamma_I = 3.0 \cdot I_{252} [\text{s}^{-1}]$ is reported, where I_{252} is field strength of 252.5 nm in unit of W/cm^2 [57]. Although the metastable Xe atoms can also absorb the third photon to be ionized, the ionization rate of $\Gamma_I = 0.19 \cdot I_{252} [\text{s}^{-1}]$ roughly estimated by the reported photoionization cross section [58] is smaller than that of 6p state.

It must be noted also on the Doppler broadenings in each transition which affect the phase coherence in the relevant two states. At room temperature, the Doppler widths (FWHM) of the 5p-6p and 6p-6s transitions are 2.6 GHz and 0.40 GHz, respectively.

4.3.3. Coherence preparation and its measurement. Atomic coherence between the metastable and ground state in Xe atom is produced by two laser fields, one for two-photon excitation from ground $|c\rangle$ to the 6p state $|a\rangle$ (pump field with frequency ω_p), another for coupling between 6p and the metastable state $|b\rangle$ (coupling field with frequency ω_c). As

described previously, the preparation process of coherence includes the two-photon excitation and some relaxations and is then complex. Therefore, it is important to quantitatively estimate how large atomic coherence can be achieved. We then perform numerical simulations for the coherence of metastable Xe.

The time evolution of populations and coherences for Λ -type three-level system in the presence of the two laser fields are estimated by the optical-Bloch equations. The optical Bloch equation is the homogeneous (spatially constant) version of the Maxwell-Bloch equation in which the light-field is taken as given. The equations for the populations ρ_{aa} , ρ_{bb} and ρ_{cc} in each state are described as

$$\dot{\rho}_{aa} = \frac{i\Omega_{ab}}{2}(\tilde{\rho}_{ab} - \tilde{\rho}_{ba}) + \frac{i\Omega_{ac}}{2}(\tilde{\rho}_{ac} - \tilde{\rho}_{ca}) - (\Gamma_a^{(rad-all)} + \Gamma_a^{(ion)})\rho_{aa} \quad (82)$$

$$\dot{\rho}_{bb} = \frac{i\Omega_{ab}}{2}(\tilde{\rho}_{ba} - \tilde{\rho}_{ab}) - (\Gamma_b^{(ion)} + \Gamma_b^{(col)})\rho_{bb} + \frac{\Gamma_a^{(rad-meta)}}{2}\rho_{aa} \quad (83)$$

$$\dot{\rho}_{cc} = \frac{i\Omega_{ac}}{2}(\tilde{\rho}_{ca} - \tilde{\rho}_{ac}) + \frac{\Gamma_{a-c}^{(rad)}}{2}\rho_{aa}, \quad (84)$$

and similarly for the coherences, the following equations describe the time evolutions

$$\dot{\tilde{\rho}}_{ab} = -(\gamma_{ab} - i\delta_{ab})\tilde{\rho}_{ab} + \frac{i\Omega_{ab}}{2}(\rho_{aa} - \rho_{bb}) - \frac{i\Omega_{ac}}{2}\tilde{\rho}_{cb} \quad (85)$$

$$\dot{\tilde{\rho}}_{ac} = -(\gamma_{ac} - i\delta_{ac})\tilde{\rho}_{ac} + \frac{i\Omega_{ac}}{2}(\rho_{aa} - \rho_{cc}) - \frac{i\Omega_{ab}}{2}\tilde{\rho}_{bc} \quad (86)$$

$$\dot{\tilde{\rho}}_{cb} = -(\gamma_{cb} - i(\delta_{ab} - \delta_{ac}))\tilde{\rho}_{cb} + \frac{i\Omega_{ab}}{2}\rho_{ca} - \frac{i\Omega_{ac}}{2}\rho_{ab}. \quad (87)$$

Here the "slow" variables for coherences are introduced as

$$\tilde{\rho}_{ab} = \rho_{ab}e^{-i(\omega_{ab} - \omega_c)t}, \quad \tilde{\rho}_{ac} = \rho_{ac}e^{-i(\omega_{ac} - 2\omega_p)t}, \quad \tilde{\rho}_{cb} = \rho_{cb}e^{-i\omega_{cb}t}, \quad (88)$$

in order to move into appropriate rotating frames. Ω_{ac} and $\Omega_{ab} = \mu_{ab}E_c/\hbar$ represent the Rabi frequencies for the pump and coupling field, respectively. Ω_{ac} is defined as an effective two-photon Rabi frequency for the field at frequency of ω_p ; $\Omega_{ac} = \alpha_{ac}E_p^2/\hbar$, where $\alpha_{ac} = \sum_i \mu_{1i}\mu_{i2}/2\hbar(\omega_i - \omega_p)$ and the μ_{ij} indicates the corresponding dipole matrix elements. E_p and E_c are the amplitudes of the applied pump and coupling fields respectively, and these field amplitudes are described with corresponding intensities I of the incident lights as $E = \sqrt{2Z_0I} = 27.5\sqrt{I(\text{W/cm}^2)}$ V/cm. In these equations we include the spontaneous decay term $\Gamma_a^{(rad-all)}$ and $\Gamma_a^{(rad-meta)}$ corresponding the decay rates from $|a\rangle$ to two 6s states and only to the metastable state $|b\rangle$. These decay rates take the values $\Gamma_a^{(rad-all)} = 2.63 \times 10^7 \text{ s}^{-1}$ [59] and $\Gamma_a^{(rad-meta)} = 2.24 \times 10^7 \text{ s}^{-1}$ [56]. The state $|a\rangle$ tends to decay into the ground state $|c\rangle$ with two E1 decays through $5p6s^2[3/2]_1$ whose decay rate is estimated as $\Gamma_{a-c}^{(rad)} = (1/\Gamma_{a \rightarrow 6s1} + 1/\Gamma_{6s1 \rightarrow c})^{-1} = 9.1 \times 10^6 \text{ s}^{-1}$ [56, 60]. As described in the previous subsection, the states $|a\rangle$ and $|b\rangle$ also have decay rates $\Gamma_a^{(ion)}$ and $\Gamma_b^{(ion)}$ through ionization by the pump field as relaxation processes. The collisional loss of population in $|b\rangle$ is assumed $\Gamma_b^{(col)} = 5 \times 10^7 \text{ s}^{-1}$ (we here assume high density; $> 1 \text{ atm}$). In this calculation, the widths of Doppler broadening in each transition are included in the relaxation terms γ_{ij} in coherence. These values are $\gamma_{ac} = 1.6 \times 10^{10} \text{ s}^{-1}$, $\gamma_{ab} = 2.5 \times 10^9 \text{ s}^{-1}$, and $\gamma_{bc} = 1.4 \times 10^9 \text{ s}^{-1}$. The pressure broadening assumed to be $1 \times 10^9 \text{ s}^{-1}$ at a pressure of 1 atm (room temperature) is also considered in these decoherence terms. We assume that the detunings δ_{ab} and δ_{ac} in each field are larger

than the linewidths in the corresponding transitions, so that both of these transitions by the applied fields are adiabatic.

The dependence of population ρ_{aa} in the 6p state and the coherence ρ_{ac} between 6p and 5p states on the intensity of the incident pump light is firstly estimated by the above equations. The incident pump light is assumed to have a Gaussian envelope with a width of 5 ns and to have a peak intensity at $t = 10$ ns. The detuning δ_{ac} of pump frequency is assumed to be $1.2 \times 10^{10} \text{ s}^{-1}$ (2.0 GHz) so as to be larger than the Doppler broadening 1.3 GHz (HWHM). Figure 41 shows time evolutions of ρ_{ac} and ρ_{aa} when the pump field is applied. The effective

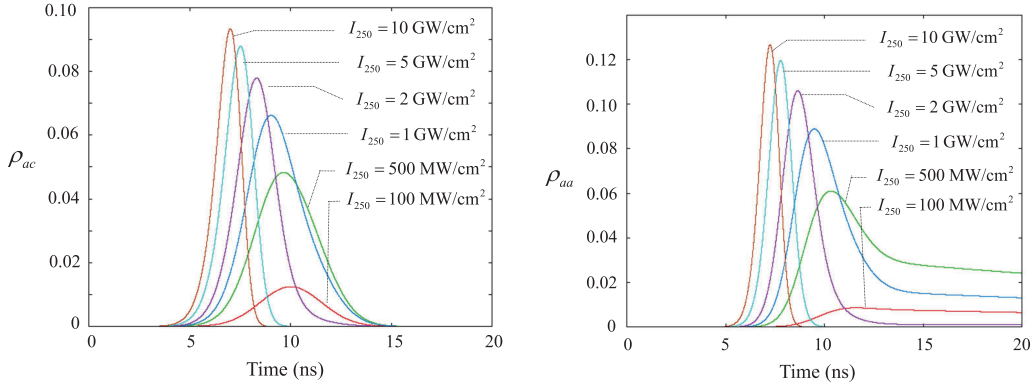


Fig. 41 Numerically calculated atomic coherence ρ_{ac} between ground state and 6p state (left panel) and the population ρ_{aa} (right panel) when only the two-photon field (252 nm) are applied.

two-photon Rabi frequency Ω_{ac} is calculated with the effective dipole moment α_{12} . Here only $6s^2[3/2]_1$ state is taken as the intermediate state $|i\rangle$ for calculating the α_{12} . Thus Ω_{ac} is estimated as

$$\Omega_{ac} = 5.44 \cdot I_{252} \text{ s}^{-1}, \quad (89)$$

where I_{252} denotes the pump-field strength in unit of W/cm^2 . These results shows that the effect of ionization loss starts to appear with the field strength of $I_{252} \approx 1 \text{ GW/cm}^2$, and that the coherence achieves $\rho_{ac} \approx 0.06$ at that field. The achievable coherence tends to saturate around $\rho_{ac} \approx 0.1$ due to the ionization effect.

The coherence ρ_{bc} between the metastable and the ground state is calculated by adding the coupling field of 823 nm to the above situation. The Rabi frequency for this transition can be calculated with the A -coefficient $A = 2.24 \times 10^7 \text{ s}^{-1}$ [56] in the transition as

$$\Omega_{ab} = 5.43 \times 10^8 \cdot \sqrt{I_{823}} \text{ s}^{-1} \quad (90)$$

where I_{823} is the coupling-field strength in unit of W/cm^2 . The estimated atomic coherences ρ_{bc} with $I_{823} = 10 \sim 5000 \text{ W/cm}^2$ and $I_{252} = 500 \text{ MW/cm}^2$ are summarized in Fig. 42. The populations ρ_{bb} in the metastable state are also shown in this Figure. The detuning δ_{bc} in coupling field is assumed to be $2.5 \times 10^9 \text{ s}^{-1}$ (0.4 GHz) which is larger than Doppler broadening 0.2 GHz (HWHM). The expected coherence increases to $\rho_{bc} = 0.01 \sim 0.1$ when the coupling Rabi frequency Ω_{ab} exceeds the two-photon Rabi frequency Ω_{ac} . As shown in the results, the coherence $\rho_{bc} = 0.05$ is available if the pump and coupling fields are increased

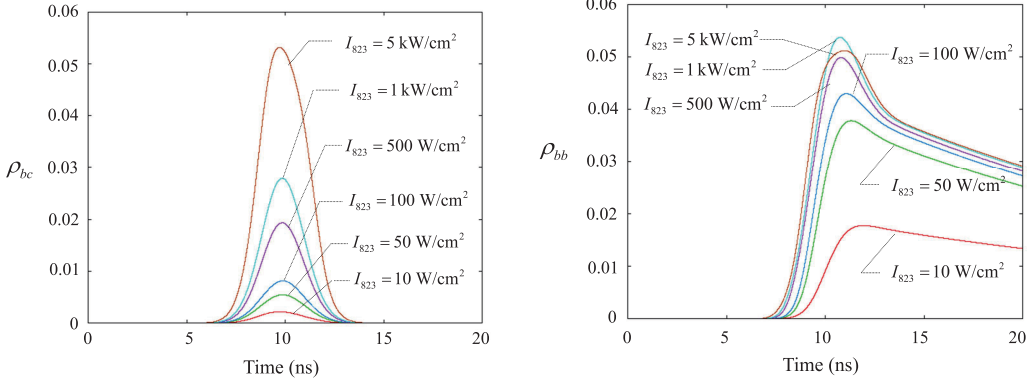


Fig. 42 Numerically calculated atomic coherence ρ_{bc} between the the metastable and ground states.

to $I_{250} = 500 \text{ MW/cm}^2$ and $I_{823} = 5 \text{ kW/cm}^2$. In this condition each Rabi frequency takes $\Omega_{ab} = 3.8 \times 10^{10} \text{ s}^{-1}$ and $\Omega_{ac} = 2.7 \times 10^9 \text{ s}^{-1}$. The population ρ_{bb} in the metastable state reaches ~ 0.05 under this condition.

There would not be straightforward way to confirm presence of coherence ρ_{bc} , because there is no adequate transition path between $|b\rangle$ and $|c\rangle$ for coherence measurements such as coherent anti-stokes Raman scattering (CARS). This is a same situation for both of the coherence between $6s_2$ ($|b\rangle$) and $5p^6$ ($|c\rangle$), and between $6s_1$ and $5p^6$. However, it is known that the three level system behaves as the dressed state system when the strong coupling field is applied (Rabi frequency exceeds the line broadening), and this strong coupling between these states can be confirmed by observing that absorption of the radiation from the state $|b\rangle$ to $|c\rangle$ is reduced, called as Electromagnetically Induced Transparency (EIT) [61]. A relevant case for this phenomenon was studied with atomic hydrogen [62] which has a similar Λ -type three-level structure as shown in Fig. 43. In both of these systems, the atoms are pumped to the excited state by two-photon transition and the atoms tend to be ionized by the applied fields. In the EIT experiments with hydrogen atom investigated in [62], the transparency of the VUV radiation (103 nm) from the $3p$ to the ground state and the reduction of the photoion signal from the atomic system were observed when the coupling Rabi frequency Ω_{2s-3p} exceeds the line broadening $\delta_{\text{Doppler}} = 2.3 \times 10^{11} \text{ s}^{-1}$. In Xe atom, this method can be applied to the three-level system of $|a\rangle$, $|c\rangle$ and $6s^2[3/2]_1$ (instead of $|b\rangle$), where the transparency of the VUV radiation (147 nm) from the $6s^2[3/2]_1$ is expected to be observed. The required condition for the applied coupling field in this experiment is $\Omega_{\text{coupling}} > \delta_{\text{Doppler}} \sim 2 \times 10^{10} \text{ s}^{-1}$ corresponding the coupling field intensity of $> 2 \text{ kW/cm}^2$. The coupling between the three states $|a\rangle$, $|b\rangle$ and $|c\rangle$, which is the target system in our studies, can be estimated from the observation in the above system and the numerical simulation. The reduction of the photoion signal with the EIT condition would also be useful for evaluation of the atomic coherence as the experiments with hydrogen.

4.3.4. Prospect for experiment. As described above, the atomic coherence of the metastable state in Xe atom is expected to reach $\rho_{bc} \sim 0.05$ which enables to study the RENP process by the numerical simulations where the pump and the coupling fields lead

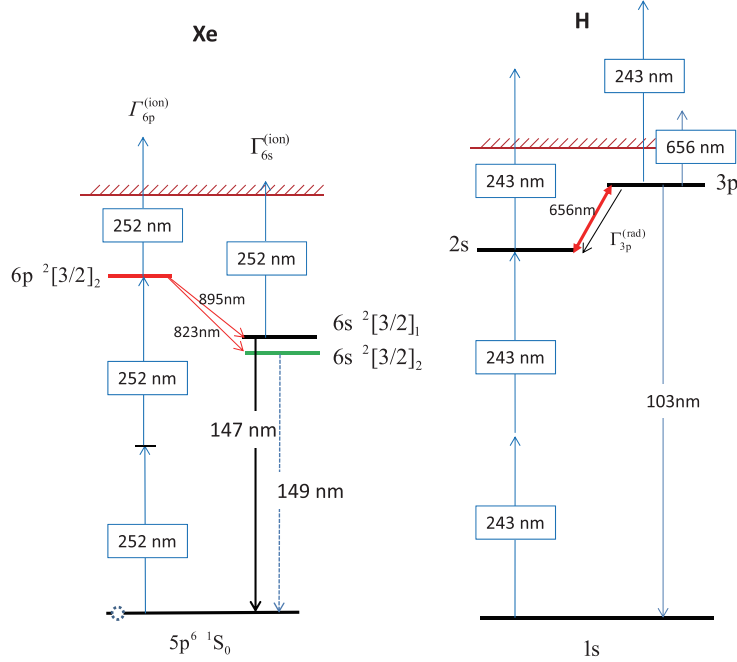


Fig. 43 Comparison of the Λ -type three-level systems between Xe and Hydrogen atom. The two-photon excitation scheme and the ionization are common in these species.

adiabatic transitions. In order to perform the experiments for the coherence preparation and measurement, the following experimental conditions are required:

- Linewidth of the applied fields is narrower than the line broadening
- Smooth temporal profile for the applied fields
- Smooth spacial profile for the applied fields.

The main broadening in Xe atom in gas phase arises from the Doppler effect, and estimated $1.6 \times 10^{10} \text{ s}^{-1}$ (2.6GHz(FWHM)) for two-photon transition and $2.5 \times 10^9 \text{ s}^{-1}$ (0.4GHz(FWHM)) for coupling transition at room temperature. The pressure broadening would not be negligible in the high-pressure atomic gas, which becomes $\sim 10^9 \text{ s}^{-1}$ at the pressure of 1 atm. The required linewidth is then $< 100 \text{ MHz}$. Therefore the laser system with enough narrow linewidth such as an injection seeded Ti:Sapphire is required (Sec.4.2.2). As listed above the applied fields should have smooth spacial profiles for both of the pump and coupling, and these fields should be overlapped in space. The available field strength should be estimated with the realistic beam diameter for this overlapping. If the beam diameters are assumed that $\phi_{\text{pump}} = 0.2 \text{ mm}$, $\phi_{\text{coupling}} = 0.5 \text{ mm}$ and the pulse energy is assumed 10 mJ/pulse with a pulse width of 10 ns for both fields, the field strength can then reach $I_{\text{pump}} = 600 \text{ MW/cm}^2$ and $I_{\text{coupling}} = 100 \text{ MW/cm}^2$ with which the coherence ρ_{bc} becomes > 0.05 .

The conceptual setup for the experiment is shown in Fig. 44. The high-quality pulsed beams for pump and coupling can be produced with Ti:S lasers injection seeded by Nd:YAG laser. The pumping field of 252 nm is obtained through third harmonic generation (THG) by using BBO crystals from the output beam of a Ti:S Laser. The detectors includes a

monochromator and a photomultiplier (PMT) for the light, and an electron multiplier (EMT) for the ionized Xe. The fundamental experiment as R&D for spectroscopy of the metastable Xe is now being performed with relatively broad linewidth lasers such as a pulsed Dye. It contains spectroscopy of transitions from the two-photon excited 6p states, investigation of populations in the metastable state, and lifetime of the metastable states.

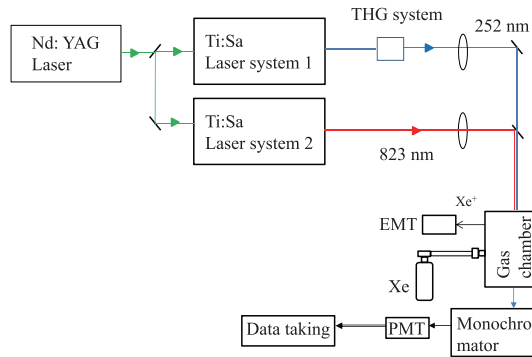


Fig. 44 The conceptual setup for the coherence preparation and measurement of Xe.

5. Summary and prospects

In the present work we first explained in detail theoretical principles of the neutrino mass spectroscopy with atoms and molecules, which aims at determination of undetermined important neutrino parameters. The key idea for measurements is to amplify otherwise small rates of radiative emission of neutrino pair (RENP), $|e\rangle \rightarrow |g\rangle + \gamma + \nu_i \nu_j$ (with ν_i, ν_j mass eigenstates), by developing the macro-coherent medium polarization among target atoms/molecules strongly coupled to fields inside the medium, in order to stimulate the process cooperatively. The amplification is realized by trigger irradiation of two colors into a well prepared target state of good phase coherence between atoms in two relevant levels, $|e\rangle$ and $|g\rangle$. The amplification also works for two-photon emission called paired super-radiance (PSR), $|e\rangle \rightarrow |g\rangle + \gamma + \gamma$. Detailed account of the master equation for PSR and coherence development for RENP is presented and results of numerical simulations on the pH₂ $Xv = 1$ vibrational transition have been presented both for explosive PSR events and events in the weaker linear regime. Our master equation includes effects of phase decoherence of medium polarization and decay of population difference.

By selecting a metastable state $|e\rangle$ forbidden to decay to lower levels via E1 transition, one can obtain a large E1×E1 two-photon PSR rate for $|e\rangle \rightarrow |g\rangle$. A good example of this feature is pH₂ vibrational transition $Xv = 1 \rightarrow 0$. The PSR event may occur explosively, as shown in Figure 4 of Section 1, if the target relaxation time T_2 is larger than some number, for the target number density $n = 10^{21} \text{ cm}^{-3}$ this number being of order a few to several nano seconds. Even for smaller T_2 's, the enhanced output over the input trigger is expected

as discussed in Section 4. Discovery of these PSR events serves to prove our principle of macro-coherence, a necessary prerequisite for RENP experiments.

The RENP spectral rate is given by the factorized formula $\Gamma_{\gamma 2\nu}(\omega) = \Gamma_0 I(\omega) \eta_\omega(t)$. The factor Γ_0 determines the overall rate in the unit of 1/time, and for Xe it is of order, 1 Hz $(n/10^{22} \text{cm}^{-3})^3 (V/10^2 \text{cm}^3)$. The spectral shape as a function of photon energy ω is given by $I(\omega)$, which serves to determine the neutrino parameters. Detailed photon spectrum calculations of Xe and I₂ transitions, having available energy 8.3 eV and 0.88 eV, respectively, have been given to explain how the parameter determination is made possible. The dynamical factor $\eta_\omega(t)$ is the space integrated quantity over the entire target of $|\vec{E}^-(R_1 - iR_2)|^2/(4\epsilon_{eg}n^3)$, the dimensionless squared product of the coherent polarization $(R_1 - iR_2)/2$ and the field $E^{(-)}$ inside the target.

The dynamical factor $\eta_\omega(t)$ is highly time dependent in the phase of large PSR related activities. It asymptotically approaches a constant value of the stable state made of field condensate supported by coherent medium polarization. For RENP it is important to utilize this factor as large as possible. How the condensate state is described is explained and a sample simulation has been presented, leaving more detailed investigation to future works. If the amplification works as expected, the absolute neutrino mass determination along with distinction of mass hierarchy pattern (normal or inverted) becomes feasible. Other important neutrino parameters such as Majorana/Dirac distinction along with CP violating phases may also be determined if the initial metastable atomic state lies close to the ground level, preferably within a fraction of eV.

Heavy atoms/molecules which have a large breaking of the *LS* coupling scheme are favored for RENP target candidates, since they may give a large enough amplitude of M1×E1 type for RENP between $|e\rangle$ and $|g\rangle$.

In the later half of the paper experimental status of our project has been reported, along with an overview of the entire experimental strategy.

Our basic strategy towards precision neutrino mass spectroscopy is first to prove the macro-coherent amplification principle by the PSR process. To this end, we have chosen gas-phase para-hydrogen (pH₂) as a target, and focus on the E1 forbidden transition from the vibrational excited state Xv=1 to the ground state Xv=0. As is discussed in Sec.2 and 4, PSR is highly non-linear phenomenon, and can be observed only when a certain set of initial conditions are realized. In the case of pH₂, they are the number density (n), the initial coherence (r_1 or r_2), and dephasing time (T_2 and T_3). We expect all necessary condition can be fulfilled in the current technology available to us at least for observing PSR events in the linear regime. As described in Sec.4, all components are prepared, and ready for the experiments.

It is crucial to achieve a large value of the RENP dynamical factor $\eta_\omega(t)$ to realize high precision mass spectroscopy. We plan to study evolution of macroscopic coherence and formation of field condensates, both of which directly affects $\eta_\omega(t)$, using Xe atom as an experimental platform. Details of the current status on the Xe experiment can be found in Sec.4.3. Condensed-phase targets are highly desirable not only for RENP experiments but also for observation of explosive PSR events. We are seeking and trying to develop high density solid targets with long dephasing time. Some preliminary results of our efforts along this line are presented in Appendix D and E.

It is evident that we need much more detailed simulations and experimental studies on how best we should design this challenging experiment. Some entirely new idea is welcome and may further enlighten prospects towards this important objective of neutrino physics.

Note added in proof. After the original submission of the manuscript some of us succeeded in deriving breathing solitons which are useful as an ideal target state for radiative neutrino pair emission (RENP). This shall be discussed elsewhere in a separate work [92].

Acknowledgment

We should like to thank M. Katsuragawa, K. Kawaguchi, Y. Kubozono, T. Momose, S.T. Petcov, and S. Yabushita for many helpful discussions and comments on this project. This research was partially supported by Grant-in-Aid for Scientific Research A (21244032), Grant-in-Aid for Challenging Exploratory Research (24654132), and Grant-in-Aid for Scientific Research on Innovative Areas "Extreme quantum world opened up by atoms" (21104002) from the Ministry of Education, Culture, Sports, Science, and Technology of Japan.

A. Electroweak interaction under nuclear Coulomb potential

A.1. Electrons in atom and their electromagnetic interaction

Electrons in an atom are described by solutions of the Dirac equation under the nuclear Coulomb potential [63] augmented by interaction with other electrons in the atom. Bound and nearly free (modified by the nuclear Coulomb field) electron states thus obtained form a complete set of states that may be used as an expansion basis of electron field denoted by a four component operator $\psi_e(\vec{x}, t)$. The interaction of atomic electrons with the electromagnetic field $\vec{A}(\vec{x}, t)$ is best described in physical terms by using the radiation gauge, as given for instance in standard textbooks of QED such as [63]. The radiation gauge field satisfies $\vec{\nabla} \cdot \vec{A} = 0$ and possesses two transverse degrees of freedom representing two transverse waves of photon. In this gauge the static Coulomb interaction is separated from the transverse field interaction, hence is convenient for our purpose.

In the present work we deal with interaction of atomic electrons with the transverse electromagnetic field \vec{A} and three massive neutrino field ν_i . This way we can derive an effective hamiltonian of atomic electrons in the electroweak theory [11] we need for our purpose.

In most cases of atomic electrons relativistic effects are minor and atomic electrons have bound energies much less than the electron rest mass. Or equivalently, the average electron velocity within an atom is much less than the light velocity. This makes non-relativistic treatment sufficient, although in some cases relativistic corrections such as LS coupling are important. Under this circumstance the electron field operator can be decomposed into two parts; a large and a small two-component fields. The major large two-component field is denoted by a new operator $\phi_e(\vec{x}, t)$.

As is well known [63], the electromagnetic interaction of atomic electrons is governed by interaction hamiltonian (or rather the hamiltonian density to be spatially integrated),

$$e\phi_e^\dagger(\vec{x}, t)(-i\vec{\nabla}) \cdot \vec{A}(\vec{x}, t)\phi_e(\vec{x}, t). \quad (\text{A1})$$

When this interaction hamiltonian is applied to atomic process, it gives a vertex amplitude for the atomic transition $|i\rangle \rightarrow |f\rangle$,

$$e\varphi_f^\dagger(\vec{x}, t)(-i\vec{\nabla}) \cdot \vec{A}(\vec{x}, t)\varphi_i(\vec{x}, t), \quad (\text{A2})$$

where φ_a is a wave function solving the nuclear Coulomb potential problem [17].

A further simplification arises by taking the long wavelength limit of emitted photons (the wavelength of photon much larger than the atomic size), and this leads to what is called the

E1 transition in the literature [63], [17], where one can replace the vertex amplitude above by

$$\varphi_f^\dagger(\vec{x}, t) \vec{d} \cdot \vec{E}(\vec{x}, t) \varphi_i(\vec{x}, t), \quad \vec{d} = e \vec{x}. \quad (\text{A3})$$

In the many-electron system in atom the dipole operator \vec{d} should be replaced by a summed quantity over all contributing electrons at position \vec{x}_n ; $\vec{d} = e \sum_n \vec{x}_n$. The wave functions φ should also be replaced by those of the multi-electron states [17].

A.2. Quantized massive neutrino fields

We have two possibilities to describe massive neutrinos: one is the Dirac type and another is the Majorana one. The neutrino and the anti-neutrino are distinct particles in the Dirac case, while they are identical in the Majorana case. RENP final states discriminate these cases due to the identical particle effect as explained in Secs. 1 and 3. The neutrino expansion base may be taken, effectively and conveniently, as plane wave functions, since the neutrino interaction with atomic nuclei is very weak.

For the Dirac type, a quantized free neutrino field is represented as

$$\psi^D(x) = \sum_{p,\lambda} \left[b(p, \lambda) u(p, \lambda) e^{-ipx} + d^\dagger(p, \lambda) v(p, \lambda) e^{ipx} \right], \quad (\text{A4})$$

where $b(p, \lambda)$ is the annihilation operator of the neutrino with a momentum p and a helicity λ , and $d^\dagger(p, \lambda)$ denotes the creation operator of the anti-neutrino. The four-component spinors $u(p, \lambda) e^{-ipx}$ and $v(p, \lambda) e^{ipx}$ are solutions of the Dirac equation. We employ the following convention for the neutrino momentum sum,

$$\sum_p = \int \frac{d^3 p}{(2\pi)^3 2E_p}, \quad (\text{A5})$$

where $E_p = \sqrt{m^2 + \vec{p}^2}$ is the energy of neutrino of mass m . The Dirac field ψ^D either annihilates a neutrino or creates an anti-neutrino. A free Majorana neutrino field is quantized as

$$\psi^M(x) = \sum_{p,\lambda} \left[b(p, \lambda) u(p, \lambda) e^{-ipx} + b^\dagger(p, \lambda) v(p, \lambda) e^{ipx} \right], \quad (\text{A6})$$

where b (b^\dagger) represents the annihilation (creation) operator of the Majorana neutrino and ψ^M satisfies $\psi^M = C(\bar{\psi}^M)^T$ with C being the charge conjugation matrix.⁵ We note that there is no distinction between neutrinos and anti-neutrinos in the Majorana case, and both the creation and annihilation operators of the Majorana neutrino appear in ψ^M .

A.3. Effective interaction of neutrinos with electrons

The neutrino fields in the flavor eigen-basis are related to those in the mass eigen-basis by a unitary transformation as

$$\nu_\alpha(x) = \sum_i U_{\alpha i} \nu_i(x), \quad (\text{A7})$$

where $\alpha = e, \mu, \tau$ specifies a neutrino flavor, $i = 1, 2, 3$ denotes a mass eigenstate, and $\nu_i(x) = \psi^D(x)$ or $\psi^M(x)$ with mass m_i . The lepton mixing matrix is written as a product of two

⁵ This ψ^M effectively reduces to two independent solutions in accordance with two-component formalism. The field quantization in the two-component formalism is given in [11] and [9].

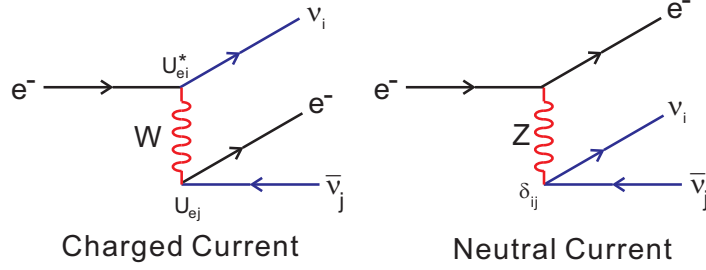


Fig. A1 Feynman diagram for W and Z exchange weak interaction of electron with neutrinos.

unitary matrices [1]:

$$U = VP, \quad (\text{A8})$$

where

$$V = \begin{bmatrix} c_{12}c_{13} & s_{12}c_{13} & s_{13}e^{-i\delta} \\ -s_{12}c_{23} - c_{12}s_{23}s_{13}e^{i\delta} & c_{12}c_{23} - s_{12}s_{23}s_{13}e^{i\delta} & s_{23}c_{13} \\ s_{12}s_{23} - c_{12}c_{23}s_{13}e^{i\delta} & c_{12}c_{23} - s_{12}s_{23}s_{13}e^{i\delta} & c_{23}c_{13} \end{bmatrix}, \quad (\text{A9})$$

with $c_{ij} = \cos \theta_{ij}$ and $s_{ij} = \sin \theta_{ij}$. The diagonal unitary matrix P may be expressed by

$$P = \text{diag.}(1, e^{i\alpha}, e^{i\beta}), \quad (\text{A10})$$

for Majorana neutrinos, and we rotate away the phases α and β for Dirac neutrinos.

The effective interaction of neutrinos with the electron field arises from W and Z exchange CC and NC interaction [11], as depicted in Fig.A1, and is given by

$$\mathcal{H}_{\text{eff}} = \frac{G_F}{\sqrt{2}} \sum_{i,j} \bar{\nu}_i \gamma^\mu (1 - \gamma_5) \nu_j \bar{e} \gamma_\mu (v_{ij} - a_{ij} \gamma_5) e, \quad (\text{A11})$$

where

$$v_{ij} = U_{ei}^* U_{ej} - \left(\frac{1}{2} - 2 \sin^2 \theta_W \right) \delta_{ij}, \quad a_{ij} = U_{ei}^* U_{ej} - \frac{1}{2} \delta_{ij}. \quad (\text{A12})$$

The interaction above is written using the four component spinor notation. It has been shown that for non-relativistic atomic electrons the leading neutrino interaction stems from the axial-vector part and in the two-component notation it can be written using the spin operator of the form,

$$\nu^\dagger \vec{\sigma} \nu \cdot \phi_e^\dagger \vec{\sigma} \phi_e. \quad (\text{A13})$$

This results in the magnetic type of transition operator on the electron side. We may thus use, for the spin matrix element of atomic transitions from a bound state $|a\rangle$ to $|b\rangle$, their wave functions $\varphi_a(\vec{r})$, $\varphi_b(\vec{r})$, and compute the overlapping integral of the kind,

$$\int d^3r \varphi_a^*(\vec{r}) \vec{S}_e \varphi_b(\vec{r}). \quad (\text{A14})$$

In practice, it is better to use experimental data for this if they are available.

B. Mathematical structure of Maxwell-Bloch equation

B.1. Maxwell-Bloch equation for SR

We consider equations, Eq. 19 ~ 21 in the text, for the single photon SR. First rescale time, length and field by

$$\tau = \frac{t}{T_R}, \quad \xi = \frac{x}{T_R}, \quad e = -idT_R E, \quad (\text{B1})$$

where T_R should have the dimension of time/length. It is further convenient to introduce the retarded time $\tau_- = \tau - \xi$ and use (τ_-, ξ) as independent variables. In terms of these the Maxwell-Bloch equation is converted to

$$\partial_- R = Ze, \quad (\text{B2})$$

$$\partial_- Z = -\frac{1}{2}(e^* R + e R^*), \quad (\text{B3})$$

$$\partial_\xi e = R, \quad (\text{B4})$$

with $T_R = 1/\sqrt{2\pi\omega d^2 n}$ determined from consistency.

Using the conservation law that follows, $\partial_-(|R|^2 + Z^2) = 0$, we introduce an angle function $\theta(\tau_-, \xi)$:

$$R = e^{i\varphi} B(\xi) \sin \theta(\tau_-, \xi), \quad Z = B(\xi) \cos \theta(\tau_-, \xi). \quad (\text{B5})$$

In order to avoid unnecessary complication we assume real field e and set the phase $\varphi = 0$. The Maxwell-Bloch equation then becomes

$$\frac{\partial^2}{\partial_- \partial_\xi} \theta = B \sin \theta, \quad (\text{B6})$$

$$e = \partial_- \theta. \quad (\text{B7})$$

The first equation is known as the sine-Gordon equation in 1+1 space-time dimensions.

Scaling invariance under $\tau_- \rightarrow \beta \tau_-, \xi \rightarrow \beta^{-1} \xi$, exists in this system. The Burnham-Chiao equation [64] is obtained using the variable, $w = 2\sqrt{\tau_- \xi} = 2\sqrt{(\tau - \xi)\xi}$,

$$\frac{d^2 \theta}{dw^2} + \frac{1}{w} \frac{d\theta}{dw} = B \sin \theta. \quad (\text{B8})$$

Since this is an ordinary differential equation, it is much easier to solve than 1+1 dimensional partial differential equation. This solution is illustrated in Fig.B1, which shows interesting ringing structure of emitted pulses.

B.2. Maxwell-Bloch equation for PSR

We recapitulate the master equation for the most general case of two-color trigger irradiation of frequencies $\omega_1 + \omega_2 = \epsilon_{eg}$, as given in [14].

We introduce the dimensionless unit:

$$(\xi, \tau) = (\mu x, \mu t), \quad \mu(\omega) = \epsilon_{eg} n \alpha_{ge}(\omega, \epsilon_{eg} - \omega), \quad |e_{L,R}^{(1),(2)}|^2 = \frac{|E_{L,R}^{(1),(2)}|^2}{\epsilon_{eg} n}, \quad r_i = \frac{R_i}{n}, \quad (\text{B9})$$

$$\alpha_{ge}(\omega, \epsilon_{eg} - \omega) = \frac{d_{pe} d_{pg} (\epsilon_{pg} + \epsilon_{pe})}{(\epsilon_{pe} + \omega)(\epsilon_{pg} - \omega)}. \quad (\text{B10})$$

Assume R-mover field of frequency ω_1 and L-mover of frequency ω_2 (neither R-mover of frequency ω_2 nor L-mover of frequency ω_1). Note the frequency dependence of coupling parameters $\alpha_{ab}(\omega_1, \omega_2)$ and the universal relation $\alpha_{eg}(\omega_1, \omega_2) = \alpha_{ge}(\omega_1, \omega_2)$ for any

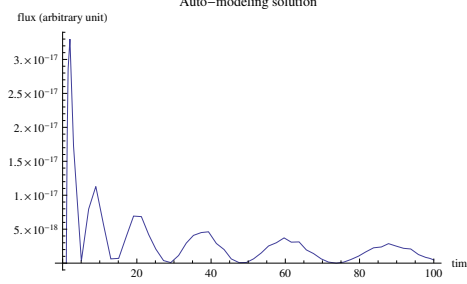


Fig. B1 Auto-modeling solution numerically computed from eq.(B8). Initial values are $\theta(\tau = 2 \times 10^{-6}) = 10^{-8}$, $\theta(\tau = 2 \times 10^{-6}) = 0$ and target length = 1. Constant $B \sim 1$ is assumed.

combination of $\omega_1 + \omega_2 = \epsilon_{eg}$. The master equations for medium polarization and fields are

$$\begin{aligned} \partial_\tau r_1^{(0)} &= 2(\gamma_-^{(1)}|e_R|^2 + \gamma_-^{(2)}|e_L|^2)r_2^{(0)} + 4\Im(e_Re_L)r_3^{(0)} + 2\gamma_-^{(12)}e_Re_L^*r_2^{(-)} + 2\gamma_-^{(21)}e_L e_R^*r_2^{(+)} \\ &\quad -i(e_L^2 - (e_R^*)^2)r_3^{(+)} - i(e_R^2 - (e_L^*)^2)r_3^{(-)} - \frac{r_1^{(0)}}{\tau_2}, \end{aligned} \quad (\text{B11})$$

$$\partial_\tau r_1^{(+)} = 2\gamma_-^{(12)}e_Re_L^*r_2^{(0)} - i(e_R^2 - (e_L^*)^2)r_3^{(0)} + 2(\gamma_-^{(1)}|e_R|^2 + \gamma_-^{(2)}|e_L|^2)r_2^{(+)} + 4\Im(e_Re_L)r_3^{(+)} - \frac{r_1^{(+)}}{\tau_2}, \quad (\text{B12})$$

$$\begin{aligned} \partial_\tau r_2^{(0)} &= -2(\gamma_-^{(1)}|e_R|^2 + \gamma_-^{(2)}|e_L|^2)r_1^{(0)} + 4\Re(e_Re_L)r_3^{(0)} - 2\gamma_-^{(12)}e_Re_L^*r_1^{(-)} - 2\gamma_-^{(21)}e_L e_R^*r_1^{(+)} \\ &\quad + (e_L^2 + (e_R^*)^2)r_3^{(+)} + (e_R^2 + (e_L^*)^2)r_3^{(-)} - \frac{r_2^{(0)}}{\tau_2}, \end{aligned} \quad (\text{B13})$$

$$\partial_\tau r_2^{(+)} = -2\gamma_-^{(12)}e_Re_L^*r_1^{(0)} + (e_R^2 + (e_L^*)^2)r_3^{(0)} - 2(\gamma_-^{(1)}|e_R|^2 + \gamma_-^{(2)}|e_L|^2)r_1^{(+)} + 4\Re(e_Re_L)r_3^{(+)} - \frac{r_2^{(+)}}{\tau_2}, \quad (\text{B14})$$

$$\begin{aligned} \partial_\tau r_3^{(0)} &= -4\left(\Re(e_Re_L)r_2^{(0)} + \Im(e_Re_L)r_1^{(0)}\right) + i(e_R^2 - (e_L^*)^2)r_1^{(-)} + i(e_L^2 - (e_R^*)^2)r_1^{(+)} \\ &\quad - (e_L^2 + (e_R^*)^2)r_2^{(+)} - (e_R^2 + (e_L^*)^2)r_2^{(-)} - \frac{r_3^{(0)} + 1}{\tau_1}, \end{aligned} \quad (\text{B15})$$

$$\partial_\tau r_3^{(+)} = ir_1^{(0)}(e_R^2 - (e_L^*)^2) - r_2^{(0)}(e_R^2 + (e_L^*)^2) - 4\left(\Re(e_Re_L)r_2^{(+)} + \Im(e_Re_L)r_1^{(+)}\right) - \frac{r_3^{(+)}}{\tau_1}, \quad (\text{B16})$$

$$(\partial_\tau + \partial_\xi)e_R = \frac{ia_1}{4}(\gamma_+^{(1)} + \gamma_-^{(1)}r_3^{(0)})e_R + \frac{i}{4}\gamma_-^{(12)}r_3^{(+)}e_L + \frac{ia_{12}}{4}(r_1^{(0)} - ir_2^{(0)})e_L^* + \frac{i}{4}(r_1^{(+)} - ir_2^{(+)})e_R^*, \quad (\text{B17})$$

$$(\partial_\tau - \partial_\xi)e_L = \frac{ia_2}{4}(\gamma_+^{(2)} + \gamma_-^{(2)}r_3^{(0)})e_L + \frac{i}{4}\gamma_-^{(21)}r_3^{(-)}e_R + \frac{ia_{21}}{4}(r_1^{(0)} - ir_2^{(0)})e_R^* + \frac{i}{4}(r_1^{(-)} - ir_2^{(-)})e_L^*. \quad (\text{B18})$$

$$\gamma_\pm^{(a)} = \frac{\alpha_{ee}(\omega_a, \omega_a) \pm \alpha_{gg}(\omega_a, \omega_a)}{2\alpha_{ge}}, \quad \gamma_\pm^{(ab)} = \frac{\alpha_{ee}(\omega_a, \omega_b) \pm \alpha_{gg}(\omega_a, \omega_b)}{2\alpha_{ge}}, \quad (\text{B19})$$

$$a_i = \frac{2\omega_i}{\epsilon_{eg}}, \quad a_{ij} = \frac{2\omega_j^2}{\omega_i \epsilon_{eg}}, \quad (\text{B20})$$

with α_{aa} defined by

$$\alpha_{aa}(\omega_1, \omega_2) = \frac{d_{pa}^2(2\epsilon_{pa} + \omega_1 - \omega_2)}{(\epsilon_{pa} + \omega_1)(\epsilon_{pa} - \omega_2)}. \quad (\text{B21})$$

The single mode equations in the text are readily derived by taking $\omega_i = \epsilon_{eg}/2$, $a_i = 1$, $a_{ij} = 1$ and all $\gamma_{\pm}^{(ab)}$ a, b -independent.

C. Molecules for RENP

Molecules are interesting candidates for RENP measurements from a variety of reasons: (1) they have a rich structure in energy levels, in particular energy level spacing of vibrational bands may give features of the photon energy spectrum helpful for identification of the RENP process; (2) closeness of different parity levels may enhance parity violating effects.

In this Appendix we explain basic facts on molecules and present crude estimates related to molecular RENP, by taking I_2 molecule as an example. In the fundamental Born-Oppenheimer approximation [17] the molecular wave function of diatomic molecules consists of three parts; electronic, vibrational, and rotational parts. Energy scale associated with each of these is clearly separated reflecting three different time scales of their motion.

The vibrational part of wave function is usually derived after electronic wave functions of energy eigenstates are calculated taking the nuclear distance of two atoms fixed. For each fixed nuclear distance one has different energy functions corresponding to different electronic states. These energy functions are called potential curves. Potential curves have different equilibrium nuclear distances denoted by r_e (corresponding to different positions of energy minima) and different curvatures ω_e at these minima, as illustrated in the conceptual diagram in Sec.3. We need to compute matrix elements of electronic operators such as electronic spin \vec{S} and electric dipole \vec{d} . Even for two different electronic states these electronic operators have non-trivial overlap of vibrational wave functions because of different equilibrium distances and potential curvatures. This gives rise to the Franck-Condon (FC) factor, as computed below.

For simplicity we construct as a model of potential curves the Morse potential from molecular experimental data of Table 2 given in Sec.3 and calculate the FC factors we need for RENP spectrum computations.

C.1. Morse potential and vibrational energy eigenstates

The Morse potential is a three-parameter fit to the potential curve and is given by

$$V(r) = D_e \left(1 - e^{-a(r-r_e)}\right)^2 - D_e, \quad (\text{C1})$$

$$a = \sqrt{\frac{m}{2D_e}}\omega_e, \quad (\text{C2})$$

with m the effective mass of two nuclei, in this case the half of I atom. This potential curve is plotted for X , A' and A states, three lowest electronic states in Fig.C1, along with three vibrational levels.

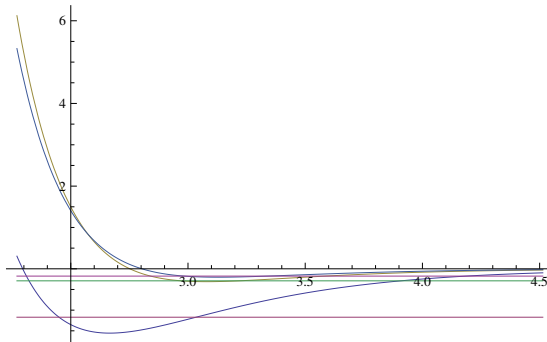


Fig. C1 The Morse potential for states, X(v=15 indicated), A'(v=1) and A(v=2).

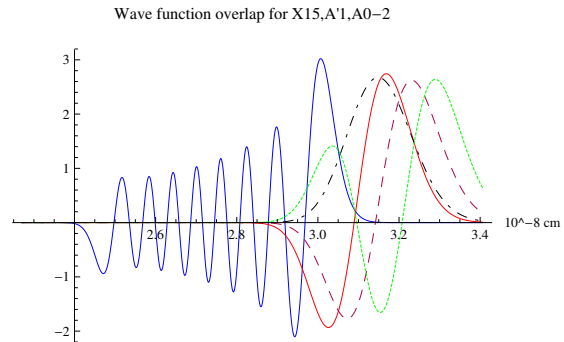


Fig. C2 Vibrational wave functions for Xv=15, A'v=1 and Av = 0 ~ 2

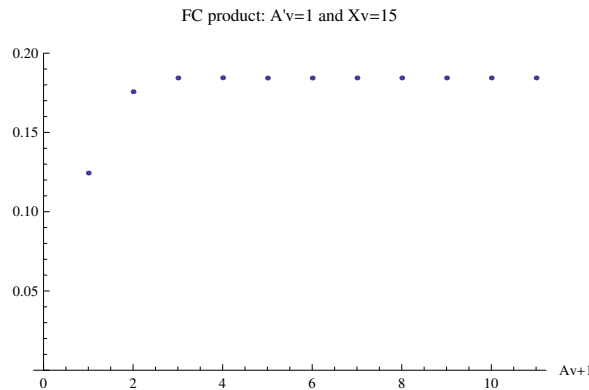


Fig. C3 FC product between A' and X: the intermediate sum is taken up to Av (plotted abscissa is $Av+1$).

This potential has analytic solutions for the energy eigenvalue problem:

$$E_v = \omega_e(v + \frac{1}{2}) - \frac{\omega_e^2}{4D_e}(v + \frac{1}{2})^2 - D_e, \quad v = 0, 1, \dots [\lambda - \frac{1}{2}], \quad \lambda = \frac{4D_e}{\omega_e}. \quad (\text{C3})$$

The wave functions are given in terms of the associated Laguerre polynomial L_v^α . Examples of these wave functions are shown in Fig.C.1.

C.2. FC factors

The Franck-Condon (FC) factor is the overlap of vibrational wave functions, for instance between A'-A, and A-X. We need a product of FC factors between A'-A and A-X for RENP amplitude calculation. Result of FC product between A' and X for summation up to Av is shown in Fig.C3, which indicates that the approach to the final product value is fast, already seen $Av \sim 2$.

C.3. RENP spectrum

The RENP spectral shape given in the text is used. We neglect the spin factor \vec{S} expected to be order unity, and further ignore the presence of rotational levels. Examples of the photon spectrum function $I(\omega)$ are shown in Fig.C4 ~ Fig.C5. The molecular spin factor

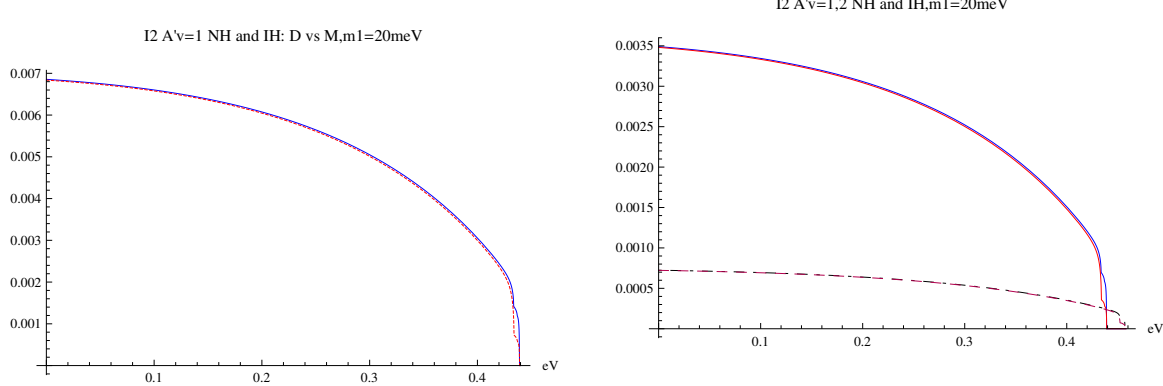


Fig. C4 I_2 RENP spectrum between $A' v=1$ and $Xv=15$. IH vs NH is compared, using the smallest neutrino mass 20 meV. The vertical scale is in arbitrary units.

Fig. C5 I_2 RENP spectrum between $A' v=1$ and $Xv=15$ in solid, and $A' v=2$ and $Xv=14$ in dashed. IH vs NH is compared, for two cases of the smallest neutrino mass 2 (in dashed) and 20 (in solid) meV. The vertical scale is in arbitrary units.

has been taken as a constant for simplicity. A more accurate calculation including the correct treatment of the spin factor is in progress [24].

C.4. The $I_2 A'$ state

In this Subsection, we briefly describe how to produce the metastable A' states. I_2 molecules form stable solids at room temperature with relatively high vapor pressure (~ 0.5 Torr). Fig. C6 shows saturated vapor pressure of iodine.[65] It is possible to prepare 1 atm I_2 gas by heating up to about 450 K. Therefore, I_2 is an easy-to-handle sample for both gas phase or matrix isolation experiments. Actually, many spectroscopic studies of I_2 has been performed in both phases. In gas phase, however, at least three photons are needed to access the A' state from X state. For example, $X \rightarrow A \rightarrow a \rightarrow A'$ may be possible by pure optical transition. As an alternative pathway, Koffend et al. used collisional induced transition to prepare the A' state.[66] On the other hand, solid environment makes access to the A' state easy. It is known that $A' - X$ transition is weakly dipole-allowed by interaction with a matrix. [67] This may be advantageous for preparing initial population in the A' state while both T_1 and T_2 in the solid phase are much shorter than in the gas phase.

D. Coherence time measurements of para-hydrogen vibrational levels

D.1. TRCARS method

Solid para-hydrogen (pH₂) is an attractive target to study the PSR phenomenon. Its properties of high density (2.6×10^{22} molecules cm⁻³) and long coherence time are well suited to observe explosive type PSR events, as discussed in Sec. 2. In this Appendix, we focus on the $v = 2$ (overtone) vibrational level of pH₂, one possible initial state for PSR. Previous studies have reported that the $v = 1$ (of consisting H₂ molecules) coherence decay exceeds 10 ns [68–71], that is quite long as a condensed sample. A direct coherence time measurement

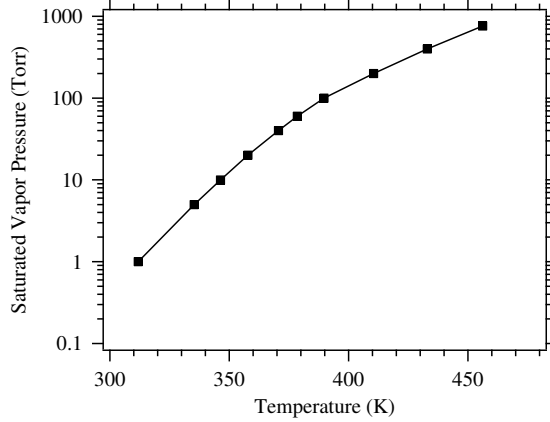


Fig. C6 Saturated vapor pressure of iodine.[65]

is possible by investigating the temporal change in time-domain spectra. With this method, the coherence decay of the $v = 1$ state has been studied already [71]. Below, we describe our time-domain examination of the coherence decay of the overtone $v = 2$ state of solid para-hydrogen.

TRCARS (time-resolved coherent anti-Stokes Raman scattering) [72] is a technique to trace the coherence decay in a real-time basis for Raman-type transitions. This is applicable to para-hydrogen vibrational levels since they are Raman-active. In this technique, the coherence produced by a short excitation pulse pair (pump and Stokes, whose energy difference is equal to the Raman transition frequency ω_0) are monitored by a delayed short probe pulse at $t = \Delta t$ (see Fig. D1 (a)). At $t = 0$, molecules in the excited sample are in a coherent superposition state between the upper and lower states of the Raman transition. This superposition state starts to decay after the excitation. At $t = \Delta t$, the probe pulse and the coherence that remains the sample generate the anti-Stokes pulse along the direction determined by phase-matching condition. The intensity of this output pulse is proportional to the square of the coherence that remains at the delay Δt . In the case of usual exponential-like decays,

$$I_{AS}(\Delta t) \propto \left| q_0 \cdot \exp \left(-\frac{\Delta t}{\tau} \right) \right|^2, \quad (\text{D1})$$

where q_0 is the amplitude of the vibrational coordinate at $t = 0$, and τ the coherence decay constant. The energy conservation law (Fig. D1 (a)) and the phase-matching condition (Fig. D1 (b)) are fulfilled in the TRCARS process as follows:

$$\omega_L - \omega_S = \omega_{AS} - \omega_P = \omega_0,$$

$$\mathbf{k}_L - \mathbf{k}_S = \mathbf{k}_{AS} - \mathbf{k}_P = \mathbf{k}_0.$$

Here ω_i and \mathbf{k}_i represent the frequency and the wavevector, related to each other by $|\mathbf{k}_i| = n(\omega_i)c\omega_i$, where $n(\omega_i)$ is the refractive index of solid para-hydrogen [73] at ω_i . c the speed of light in vacuum. The subscripts L, S, AS, and P represent pump, Stokes, anti-Stokes, and probe, respectively. For $v = 2$, ω_0 is $8070.4(1)$ cm^{-1} in solid hydrogen [74]. \mathbf{k}_0 is the wavevector generated at $t = 0$ and then probed at $t = \Delta t$.

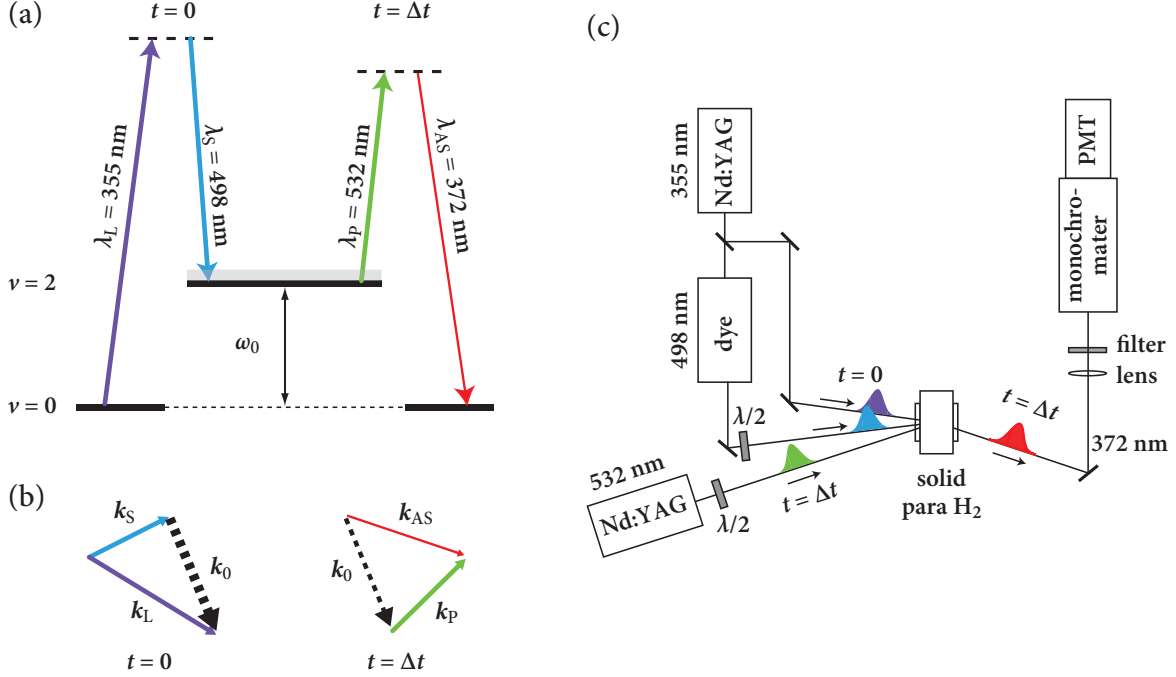


Fig. D1 (a) TRCARS scheme for $v = 2$ coherence decay measurement in solid para-hydrogen. The $v = 2$ coherence produced at $t = 0$ by a pump (denoted by the subscript L) and Stokes (S) pulse pair is monitored by a probe (P) pulse delayed by $t = \Delta t$ generating an anti-Stokes (AS) pulse. (b) The wavevector relations at $t = 0$ (left) and $t = \Delta t$ (right). (c) Experimental setup. Three nano-second pulsed lasers (Nd:YAG (wavelength: 355 nm) as pump, dye (498 nm) as Stokes, and another Nd:YAG (532 nm) as probe) were irradiated to a sample of solid para-hydrogen. The phase-matched anti-Stokes signal (372 nm) was detected by a photomultiplier tube after spectral separation via a UV filter and a monochromator.

The experimental setup used in this study is found elsewhere [75]. Briefly, the solid samples were obtained by the method described in Section 4.3.1. The sample temperature and the ortho hydrogen impurity concentration were controlled for optimization. For the TRCARS measurement as shown in Fig. D1 (b), three commercially available, nano-second pulsed lasers were used as the pump, Stokes, and probe sources. After spatial separation from the laser pulses, the anti-stokes signal pulse in the UV region was detected as a function of the delay.

D.2. $v = 2$ coherence time of solid para-hydrogen

Figure D2 shows the $v = 2$ coherence decay profiles under various conditions. Before optimization, the decay constants τ were found to be 10–15 ns (Fig. D2 (b)–(d)). Ortho hydrogen impurities disturb the translational symmetry of the sample crystal, then an induced inhomogeneous component contributes to the coherence decay [70] (Fig. D2 (b)). An additional contribution occurs from elastic scattering of the vibrationally excited molecules by thermal phonons [69, 76] (Fig. D2 (c)). This contribution is known to obey a T^7 law on the temperature dependence of the decay rates [77]. We observed this dependence for the $v = 2$

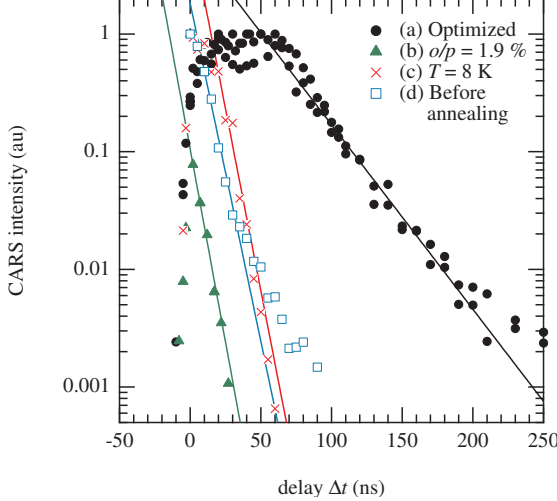


Fig. D2 Coherence decay profiles of the vibrational states $v = 2$ of solid para-hydrogen. (a) The decay measured under the optimized condition (after annealing, at the sample temperature $T = 4$ K, and at the ortho hydrogen concentration $o/p = 0.01\%$). The others were obtained under the same condition except for (b) $o/p = 1.9\%$, (c) $T = 8$ K, and (d) before annealing. Each profile is normalized by its peak value. Solid lines are exponential fits to the data, in which the data points corresponding to the normalized intensity below 0.1 were used. The decay constant τ of (a) is found to be ~ 50 ns.

excited state.[75] Finally, the intrinsic structural defects induced during sample preparation accelerates the coherence decay (Fig. D2 (d)).

By improving the sample conditions described above, we obtained quite a long decay profile (Fig. D2 (a)). Here, the ortho concentration was lowered to 0.01 %, and the sample temperature was cooled down to $T = 4$ K. To optimize the decay further, an annealing process for half an hour at $T = 9$ K was performed before the measurement. As seen in Fig. D2 (a), the coherence was kept almost constant up to ~ 50 ns just after the excitation. This can be accounted for by a transient stimulated Raman process induced on the excitation. [78] The profile after this plateau has an exponential-like decay. Fitting this part to Eq. D1 gives $\tau \sim 50$ ns. A deviation from an exponential function at longer delay (also seen in Fig. D2 (d)) is discussed elsewhere. [75] The obtained coherence time for $v = 2$ is comparable to that for $v = 1$. In the PSR process, a coherent superposition state of the upper and lower states develops in time. It is required that the disturbance of the coherence is weak during the process. The long coherence times of $v = 1$ and $v = 2$ show that a nano-second scale measurement can trace PSR signals for solid para-hydrogen when these states are employed.

Generally in solid samples at low temperatures, the dephasing mechanism in the gas phase as Doppler broadening and collisional relaxation is minimized. Instead, the interatomic/intermolecular distance is close as a few Å, and the inhomogeneity and the fluctuation of the solid crystal structure causes corresponding variations in the interatomic/intermolecular interaction. These variations result in fast relaxation usually in a time scale of 10–100 ps. However, the vibrational states in solid para-hydrogen have such a

long coherence time as a few 10 ns, because of a rather weak intermolecular interaction and the high homogeneity due to large zero-point vibration around lattice points.

The coherence time of 50 ns obtained here for the $v = 2$ state of solid para-hydrogen satisfies the assumption in a simulative work of PSR. [14] The coherence time can be further improved by a single crystal sample by the pressurized liquid method [79], that was exhibited for $v = 1$.[38]. To succeed in PSR observation, the excitation sample density is another important factor. Additionally, the initial coherence preparation by intense lasers are necessary to observe an explosive PSR. In the present solid para-hydrogen experiment, the low damage threshold of our sample crystals ($\sim 1 \text{ MW/cm}^2$) limits the maximum laser intensity. Crystals with high damage threshold can be obtained by the pressurized liquid method mentioned above. In order to achieve the initial coherence of 0.1 – 0.01 as achieved in the $v = 1$ excitation,[80] the excitation lasers are required to have a good coherence. These laser system, as discussed in Sec. 4.2.2, is being exploited for PSR in gas para-hydrogen experiment, which is a promising candidate for explosive PSR because the samples are basically damage-free.

E. Experimental studies on PSR/RENP targets in condensed phases

Atomic and molecular systems, examined in our group for PSR/RENP targets other than pH_2 , I_2 , and Xe , are briefly introduced. Condensed matter targets are advantageous in the following three aspects. 1) High density energy storage is possible in a typical number density of 10^{21} cm^{-3} for target atoms and molecules. 2) Coherence control is possible by tuning inter-atomic or inter-molecular interaction to suppress undesired processes for decoherence accompanied by dissipation of energy. 3) Doppler broadening in the spectral linewidth is minimized by keeping the solid sample at low temperatures. Despite a disadvantage for some materials of relatively low damage threshold to laser exposure, solid targets are promising for future experimental research for PSR/RENP. In this Appendix, spectroscopic characterization of condensed-phase atomic and molecular systems are described, i.e., HF molecules in solid pH_2 , atomic N in a carbon cage of C_{60} , and Bi atoms in solid Ne.

E.1. Bismuth in neon matrix

E.1.1. Energy levels of Bi. As a heavy element with large spin-orbit coupling, bismuth is one of the excitation targets for the observation of radiative emission of neutrino pair (RENP). Figure E1 shows the energy levels for Bi atom. Similarly to the other group-15 elements, the low-lying excited states, $^2\text{P}_{3/2,1/2}$ and $^2\text{P}_{5/2,3/2}$, are stemming from the same electron configuration, $6s^26p^3$, as that for the ground state, $^4\text{S}_{3/2}$. Due to the large spin-orbit coupling, however, unlike the lightest group-15 element of nitrogen, different J states for bismuth are largely separated, i.e., 10504 cm^{-1} for ^2P ($J=3/2$ and $1/2$) and 4019 cm^{-1} for ^2D ($J=5/2$ and $3/2$). As a result of the mixing of different spin states, orbital angular momentum, L , and spin angular momentum, S , are no longer good quantum numbers. As a result of the mixing of different spin states by the spin-orbit interaction, transitions become possible for a pair of states with the same electron configuration. The radiative lifetimes for these transitions, $\sim 10^{-2}$ – 10^{-1} seconds in the gas phase, are long enough to be detected by using an instantaneous excitation with a nanosecond laser pulse. These low-lying excited

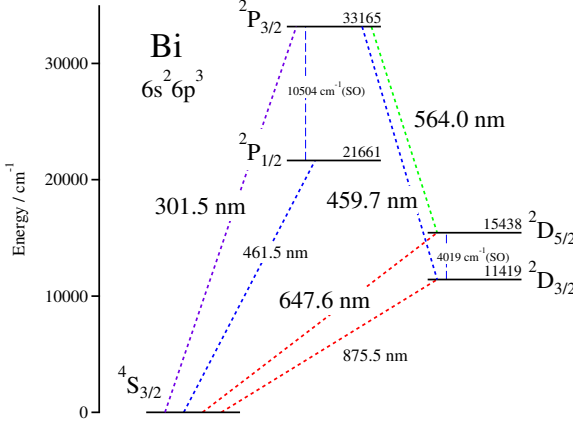


Fig. E1 Level diagram of bismuth atom (gas phase).

states were observed in solid Ne matrix [81]. Using higher excited levels accessible by non-resonant two-photon excitation, single-photon super-radiance was observed with Bi atoms in the gas phase [82].

E.1.2. PSR/RENP transition. In Fig. E1, two energy levels are noted. One is a metastable ²D_{5/2} state (6p³) and the other is the ground ⁴S_{3/2} state (6p³). These two states can be connected via intermediate states at higher energies, e.g., ⁴P_{5/2} (6p³7s¹), with a combination of E1 and M1 (practically E1) transitions. The set of these energy levels is an example for a λ -type ladder for paired super-radiance (PSR) using bismuth atoms. If the coherence is developed between the ground state and the metastable excited state, and if an appropriate trigger source is applied to the system, explosive two-photon emission of radiation by PSR or even RENP can be promoted. A PSR rate of \sim 17 kHz was calculated for the number density 10^{16} cm⁻³ of excited bismuth atoms.

E.1.3. Matrix isolation technique. In order to realize PSR or RENP, to produce a system containing a large number of excited atoms in a small volume is crucial. The use of a solid-state material is demanded for realization of a large atomic density, thus for prolonged observation in the detection of events. Matrix isolation technique has been a spectroscopic tool applicable to reactive species such as atoms, molecules, open-shell radicals, and clusters of metal atoms. The target species are entrapped in small vacancies in rare-gas solids of Ne, Ar, Kr, or Xe. The number density of target atoms can be increased up to 10^{20} cm⁻³ under well-isolated conditions. For matrix-isolated species, relaxation pathways to the long-lived metastable state can be enhanced, by which the excited-state population is increased to a substantial fraction or even inverted against the ground state, as recently demonstrated for Yb atoms in solid Ne [83].

E.1.4. Laser induced optical emission. We performed laser-induced optical emission spectroscopy to determine energy levels and lifetimes for Bi atoms in solid Ne matrix. Vapor of bismuth emanated from a bismuth-containing molybdenum crucible at \sim 1000 K was co-deposited on a cold surface of sapphire at 3 K together with an excess of neon gas. After

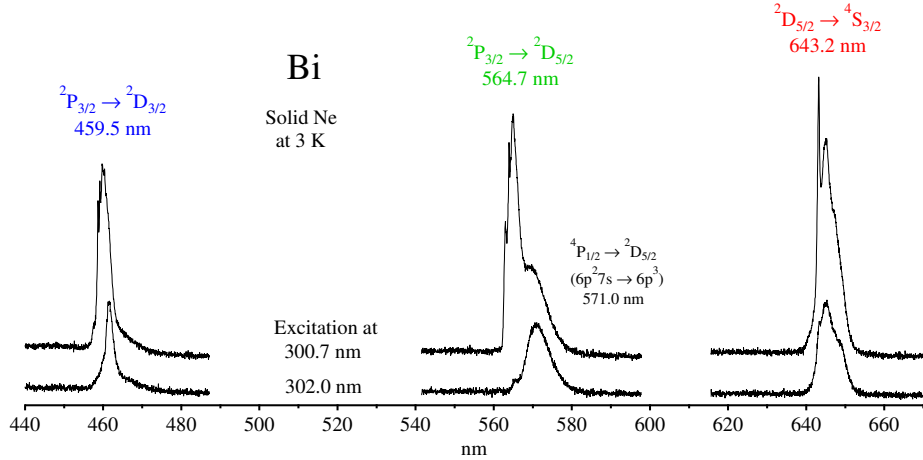


Fig. E2 Emission spectra of Bi atoms trapped in a solid Ne matrix at 3 K using the excitation with nanosecond laser pulses at 300.7 nm (upper trace) and 302.0 nm (lower trace) for the $^2\text{P}_{3/2} \leftarrow ^4\text{S}_{3/2}$ transition.

the deposition, nanosecond laser pulses tuned at transition wavelengths for Bi atom were irradiated on the solid sample in a grazing angle. The emitted light was dispersed by using a grating spectrometer (Acton SP300i) and detected by using a CCD camera (PI SPEC10) for the observation of emission spectra. A photomultiplier (Hamamatsu R928) was used for the measurement of lifetimes. In order to reduce stray light of the excitation laser, a long-pass optical filter (Schott Glass Filter) was used.

First we excited the $^2\text{P}_{3/2} \leftarrow ^4\text{S}_{3/2}$ transition. Figure E2 shows typical emission spectra for the excitation at 300.7 nm. Emission bands corresponding to three relaxation pathways were observed. Two of them were the transitions from the upper state of $^2\text{P}_{3/2}$ to the metastable states of $^2\text{D}_{5/2}$ (565 nm) and $^2\text{D}_{3/2}$ (460 nm). The other one was the transition from the metastable state of $^2\text{D}_{5/2}$ (645 nm) to the ground state of $^4\text{S}_{3/2}$. Each band was composed of a few lines, for which the relative intensity varied upon different excitation wavelengths. At the excitation wavelength of 300.7 nm providing maximum emission intensity, relatively sharp emission lines were intensified at the blue edge of the emission band. A broad emission band at 570 nm in the lower trace in Fig. E2 may be associated with another transition of $^4\text{P}_{1/2} \rightarrow ^2\text{D}_{5/2}$ ($6\text{p}^2 7\text{s}^1 \rightarrow 6\text{p}^3$), whose upper state of $^4\text{P}_{1/2}$ locates slightly below the $^2\text{P}_{3/2}$ (6p^3) level. The lifetime for this transition at 570 nm was several times shorter than that for the transition at 565 nm.

Figure E3 depicts decay profiles for the three transitions for Bi atom in solid Ne. The single exponential fits provide lifetimes of 1.05 ms for $^2\text{D}_{5/2} \rightarrow ^4\text{S}_{3/2}$, 0.31 ms for $^2\text{P}_{3/2} \rightarrow ^2\text{D}_{5/2}$, and 0.35 ms for $^2\text{P}_{3/2} \rightarrow ^2\text{D}_{3/2}$. These lifetimes in a Ne matrix are two orders of magnitude shorter than those in the gas phase. The latter two, corresponding to relaxation to the metastable $^2\text{D}_{5/2,3/2}$ states, showed a single exponential decay with a characteristic lifetime of ~ 0.3 ms, while the former one, from the metastable state to the ground state, showed a characteristic feature of rise in ~ 0.2 ms and a decay in a longer lifetime of ~ 1 ms. These profiles are consistent with a picture that the population in the metastable state, $^2\text{D}_{5/2}$, increases via

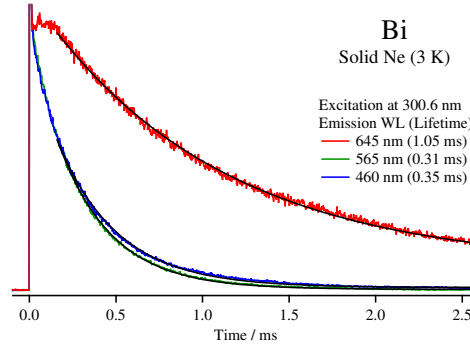


Fig. E3 Decay of emission bands for Bi in solid Ne with the excitation at 300.6 nm, $^2\text{D}_{5/2} \rightarrow ^4\text{S}_{3/2}$ (645 nm), $^2\text{P}_{3/2} \rightarrow ^2\text{D}_{5/2}$ (565 nm), and $^2\text{P}_{3/2} \rightarrow ^2\text{D}_{3/2}$ (460 nm).

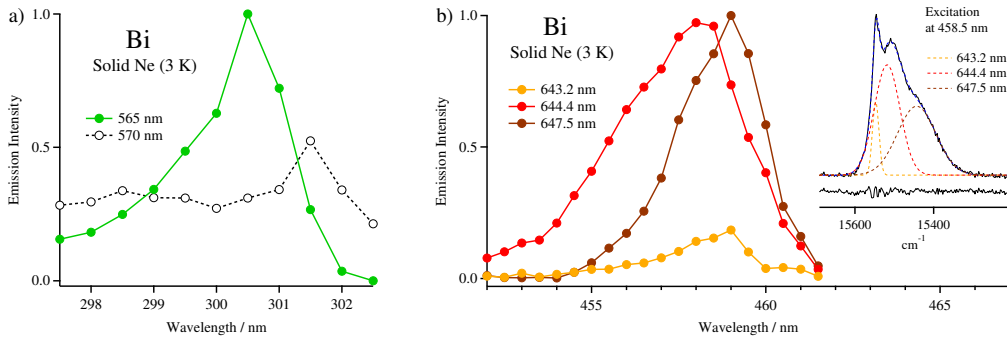


Fig. E4 Excitation profiles for Bi in solid Ne, a) $^2\text{P}_{3/2} \leftarrow ^4\text{S}_{3/2}$ (~ 300 nm) and b) $^2\text{P}_{1/2} \leftarrow ^4\text{S}_{3/2}$ (~ 460 nm). Inset shows a typical emission spectrum with fitting curves by three components.

the radiative decay of $^2\text{P}_{3/2} \rightarrow ^2\text{D}_{5/2}$ in a time scale of ~ 0.3 ms and decreases via that of $^2\text{D}_{5/2} \rightarrow ^4\text{S}_{3/2}$ in ~ 1 ms.

In order to locate the energy levels of $^2\text{P}_{3/2}$ and $^2\text{P}_{1/2}$ states, excitation profiles were examined. By using the photomultiplier detector equipped to the spectrometer, emission intensity at a fixed wavelength was measured and plotted as a function of laser-excitation wavelength. Figure E4 shows the excitation profiles for Bi atoms in solid Ne. Corresponding to the absorption for $^2\text{P}_{3/2} \leftarrow ^4\text{S}_{3/2}$, the maximum was found at 300.5 ± 0.25 nm by plotting the emission intensity at 565 nm as shown by closed circles in green in Fig. E4(a). The bandwidth for this transition was ~ 2 nm (~ 220 cm^{-1}). The excitation profile for the 570-nm emission band (see the lower trace in Fig. E2) was much broader as shown by open circles in Fig. E4(a). For $^2\text{P}_{1/2} \leftarrow ^4\text{S}_{3/2}$, the maximum was found at 458.5 ± 0.25 nm by plotting the emission intensity at 645 nm as shown by the three profiles in Fig. E4b, for which spectral decomposition was performed for each of the observed emission spectra at different excitation wavelengths and the excitation profile was plotted for each of the three components in the emission spectrum. The bandwidth for the $^2\text{P}_{1/2} \leftarrow ^4\text{S}_{3/2}$ transition was ~ 4 nm (~ 190 cm^{-1}).

Table E1 Observed transitions for Bi atoms in solid Ne matrix and comparison with the transition energy in the gas phase. ^aRadiative lifetimes in solid Ne with an excitation at 300.6 nm. ^bDifference of term energies.

Transition	Wavelength/nm	Lifetime/ms ^a	Energy/cm ⁻¹	Energy(gas)/cm ⁻¹
$^2P_{3/2} \leftarrow ^4S_{3/2}$	300.5	-	33280	33165
$^2P_{1/2} \leftarrow ^4S_{3/2}$	458.5	-	21810	21661
$^2P_{3/2} \rightarrow ^2D_{3/2}$	459.5	1.05	21760	21746 ^b
$^2P_{3/2} \rightarrow ^2D_{5/2}$	564.7	0.31	17710	17727 ^b
$^2D_{5/2} \rightarrow ^4S_{3/2}$	643.2	0.35	15550	15438

E.1.5. Linewidth and coherence. At the blue edge for each of the emission bands in Fig. E2, a relatively sharp peak is discernible. This peak corresponds to the zero-phonon line for each transition. The linewidth for these relatively sharp lines was $\sim 10 \text{ cm}^{-1}$, while the total width for the bands was $\sim 200 \text{ cm}^{-1}$. Even for the narrow lines, the linewidth corresponds to a natural lifetime on the order of $\sim 10^{-12}$ seconds. Since the observed lifetimes in Fig. E3 is much longer, $\sim 1 \text{ ms}$, the observed spectral linewidth is ascribed to inhomogeneous broadening due to interaction of the target atoms with the matrix media. With substantial deviations in the transition wavelength, it is considered to be difficult to develop coherence longer than a picosecond in this system.

The laser-induced emission spectroscopy revealed energy levels for all the 6p³ states of Bi atom in solid Ne. The observed transitions in this work are summarized in Table E1. Term energies for the four low-lying excited states of Bi atom in solid Ne remain intact as those in the gas phase within a bandwidth in the matrix spectra. Lifetimes were revealed to be two orders of magnitude shorter than those in the gas phase. Despite the advantage of the long lifetimes of $\sim 1 \text{ ms}$, the apparent inhomogeneous broadening would suppress coherence time shorter than expected. To remove undesired interaction between embedded guest atoms and hosting matrix atoms is crucial for realizing a system for PSR or RENP.

E.2. HF molecule trapped in solid pH₂

E.2.1. Matrix isolation spectroscopy using solid pH₂. Spectroscopy of molecules embedded in condensed phases is called matrix isolation spectroscopy, which has long been used to pilot gas phase spectroscopy. Not only unstable but also stable molecules have been subjected to studies by this method. Rare gas matrices such as solid Ne and solid Ar have been widely used because of their chemical inertness and of relatively weak perturbative interactions. The perturbation in solid rare-gas matrices sometimes makes spectral linewidths broader compared to those in the gas phase spectroscopy, to conceal detailed spectroscopic information. Small molecules in solid pH₂, on the other hand, exhibit extremely sharp lines to reflect quantized rovibrational states of the entrapped molecules in the condensed phase. The full width at half maximum (FWHM) for the vibrational ν_4 band of methane, CH₄, in solid pH₂ is as narrow as 0.015 cm⁻¹, whose signal is more than one order of magnitude sharper than that observed in conventional solid rare-gas matrices [84]. Such a narrow linewidth of $\sim 0.01 \text{ cm}^{-1}$ is a promise of a long relaxation time advantageous for the observation of coherent phenomena.

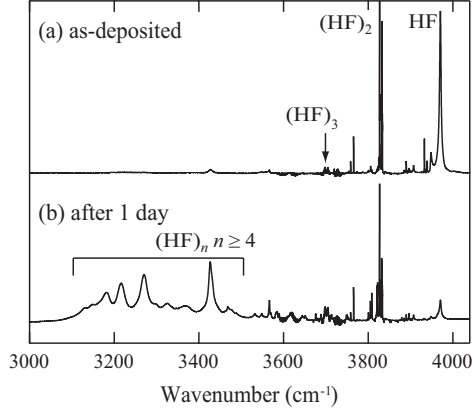


Fig. E5 IR absorption spectra of HF molecules in solid pH₂ for the sample a) as prepared and b) 1-day after preparation.

E.2.2. Preparation of chemically doped solid pH₂. To prepare the doped solid pH₂, the closed cell method (Sec. 4.2.1) can be used. Premixed pH₂ gas containing small amount of the target molecules is introduced into the cooled closed cell and a transparent doped crystal grows in the same manner as pure pH₂. However, only dopants of small intermolecular interaction like methane are isolated by this method while molecules with strong interaction like HF are difficult to be doped dispersedly. In contrast, the rapid deposition method developed by Fajardo et al [85] can isolate a number of molecular species in solid pH₂. They include CH₄, CH₃F, CH₃I, CH₂ClI, CO, CO₂, NO, N₂O, H₂O, HF, and HCN. Several millimeters thick, optically transparent solid pH₂ can be prepared by this method. The pH₂ and dopant molecules are co-deposited onto a cold substrate (typically BaF₂ at 2~4 K) placed in a cryostat. The substrate is contacted on the copper block with an indium gasket. The crystal grows perpendicularly from the substrate and a polycrystalline aggregate of h.c.p. and f.c.c. having their c axes roughly normal to the substrate is produced. To remove the metastable f.c.c. crystal, the mixed crystals are heated up to ~ 5 K for 10 to 30 min. This annealing aligns c axes normal to the substrate.

E.2.3. Infrared spectroscopy of HF in solid pH₂. Hydrogen fluoride, HF, in solid pH₂ has been studied in our laboratory as a target for super-radiance in the condensed phase [86]. Super-radiance was observed indeed in the gas phase for the rotational transition of HF, where gaseous HF was optically pumped into the rovibrationally excited state ($v=1, J$) for realizing total population inversion against the lower state ($v=1, J-1$), resulting in the super-radiance with far infrared (FIR) emission of photons [21].

We measured IR absorption spectra for HF molecules in solid pH₂ at 3.6 K by using an FTIR spectrometer. The observed spectra for HF/pH₂ are shown in Fig. E5. Based on the systematic spectral change caused by the difference in HF/pH₂ concentration (not shown), we assigned the observed IR absorption lines in the region of 4000-3000 cm⁻¹ to isolated molecular HF, dimers (HF)₂, trimers (HF)₃, and clusters (HF)_n ($n \geq 4$) as indicated in Fig. E5.

Time evolution in the IR absorption spectra in Fig. E5(a) and E5(b) indicated that the HF molecules could migrate in the solid pH₂ at 3.6 K, as was noted by the decrease in the line

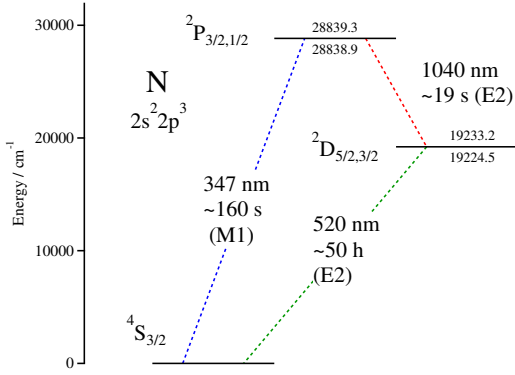


Fig. E6 Level diagram of nitrogen atom (gas phase).

at 3970 cm^{-1} for isolated HF and the concomitant increase in the bands at lower frequencies for clusters $(\text{HF})_n$. The aggregation of HF molecules in solid pH₂ indicates that the isolated HF molecules cannot be the targets for long-term observation. Moreover, the linewidth for the isolated HF in solid pH₂ is rather broad, $\sim 4\text{ cm}^{-1}$, probably due to matching between rotational energy for HF and phonon energy for solid pH₂. Note that the linewidth for the signal at 3820 cm^{-1} for the dimer, $(\text{HF})_2$, is much narrower than that for the isolated HF, probably because the rotational motion is quenched. Solid pH₂ is, in general, a good matrix medium for trapping molecules with minimal interaction, whereas, for the small but polar molecule such as HF, another difficulty may arise in migration or rotation-phonon coupling.

E.3. Nitrogen atom in fullerene C₆₀

E.3.1. N@C₆₀: discovery and characteristics. Fullerene C₆₀ is a hollow, closed-cage molecule of carbon with a dimension of $\sim 1\text{ nm}$, in which atoms of the other elements can be accommodated. Atoms of lanthanides and some transition metals are encapsulated in larger fullerenes such as C₈₂ by carbon arc using a metal-carbon composite rod as an electrode. Encapsulation of atoms in a C₆₀ cage of icosahedral symmetry has turned out to require another method, i.e., ion implantation. Li@C₆₀ [87] is a prototype of ion-implanted fullerene molecules (M@C₆₀ depicts M inside a C₆₀ fullerene cage) [88], while N@C₆₀ is an unique member among the endohedral fullerenes [89].

Unlike metallofullerenes having a metal atom locating close to inner walls of the carbon cage, the nitrogen atom in C₆₀ is believed to be located at the center of symmetry of the C₆₀ molecule. Moreover, the electron spin, $S = 3/2$, of atomic nitrogen is retained even in the carbon cage. Furthermore, the phase coherence time in the electronic ground state can be longer than 0.2 ms as revealed by electron paramagnetic resonance (EPR) [90]. With all these characteristics in mind, one can believe that the interaction between the trapped atom and the hosting cage should be minimized, thus enjoyed by further experimental studies. Once a crystalline form of pure N@C₆₀ is obtained, the density of atomic nitrogen amounts to $2.0 \times 10^{21}\text{ cm}^{-3}$, each atom being well isolated as a spin carrier for coherent phenomena.

E.3.2. Electronic states of atomic nitrogen. Figure E6 illustrates atomic energy levels for some low-lying electronic states of free nitrogen atom. The excited states, $^2\text{P}_{3/2,1/2}$ and $^2\text{D}_{5/2,3/2}$, as well as the ground state, $^4\text{S}_{3/2}$, are stemming from the same electron configuration of $2\text{s}^22\text{p}^3$. Therefore, transition between any pair of states is forbidden by E1 mechanism. To excite N atom in its ^2P or ^2D states, some higher excited states to which the E1 transition is allowed from the ground state should be involved. Note that transitions between the low-lying electronic states are possible by M1 and/or E2 mechanism, though the rate of these transitions is relatively slow.

The excitation channel by E1 mechanism is realized by vacuum-UV transitions of $3\text{s} \leftarrow 2\text{p}$ (120 nm and 113 nm). Pumping to the higher level of $^4\text{P}_{5/2,3/2,1/2}$ is followed by relaxation to the low-lying excited state of $^2\text{P}_{3/2,1/2}$ or $^2\text{D}_{5/2,3/2}$ via transitions induced by spin-orbit interaction. When the incoherent energy loss is minimized, population at the low-lying excited state increases by repetitive pumping at a high rate.

E.3.3. Preparation of N@C_{60} . Formation of N@C_{60} is conducted under vacuum where C_{60} molecules are bombarded with positively charged ions of nitrogen, which are accelerated to have a kinetic energy of several tens of electron volts. Eventually, some are trapped inside the C_{60} cage and extracted by solvents as a neutral molecule of N@C_{60} . The raw material after ion implantation contains at most one thousandth of N@C_{60} in C_{60} . Therefore, separation of N@C_{60} from C_{60} is crucial.

We succeeded in isolation of N@C_{60} using a recycling-HPLC system. Figure E7 shows a chromatogram for the final step of separation of N@C_{60} and C_{60} . Due to the faint difference in interaction between the molecule and the surface of the porous material in the 5PBB column, it takes a few percent longer times for N@C_{60} to pass through the column than those for C_{60} . After the repetitive passage of four cycles, the fraction of N@C_{60} was collected for the measurement of optical properties.

The inset in Fig. E7 shows UV-vis absorption spectrum of N@C_{60} after purification. The three major bands in the UV are essentially the same as those for empty C_{60} , indicating that the interaction between the N atom and the C_{60} molecule is not discernible at all. Since the excited states for N@C_{60} , ^2P and ^2D , are not accessible directly by the transition of E1 mechanism, corresponding absorption lines are not observed. It is natural to consider that the low-lying excited states of atomic nitrogen in a C_{60} cage remain intact as those in the gas phase.

E.3.4. EPR detection. Here, the EPR properties in the ground state are described briefly to demonstrate the significance of N@C_{60} . In the inset in Fig. E8, three narrow lines by cw-EPR measurement correspond to the transitions between different hyperfine states in $^4\text{S}_{3/2}$ of $^{14}\text{N@C}_{60}$ at room temperature in a solution of carbon disulfide. Among the total 9 lines for the EPR transitions, three lines of constant $M_I = +1, 0$, or -1 are overlapping in each of the three lines in the spectrum. This indicates that there is no noticeable anisotropy for the electron spin in N@C_{60} .

The main panel in Fig. E8 displays free induction decay (FID) for the pulse-EPR signal for a powder sample of $\text{N@C}_{60}/\text{C}_{60}$ mixture, tuned close to the transition of the $M_I = +1$ line at lower field. The moderate wiggle of a period of $\sim 3 \mu\text{s}$ is due to detuning from the line of $M_I = +1$, while the rapid modulation is due to interference by the signals of $M_I = 0$ and

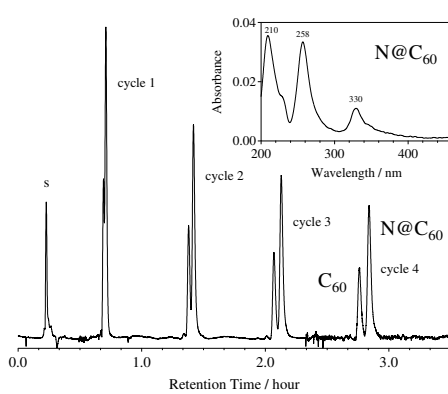


Fig. E7 HPLC chromatogram for separation of N@C_{60} and C_{60} , i.e., the 6th recycling step using 5PBB ($\phi 10 \times 250 \text{ mm} \times 3$ columns), toluene (3.0 mL min^{-1}), and a UV detector (333 nm). Inset shows UV-vis absorption spectrum of the fraction at 2h52m in the main panel. Using absorption coefficient for C_{60} ($4.8 \times 10^5 \text{ L mol}^{-1} \text{ cm}^{-1}$ at 330 nm) and the volume of the solution (2.5 mL), the amount of isolated N@C_{60} is estimated to be 3×10^{14} molecules.

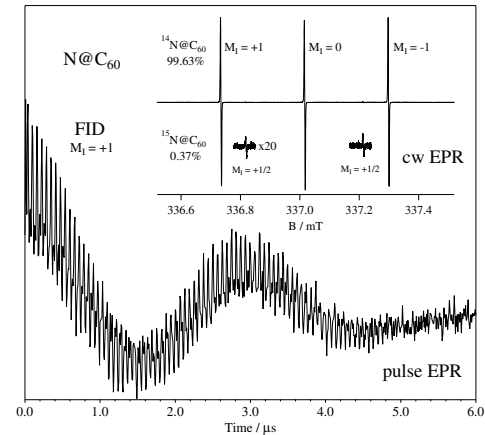


Fig. E8 FID signal for the $M_I = +1$ transition of $^{14}\text{N@C}_{60}$ ($I = 1$) obtained from X-band pulse-EPR measurement at room temperature for the powder sample of $\text{N@C}_{60}/\text{C}_{60}$ mixture (main panel). Inset shows X-band cw-EPR spectrum of purified N@C_{60} in carbon disulfide. The triplet with a hyperfine splitting of 15.8 MHz belongs to $^{14}\text{N@C}_{60}$ ($I = 1$), while the weak doublet with a splitting of 22.1 MHz belongs to $^{15}\text{N@C}_{60}$ ($I = 1/2$).

$M_I = -1$ which are separated by 15.8 and 31.6 MHz from the $M_I = +1$ line, respectively. Owing to the narrow linewidth even in a solid state, coherence can be maintained at least for several microseconds.

In conclusion, we have developed a system for preparation of purified N@C_{60} in a microgram order, $\sim 10^{14}$ molecules. UV-vis absorption spectra indicate that the nitrogen atom in a C_{60} cage stays intact as that in the gas phase. The excited-state properties are intriguing in view of the coherent phenomena induced by radiation field.

References

- [1] J. Beringer et al. (Particle Data Group), *Phys. Rev.* **D86**, 010001(2012). Our definition of Majorana phases are related to their α_i by $\alpha = (\alpha_2 - \alpha_1)/2, \beta = -\alpha_1/2$.
- [2] G.L. Fogli et al., arXiv: 1205.5254v3(2012). Reports from Daya Bay, RENO, Double Chooz, and T2K at International Conference on Neutrino Physics and Astrophysics, "Neutrino 2012" at Kyoto, available at web-site neu2012.kek.jp.
- [3] M. Doi, T. Kotani, H. Nishiura, K. Okuda and E. Takasugi, *Phys. Lett.* **102B**, 323(1981).
- [4] E. Komatsu et al., *ApJS* **192**, 18(2011).
- [5] M. Fukugita and T. Yanagida, *Phys. Lett.* **B 174** 45 (1986).
- [6] S. Davidson and A. Ibarra, *Nucl. Phys.* **B648**, 345 (2003), and references therein.
- [7] S.M. Bilenky, J. Hosek, and S.T. Petcov, *Phys. Lett.* **B94**, 495(1980). J. Schechter and J.W.F. Valle, *Phys. Rev.* **D22**, 2227(1980).
- [8] M. Yoshimura, *Phys. Lett.* **B699**, 123(2011).
- [9] M. Yoshimura, *Phys. Rev.* **D75**, 113007(2007).
- [10] M. Yoshimura, A. Fukumi, N. Sasao, T. Yamaguchi, *Progr. Theo. Phys.* **123**, 523(2010).
- [11] I.J.R. Aitchison and A.J.G. Hey, *Gauge Theories in Particle Physics*, Vol.1 and 2, 3rd edition (informa, 2003).
- [12] D.N. Dinh, S. Petcov, N. Sasao, M. Tanaka, and M. Yoshimura, *Observables in neutrino mass spectroscopy using atoms*.
- [13] For a review of both the theory and experiments of superradiance, M. Benedict, A.M. Ermolaev, V.A. Malyshev, I.V. Sokolov, and E.D. Trifonov, *Super-radiance Multiatomic coherent emission*, Informa (1996). For a formal aspect of the theory, M. Gross and S. Haroche, *Phys. Rep.* **93**, 301(1982). The original suggestion of superradiance is due to R.H. Dicke, *Phys. Rev.* **93**, 99(1954).
- [14] M. Yoshimura, N. Sasao, and M. Tanaka, *Phys. Rev.* **A86**, 013812(2012), and *Dynamics of paired superradiance*, arXiv:1203.5394[quan-ph] (2012).
- [15] M. Yoshimura, C. Ohae, A. Fukumi, K. Nakajima, I. Nakano, H. Nanjo, and N. Sasao, *Macro-coherent two photon and radiative neutrino pair emission*, arXiv 805.1970[hep-ph](2008).
M. Yoshimura, *Neutrino Spectroscopy using Atoms (SPAN)*, in Proceedings of 4th NO-VE International Workshop, edited by M. Baldo Ceolin(2008).
- [16] L.M. Narducci, W.W. Eidson, P. Furciniti, and D.C. Eteson, *Phys. Rev.* **A 16**, 1665 (1977); M. Yoshimura, *Progr. Theor. Phys.* **125**, 149 (2011).
- [17] For instance, B.H. Bransden and C.J. Joachain, *Physics of Atoms and Molecules*, 2nd edition, Prentice Hall (2003).
- [18] T. Takahashi and M. Yoshimura, *Effect of Relic Neutrino on Neutrino Pair Emission from Metastable Atoms*, hep-ph/0703019.
- [19] G. Lindblad, *Comm. Math. Phys.* **48**, 119 (1976).
- [20] F. Haake, H. King, G.S. Schoeder, J. Haus, and R. Glauber, *Phys. Rev.* **A 20**, 2047(1979). D. Polder, M.F.H. Schuurmans, and Q.H.F. Vrehe, *Phys. Rev.* **A 19**, 1192(1979).
- [21] N. Skribanowitz, I.P. Herman, J.C. McGillivray, and M.S. Feld, *Phys. Rev. Lett.* **30**, 309(1973). For a review, see Chapter 2 of *Super-radiance Multiatomic coherent emission* [13].
- [22] Q.H.F. Vrehe and M.F.H. Schuurmans, *Phys. Rev. Lett.* **42**, 224(1979). N.W. Carlson, D.J. Jackson, A.L. Schaslow, M. Gross, and S. Haroche, *Opt. Commun.* **32**, 350(1980).
- [23] C. Ohae et al., work in progress
- [24] M. Tashiro, M. Ehara, S. Kuma, Y. Miyamoto, N. Sasao, S. Uetake, and M. Yoshimura, work in progress.
- [25] W.A. de Jong, L. Visscher, and W.C. Nieuwpoort, *J. Chem. Phys.* **107**, 21(1997) and references therein.
- [26] P. Clark Souers: *Hydrogen properties for Fusion Energy* (University of California Press, 1986).
- [27] U. Fink, T. A. Wiggins and D. H. Rank: *J. Mol. Spectrosc.* **18** (1965) 384
- [28] S. E. Harris, and A. V. Sokolov: *Phys Rev. A* **55** (1997) R4019
- [29] D. D. Yavuz, D. R. Walker, M.Y. Shverdin, G.Y. Yin, and S. E. Harris: *Phys Rev. Lett.* **91** (2003) 233602
- [30] J. Q. Liang, M. Katsuragawa, Fam Le Kien, and K. Hakuta: *Phys Rev. Lett.* **85** (2000) 2474
- [31] M. Katsuragawa, K. Yokoyama, and T. Onose: *Opt. Express* **13** (2005) 5628
- [32] J. -M. Hartmann, C. Boulet, D. Robert: *Collisional effects on molecular spectra* (Elsevier, 2008).
- [33] W. B. Bischel and M. J. Dyer: *Phys Rev. A* **33** (1986) 3113
- [34] Y. V. Vanne and A. Saenz: *Phys Rev. A* **80** (2009) 053422
- [35] T. Momose and T. Oka: *J. Low. Temp. Phys.* **139** (2005) 515
- [36] J. Z. Li, M. Suzuki, M. Katsuragawa, and K. Hakuta: *J. Chem. Phys.* **115** (2001) 930
- [37] T. Oka: *Annu. Rev. Phys. Chem.* **44** (1993) 299
- [38] M. Suzuki, M. Katsuragawa, R. S. D. Sihombing, J. Z. Li, K. Hakuta: *J. Low. Temp. Phys.* **111** (1998)

[39] Robert W. Boyd, *Nonlinear Optics*, Chapter 2 (Academic Press, second edition, 2003).

[40] W. Demtröder, *Laser Spectroscopy, volume 1*, Chapter 5.8 (Springer, Berlin, fourth edition, 2008).

[41] Takayuki Suzuki, Masataka Hirai, and Masayuki Katsuragawa, Phys. Rev. Lett., **101**, 243602 (Dec 2008).

[42] J. E. Bjorkholm and H. G. Danielmeyer, Appl. Phys. Lett., **15**(6), 171–173 (1969).

[43] J. M. Boon-Engering, W. E. van der Veer, J. W. Gerritsen, and W. Hogervorst, Opt. Lett., **20**(4), 380–382 (Feb 1995).

[44] A Borsutzky, Quantum Semiclass. Opt., **9**(2), 191 (1997).

[45] P. Bourdon, M. Péalat, and V. I. Fabelinsky, Opt. Lett., **20**(5), 474–476 (Mar 1995).

[46] W. D. Kulatilaka, T. N. Anderson, T. L. Bouger, and R. P. Lucht, Applied Physics B: Lasers and Optics, **80**, 669–680 (2005).

[47] M. J. T. Milton, T. D. Gardiner, G. Chourdakis, and P. T. Woods, Opt. Lett., **19**(4), 281–283 (Feb 1994).

[48] A. V. Smith, W. J. Alford, T. D. Raymond, and Mark S. Bowers, J. Opt. Soc. Am. B, **12**(11), 2253–2267 (Nov 1995).

[49] Narayanan Srinivasan, Takashi Kimura, Hiromitsu Kiriyama, Masanobu Yamanaka, Yasukazu Izawa, Sadao Nakai, and Chiyo Yamanaka, Jpn. J. Appl. Phys., **35**(Part 1, No. 6A), 3457–3458 (1996).

[50] Ondrej Votava, Joanna R. Fair, David F. Plusquellec, Eberhard Riedle, and David J. Nesbitt, J. Chem. Phys., **107**(21), 8854–8865 (1997).

[51] Sheng Wu, Vadym A Kapinus, and Geoffrey A Blake, Optics Communications, **159**, 74 – 79 (1999).

[52] Eugene Hecht, *Optics*, Chapter 8.4 (Addison Wesley, San Francisco, fourth edition, 2002).

[53] Nan Ei Yu, Sunao Kurimura, Yoshiyuki Nomura, and Kenji Kitamura, Jpn. J. Appl. Phys., **43**(10A), L1265–L1267 (2004).

[54] M. Walhout, A. Witte, and S.L. Rolston, Phys. Rev. Lett. **72** (1994) 2843.

[55] A. Barbet, N. Sadeghi and J.C. Pebay-Peyroula, J. Phys. B **8** (1975) 1776.

[56] M. Aymar and M. Coulombe, At. DATA and Nucl. DATA Tab. **21** (1978) 537.

[57] C.H. Chen, G.S Hurst and M.G. Payne, Chem. Phys. Lett. **75** (1980) 473.

[58] R. Kau, I.D. Petrov, V.L. Sukhorukov, H. Hotop, Z. Phys. D **39** (1997) 267.

[59] H. Horiguchi, R.S.F. Chang, and D.W. Setser, J. Chem. Phys. **75** (1981) 1207.

[60] D.C. Morton, Astrophys. J. Suppl. Ser. **130** (2000) 403.

[61] K.-J. Boiler, A. Imamoglu, and S. E. Harris, Phys. Rev. Lett. **66** (1991) 2593.

[62] G. Z. Zhang, M. Katsuragawa, K. Hakuta, R.I. Thompson and B.P. StoicheffPhys. Rev. A **52** (1995) 1584.

[63] J.J. Sakurai, *Advanced Quantum Mechanics*, Addison-Wesley (1967).

[64] D.C. Burnham and R.Y. Chiao, Phys. Rev. **188**, 660(1969).

[65] D. R. Stull: Ind. Eng. Chem. **39** (1947) 540

[66] J. B. Koffend, A. M. Sibai, and R. Bacis: J. Physique **43** (1982) 1639

[67] R. Böhling, J. Langen, and U. Schurath: Chem. Phys. **130** (1989) 419

[68] T. Momose, D. P. Weliky, and T. Oka, J. Mol. Spectrosc. **153**, 760 (1992).

[69] K. Kuroda, A. Koreeda, S. Takayanagi, M. Suzuki, and K. Hakuta, Phys. Rev. B **67**, 184303 (2003).

[70] I. I. Abram, R. M. Hochstrasser, J. E. Kohl, and M. G. Semack, Chem. Phys. Lett. **71**, 405 (1980).

[71] J. Z. Li, M. Katsuragawa, M. Suzuki, and K. Hakuta, Phys. Rev. A **58**, R58 (1998).

[72] A. Laubereau and W. Kaiser, Rev. Mod. Phys. **50**, 607 (1978) and references therein.

[73] M. Perera, B. A. Tom, Y. Miyamoto, M. W. Porambo, L. E. Moore, W. R. Evans, T. Momose, and B. J. McCall, Opt. Lett. **36**, 840 (2011).

[74] W. R. C. Prior and E. J. Allin, Can. J. Phys. **50**, 1471 (1972).

[75] S. Kuma, Y. Miyamoto, K. Nakajima, A. Fukumi, K. Kawaguchi, I. Nakano, N. Sasao, M. Tanaka, J. Tang, T. Taniguchi, S. Uetake, T. Wakabayashi, A. Yoshimi, and Y. Yoshimura, submitted to J. Chem. Phys.

[76] F. L. Kien, A. Koreeda, K. Kuroda, M. Suzuki, and K. Hakuta, Jpn. J. Appl. Phys. **42**, 3483 (2003).

[77] D. E. McCumber and M. D. Sturge, J. Appl. Phys. **34**, 1682 (1963).

[78] R. L. Carman, F. Shimizu, C. S. Wang, and N. Bloembergen, Phys. Rev. A **2**, 60 (1970).

[79] B. A. Wallace and H. Meyer, J. Low Temp. Phys. **15**, 297 (1974).

[80] M. Katsuragawa, J. Q. Liang, Fam Le Kien, and K. Hakuta, Phys. Rev. A **65**, 025801 (2002).

[81] V. E. Bondybey, G. P. Schwartz, J. E. Griffiths, and J. H. English, Chem. Phys. Lett., **76**, 30 (1980).

[82] C. Cremer and G. Gerber, Appl. Phys. B, **35**, 7 (1984).

[83] C.-Y. Xu, S.-M. Hu, J. Singh, K. Bailey, Z.-T. Lu, P. Mueller, T. P. O'Conner, and U. Welp, Phys. Rev. Lett., **107**, 093001 (2011).

[84] S. Tam, M. E. Fajardo, H. Katsuki, H. Hoshina, T. Wakabayashi, and T. Momose, J. Chem. Phys. **111**, 4191 (1999).

- [85] M. E. Fajardo and S. Tam: J. Chem. Phys. **108** (1998) 4237
- [86] Y. Miyamoto, H. Ooe, S. Kuma, K. Kawaguchi, K. Nakajima, I. Nakano, N. Sasao, J. Tang, T. Taniguchi, and M. Yoshimura, J. Phys. Chem. A, **115**, 14254 (2011).
- [87] E. E. B. Campbell, S. Couris, M. Fanti, E. Koudoumas, N. Krawez, and F. Zerbetto, Adv. Mater., **11**, 405 (1999).
- [88] Y. Chai, T. Guo, C. M. Jin, R. E. Haufler, L. P. F. Chibante, J. Fure, L. Wang, J. M. Alford, and R. E. Smalley, J. Phys. Chem., **95**, 7564 (1991).
- [89] T. Almeida-Murphy, Th. Pawlik, A. Weidinger, M. Höne, R. Alcalá, and J.-M. Spaeth, Phys. Rev. Lett., **77**, 1075 (1996).
- [90] J. J. L. Morton, A. M. Tyryshkin, A. Ardavan, K. Porfyrikis, S. A. Lyon, and G. A. Briggs, J. Chem. Phys., **124**, 014508 (2006).
- [91] J.C. McGillivray and M.S. Feld, *Phys. Rev.A* **14**, 1169(1976).
- [92] M. Yoshimura, N. Sasao, and M. Tanaka, paper in preparation.